Cointercalation and In-Situ Plating for Advanced Sodium Batteries

By

Adam Paul Cohn

Dissertation

Submitted to the Faculty of the

Graduate School of Vanderbilt University

in partial fulfillment of the requirements

for the degree of

DOCTOR OF PHILOSOPHY

in

Mechanical Engineering

May 31st, 2018

Nashville, Tennessee

Approved:

Cary L. Pint, Ph.D.

Richard F. Haglund, Ph.D.

David E. Cliffel, Ph.D.

D. Greg Walker, Ph.D.

Jason G. Valentine, Ph.D.

Table of Contents

List of Figures iii
List of Publications ix
Chapter 1: Introduction 1
1.1 Motivation 1
1.2 History and overview of Li-ion batteries 1
1.3 Overview of Na-ion batteries 8
1.4 Na, diglyme and $NaPF_6$ 12
1.5 Dissertation organization 15
Chapter 2: Cointercalation of Solvated Na Ions into Few-Layer Graphene 17
2.1 Introduction 17
2.2 Background 17
2.3 Methods 18
2.3.1 Material fabrication and characterization 18
2.3.2 Electrochemical testing 18
2.3.3 In-situ Raman measurements 19
2.4 Results and discussion 20
2.3.2 Electrochemical testing 21
2.3.3 Post-cycling characterization 23
2.3.4 Cointercalation of K ions 24
2.3.5 In-situ Raman characterization 26
2.5 Conclusion 38
Chapter 3: Utilizing a Nucleation Layer to Enable an “Anode-Free” Na Battery 39
3.1 Introduction 39
3.2 Background 39
3.3 Methods 41
3.3.1 Electrochemical measurements 41
3.3.2 Na metal imaging 42
3.4 Results and discussion 43
3.5 Conclusion 52
Chapter 4: Rethinking Na-Ion Anodes as Nucleation Layers for Stable Na Metal Plating 53

4.1 Introduction 53
4.2 Methods 53
4.2.1 Material fabrication and characterization 53
4.2.2 Electrochemical testing 54
4.2.3 Data analysis 56
4.3 Results and discussion 56
4.3.1 Evaluating anode materials as nucleation layers 56
4.3.2 Additional testing on carbon black nucleation layer 63
4.3.3 Mitigating first-cycle loss 65
4.4 Conclusion 67
Chapter 5: An Anode-Free Battery with a $Na_3V_2(PO_4)_3$ Cathode 68
5.1 Introduction 68
5.2 Methods 68
5.2.1 Material fabrication and characterization 68
5.2.2 Electrochemical measurements 69
5.3 Results and discussion 70
5.3.1 Evaluating the $Na_3V_2(PO_4)_3$ cathode 70
5.3.1 Comparing the anode-free Na battery to the Na-ion battery 72
5.3.3 Anode-free cell testing 73
5.4 Conclusion 79
Chapter 6: Extending the Cycle Life of Anode-Free Batteries using a Cathode with an Ion Reservoir 80
6.1 Introduction 80
6.2 Methods 80
6.3 Results and discussion 80
6.4 Conclusion 88
Chapter 7: Conclusion 89
7.1 Summary and outlook 89
References 94

List of Figures

Figure 1: Battery configurations: (a) Li metal battery using Li metal anode, (b) Li-ion battery with anode host. 3

Figure 2: Illustration of the stage formation that occurs during the electrochemical intercalation of Li ions into graphite. Reproduced from Ref. 4 with permission. Copyright 1998, Wiley. 4

Figure 3: (a) Problematic cointercalatian of ion and solvent molecule, (b) intercalation of naked ion enabled by a stable SEI layer....6

Figure 4: Operating voltage vs. specific capacity for Na-ion (a) cathodes and (b) anodes. The difference between the operating voltage of the anode and cathode determines the full-cell operating voltage. Reproduced from Ref. 9 with permission. Copyright 2016, Nature Publishing Group....10

Figure 5: (a) Illustration of the electrochemical window of different solvent families using tetraalkyl ammonium salts. Adapted from Ref. 6 with permission of The Royal Society of Chemistry. (b) Illustration of the relative energies of the anode and cathode with respect to the electrolyte window (E_g). 13

Figure 6: Illustration of a Na ion coordinated to two diglyme molecules. 13

Figure 7: Photograph of the in-situ Raman setup....20

Figure 8: (a) SEM image showing the surface of the few-layer graphene foam; scale bar, 20 μm. Inset, SEM image showing 3D foam; scale bar, 400 μm. (b) Representative Raman spectra acquired using 2.33 eV laser. (c) TEM characterization of thickness of graphenic sheets: scale bars, 5 nm. (d) Distributions of Raman spectra acquired over ~50 um x 50 um region (225 spectra) with respect to the relative 2D peak intensity. Reprinted with permission from A. P. Cohn, K. Share, R. Carter, L. Oakes and C. L. Pint, Nano Lett., 2016, 16, 543-548. Copyright 2016 American Chemistry Society. 21

Figure 9: (a) First 5 Galvanostatic charge-discharge profiles at current density of 0.2 A/g. (b) Galvanostatic charge-discharge profiles at current densities ranging from 1 A/g to 30 A/g with the corresponding cycling performance (c). Inset shows the linear relation between specific capacity and current density. (d) Extended cycling performed at current density of 12 A/g over 8000 cycles with selected Galvanostatic charge-discharge profiles (e). Inset, the decreasing overpotential with cycling. Reprinted with permission from A. P. Cohn, K. Share, R. Carter, L. Oakes and C. L. Pint, Nano Lett., 2016, 16, 543-548. Copyright 2016 American Chemistry Society. 22

Figure 10: Distributions of 225 Raman spectra (acquired over ~50um x 50um region using 2.33 eV laser) with respect to relative D peak intensity prior to testing (above) and after 8,000 Galvanostatic charge-discharge cycles (below) showing minimal cycling-induced degradation. Inset, individual spectrum acquired after cycling with D and G components fitted with Lorentzian peaks. Reprinted

with permission from A. P. Cohn, K. Share, R. Carter, L. Oakes and C. L. Pint, Nano Lett., 2016, 16, 543-548. Copyright 2016 American Chemistry Society. 24

Figure 11: (a) Galvanostatic charge-discharge curves at 0.2 A/g in 1M KPF_6 in diglyme. (b) Galvanostatic rate performance at current densities ranging from 1 to 10 A/g. Inset, corresponding charge-discharge curves. (c) Long-term stability test showing the Coulombic efficiency and capacity retention over 1000 cycles. (d) Comparing the x-ray diffraction pattern of the pristine carbon electrode (black) to the stage 1 GIC formed through cointercalation (red) and the final deintercalated state after 1000 galvanostatic cycles. (e) Corresponding comparison using Raman spectroscopy. Reproduced from Ref. 38 with permission from The Royal Society of Chemistry. ..25

Figure 12: (a) Microscope images showing the vibrant color change in the FLG during cointercalation; scale bar, 20 μm. (b) Galvanostatic discharge (~0.6 A/g) profile recorded during in-situ Raman measurements with band illustrations showing corresponding Fermi levels. (c) In-situ Raman intensity plots normalized to the initial G peak intensity acquired using 1.58 eV laser (top) and 2.33 eV laser (bottom) consisting of 40 spectra each with schematics depicting the setup shown on the right. Reprinted with permission from A. P. Cohn, K. Share, R. Carter, L. Oakes and C. L. Pint, Nano Lett., 2016, 16, 543-548. Copyright 2016 American Chemistry Society. 27

Figure 13: (a) In-situ Raman spectra (normalized) of FLG showing the highly-ordered staging reaction as measured using a 1.58 eV laser with (b) selected spectra and Lorentzian fits of G_C (blue line) and G_{UC} (red line) components. (c) Tracking the positions of the Raman G peak components (G_C shown in blue and G_{UC} shown in red) measured in situ with the 1.58 eV laser (triangles) and the 2.33 eV laser (circles) during the electrochemical intercalation reaction with the corresponding Galvanostatic discharge (~0.2 A/g) profile shown with respect to right y-axis (black line). Reprinted with permission from A. P. Cohn, K. Share, R. Carter, L. Oakes and C. L. Pint, Nano Lett., 2016, 16, 543-548. Copyright 2016 American Chemistry Society. 29

Figure 14: Raman spectra acquired using both a 1.58 eV and 2.33 eV laser of the stage 1 compound (~ 0V vs. Na/Na^+). 31

Figure 15: Evolving Raman spectra (normalized) acquired using 1.58 eV laser during electrochemical intercalation 32

Figure 16: Evolving Raman spectra (normalized) acquired using 2.33 eV laser during electrochemical intercalation. 32

Figure 17: Raman intensity plot (normalized) showing the intercalation and deintercalation reaction using the 1.58 eV laser. 33

Figure 18: Raman intensity plot (normalized) using the 2.33 eV laser showing both the G peak and 2D peak evolution during the electrochemical intercalation. The 2D peak red-shifts though stage 2 formation (a result of electron doping) and then is suppressed by stage 1 formation. 34

Figure 19: Illustration of the different stages showing the changing ratio between charged and uncharged graphene layers. 35

Figure 20: Daumas-Herold model showing the expanding and sliding of ion galleries, which serves to explain the smooth transition between stages. 35

Figure 21: Determining the stage number by examining the changing G_{UC} peak area during the initial staging reaction. 37

Figure 22: Images of "pop-top" transfer cell used for imaging air-sensitive Na metal samples 43

Figure 23: (a) Galvanostatic sodiation and then plating for carbon/Al current collector at 40 μA/cm^2 with carbon loading of 400 μg/cm^2. (b) Comparison of the Na nucleation overpotential for bare Al and carbon/Al current collectors at 40 μA/cm^2. (c) Cycling of bare Al and carbon/Al current collectors at 0.5 mA/cm^2 with 30 minute plating times with (d) enlarged voltage profiles. Reprinted with permission from A. P. Cohn, N. Muralidharan, R. Carter, K. Share and C. L. Pint, Nano Lett., 2017, 17, 1296-1301. Copyright 2016 American Chemistry Society. 44

Figure 24: Comparing initial cycling performance for bare Al electrodes and carbon/Al electrodes. We observe higher initial Coulombic efficiency for the carbon/Al electrodes followed by more stable performance. Testing was performed at 0.5 mA/cm^2 for 30 min plating times. 45

Figure 25: (a) Galvanostatic plating/stripping of Na on carbon/Al current collectors performed over a range of currents for 30 minute plating times. (b) Nyquist curves performed after initial plating cycles with 0.25 mAh/cm^2 loading. (c) Galvanostatic plating/stripping of Na on carbon/Al current collectors performed over a range of times (or loadings) at 1.0 mA/cm^2. (d) 50 cycles performed at 1 mA/cm2 with 12 mAh/cm2 loading of Na with the in set showing a corresponding potential profile (e) Coulombic efficiency and voltage hysteresis from over 1,000 plating/stripping cycles performed at 0.5 mA/cm^2 with 0.25 mAh/cm^2 loading. (f) Corresponding potential profiles of the 1st, 2nd, 499th, 500th, 999th and 1000th plating/stripping cycles. Figure 26: (a) Galvanostatic sodiation and then plating for carbon/Al current collector at 40 μA/cm^2 with carbon loading of 400 μg/cm^2. (b) Comparison of the Na nucleation overpotential for bare Al and carbon/Al current collectors at 40 μA/cm^2. (c) Cycling of bare Al and carbon/Al current collectors at 0.5 mA/cm^2 with 30 minute plating times with (d) enlarged voltage profiles. Reprinted with permission from A. P. Cohn, N. Muralidharan, R. Carter, K. Share and C. L. Pint, Nano Lett., 2017, 17, 1296-1301. Copyright 2016 American Chemistry Society. 46

Figure 27: Photographs (SB=2 mm) and micrographs (SB=500 μm) of Na metal on carbon/Al electrodes following plating at 0.5 mA/cm^2 for (a, b) 10 minutes, (c,d) 1 hour, (e, f) 4 hours, and (g,h) 8 hours. (i) SEM image of hexagon-shaped Na metal island (SB=20 μm). (j) EDS map showing coalescing Na metal islands (CB=50 μm). (k) Micrograph of plated Na metal film with 4 mAh/cm^2 loading (SB=20 μm). Figure 28: (a) Galvanostatic sodiation and then plating for carbon/Al current collector at 40 μA/cm^2 with carbon loading of 400 μg/cm^2. (b) Comparison of the Na nucleation overpotential for bare Al and carbon/Al current collectors at 40 μA/cm^2. (c) Cycling of bare Al and carbon/Al current collectors at 0.5 mA/cm^2 with 30 minute plating times with (d) enlarged voltage

profiles. Reprinted with permission from A. P. Cohn, N. Muralidharan, R. Carter, K. Share and C. L. Pint, Nano Lett., 2017, 17, 1296-1301. Copyright 2016 American Chemistry Society.....48

Figure 29: Bare Al electrode (10 mm diameter) with 2 mAh/cm^2 of plated Na metal performed at a rate of 0.5 mA/cm^2 (4 hour plating duration).....49

Figure 30: Carbon/Al electrode (10 mm diameter) plated with 2 mAh/cm^2 of plated Na metal performed at a rate of 4 mA/cm^2 (30 minute plating duration).....50

Figure 31: Illustration of the charged and discharged states of the anode-free Na battery utilizing the carbon/Al electrode. (b) Galvanostatic potential profiles of the full cell showing the first 5 cycles at 0.125 mA/cm^2 from 0.8 to 3.0 V with (c) the delivered specific energy of the first 40 cycles with respect to the combined active mass of both electrodes. Figure 32: (a) Galvanostatic sodiation and then plating for carbon/Al current collector at 40 μA/cm^2 with carbon loading of 400 μg/cm^2. (b) Comparison of the Na nucleation overpotential for bare Al and carbon/Al current collectors at 40 μA/cm^2. (c) Cycling of bare Al and carbon/Al current collectors at 0.5 mA/cm^2 with 30 minute plating times with (d) enlarged voltage profiles. Reprinted with permission from A. P. Cohn, N. Muralidharan, R. Carter, K. Share and C. L. Pint, Nano Lett., 2017, 17, 1296-1301. Copyright 2016 American Chemistry Society.....50

Figure 33: Na metal (1 mAh) plated from pre-sodiated FeS_2 on carbon/Al electrode during the first charging of the device. The image shows that, as expected, Na metal is formed during charging for the anode-free full cells. To open this cell without shorting the device, testing was performed in a split-flat cell in the glovebox for easy disassembly. 52

Figure 34: X-ray diffraction patterns for carbon black (TIMCAL Super C45) and synthesized hard carbon 54

Figure 35: Homemade adjustable film applicator. Blade height was adjusted using a feeler gauge set. Aluminum foil was placed onto a glass plate with isopropyl to keep the foil flat and well adhered. 55

Figure 36: Na metal flattened onto a stainless steel disc (left). Two coin cells prior to crimping (right)....55

Figure 37: Figure 2. (a,b) Electrochemical voltage profiles for Na ion insertion/extraction at 0.1 A/g for carbon black (left) and hard carbon (right) electrodes. (c,d) Na metal nucleation profiles at 40 μA/cm^2 on sodiated electrodes. (e,f) Slippage profiles for Na metal plating and stripping over 50 cycles at 0.5 mA/cm^2 on sodiated electrodes. 57

Figure 38: (a,b) Electrochemical voltage profiles for Na ion alloying/dealloying at 0.1 A/g for bismuth (left) and tin (right) electrodes. (c,d) Na metal nucleation profiles at 40 μA/cm^2 on sodiated electrodes. (e,f) Slippage profiles for Na metal plating and stripping over 50 cycles at 0.5 mA/cm^2 on sodiated electrodes. 59

Figure 39: (a,b) Electrochemical voltage profiles for Na ion insertion/extraction at 0.1 A/g for natural graphite (left) and activated carbon (right) electrodes. (c,d) Na metal nucleation profiles at 40 μA/cm^2 on sodiated electrodes. (e,f) Slippage profiles for Na metal plating and stripping over 50 cycles at 0.5 mA/cm^2 on sodiated electrodes. 62

Figure 40: Plating on carbon black nucleation layer in a half-cell configuration until exhaustion of the Na metal counter/reference electrode. Voltage profile shows stable plating over ~30 mAh/cm^2 of operation. Images show the full removal of all the Na metal from the stainless steel disc and the deposition of Na metal on the nucleation layer disc. 64

Figure 41: 50 cycles of plating and stripping on a carbon black nucleation layer in a half-cell configuration using a 10 hour rest between each plating and stripping step. The plating current was 1 mA/cm^2 and the plating capacity per cycle was 1 mAh/cm^2. The inset shows the voltage profile for 4½ of these cycles. The average Coulombic efficiency of 99.73% over these 50 cycles indicates that minimal Na is lost during the 10 hour resting period. 65

Figure 42: First-cycle voltage profiles for (a) Na-ion storage in hard carbon at 0.1 A/g and (b) Na metal plating on a 0.25 mg/cm^2 carbon black electrode at 0.5 mA/cm^2 for a capacity of 2 mAh/cm^2. 66

Figure 43: First-cycle voltage profiles for Na metal plating on a 0.25 mg/cm^2 carbon black electrode at 0.5 mA/cm^2 for a capacity of 0.5 mAh/cm^2. 67

Figure 44: (a) Dried precursor after ball milling. (b) Sintered $Na_3V_2(PO_4)_3$ discs in ceramic boat. 69

Figure 45: Cyclic voltammogram of $Na_3V_2(PO_4)_3$ half cell performed at 0.25 mV/s to 4.5 V vs. Na/Na^+ using an electrolyte of 1M $NaPF_6$ diglyme. 71

Figure 46: (a) SEM image of $Na_3V_2(PO_4)_3$ particles and corresponding (b) XRD pattern. (c) Voltage profile for $Na_3V_2(PO_4)_3$ half cell at C/6 (where C=117 mA/g). 71

Figure 47: Cycling of $Na_3V_2(PO_4)_3$ in a half-cell configuration performed at 0.5 mA/cm^2 (0.37C) for 100 cycles. 72

Figure 48: (a) Schematic diagram illustrating the difference between the Na-ion battery and the anode-free Na battery. (b) Specific energy comparison between battery configurations using different negative electrodes with a $Na_3V_2(PO_4)_3$ cathode; the anode-free approach using a nucleation layer is highlighted on the bottom. 73

Figure 49: (a) Schematic of the charged and discharged state of the anode-free cell. (b) Slippage profile for the first 20 cycles of the anode-free cell. Inset, nucleation spike during charging. 74

Figure 50: (a) 100-cycle voltage profiles for anode-free cells at 0.50 mA/cm^2 (above) and 0.25 mA/cm^2 (below). (b) Corresponding cycling capacity retention with decay curves plotted for guidance. 75

Figure 51: Nucleation spike voltage for anode-free cells cycled at 0.25 mA/cm^2 and 0.5 mA/cm^2. Above, example of the nucleation spike measurement. 76

Figure 52: Disassembled anode-free cells after 100+ cycles showing deposited Na metal (charged state) for devices cycled at (a) 0.5 mA/cm^2 and (b) 0.25 mA/cm^2. 77

Figure 53: (a) Projected cycling performance of an anode-free cell with (red line) and without (black line) an ion reservoir, assuming a plating-stripping Coulombic efficiency of 99.9%. (b) Projected cycle life where >80% of the initial capacity of an anode-free cell is retained, considering a range of plating-stripping Coulombic efficiencies and ion reservoir sizes, expressed as the excess of ions as a percent of the operating capacity. 81

Figure 54: Voltage profiles of 50 cycles of sodium metal plating and stripping on carbon black nucleation layers at a current of 1.0 mA/cm^2 with a plating capacity per cycle of 2.0 mAh/cm^2 performed (a) without a sodium surplus, using a voltage cutoff per cycle of 100 mV vs. Na/Na$^+$, and (b) after a surplus of 1.0 mAh/cm^2 of sodium was first plated (red line), using a 2.0 mAh/cm^2 capacity cutoff per cycle for the 50 cycles, and a final full strip (blue line) with a voltage cutoff of 100 mV vs. Na/Na$^+$ after the 50 cycles. The cumulative loss of charge is shown for both tests as Q_{Loss}. 82

Figure 55: Voltage profiles of 50 cycles of sodium metal plating and stripping on a carbon black nucleation layer at a current of 1.0 mA/cm^2 with a plating capacity per cycle of 2.0 mAh/cm^2 performed after a surplus of 1.0 mAh/cm^2 of sodium was first plated at a current of 0.1 mA/cm^2 (red line), using a 2.0 mAh/cm^2 capacity cutoff per cycle for the 50 cycles, and a final full strip (blue line) with a voltage cutoff of 100 mV vs. Na/Na$^+$ after the 50 cycles. The cumulative loss of charge is shown as Q_{Loss}. 84

Figure 56: XRD patterns of NVP before (bottom) and after (red) electrochemical reduction. The top pattern was acquired using an air-sensitive sample holder with the pattern from the holder baseline subtracted....85

Figure 57: Voltage profile of the first 3 cycles of the anode-free cell with ion reservoir performed at a current of 0.5 mA/cm^2 (~C/3)....85

Figure 58: Capacity of anode-free cell with ion reservoir over 230 cycles performed at a current of 0.5 mA/cm^2 (~C/3). The left inset shows the voltage profile for all cycles from cycle 2 to 180, and the right inset shows the voltage profile for all cycles from cycle 180 to 230. 86

Figure 59: Voltage profile from the cycling data shown in Figure 4 showing the beginning of the charging profile for all cycles from cycle 180 to 230. The spike that emerges corresponds to the nucleation of sodium metal. The delay in the emergence of this spike (as the surplus appears depleted by cycle 180) is due to the alignment of the NVP voltage plateau with the nucleation event, requiring the additional loss of sodium content from the NVP before the spike aligns with the flat plateau and becomes apparent. 88

List of Publications

1. A.P. Cohn*, W.R. Erwin*, K. Share, L. Oakes, A.S. Westover, R.E. Carter, R. Bardhan, and C.L. Pint, "All silicon electrode photo-capacitor for integrated energy storage and conversion," *Nano Letters*, 15, 2727-2731, (2015). (*equal contributing first authors)

2. A.P. Cohn, K. Share, R. Carter, L. Oakes, and C.L. Pint, "Ultrafast solvent-assisted sodium ion intercalation into highly crystalline few-layered graphene," *Nano Letters*, 16, 543-548 (2016).

3. A.P. Cohn, N. Muralidharan, R. Carter, K. Share, L. Oakes, and C.L. Pint, "Durable potassium ion battery electrodes from high-rate cointercalation into graphitic carbons," *Journal of Materials Chemistry A*, 4, 14954-14959, (2016).

4. A.P. Cohn, N. Muralidharan, R. Carter, K. Share, and C.L. Pint, "An anode-free sodium battery through in-situ plating of sodium metal," *Nano Letters*, 17, 1296-1301 (2017).

5. A.P. Cohn, T. Metke, J. Donohue, N. Muralidharan, K. Share, and C.L. Pint, "Rethinking sodium-ion anodes as nucleation layers for anode-free batteries," in preparation.

6. A.P. Cohn, N. Muralidharan, T. Metke, J. Donohue, K. Share, and C.L. Pint, "Extending the cycle life of anode-free batteries using a cathode with an ion reservoir," in preparation.

Chapter 1: Introduction

1.1 Motivation

In the push to decarbonize our electricity and transportation sectors, the continued reduction in the cost of electrical energy storage is critical. Intermittent renewable resources, such as solar and wind, require low-cost electrical energy storage to provide grid flexibility. Similarly, the wide-spread success of electric vehicles relies on their cost competitiveness, which hinges on the cost of their battery pack. Li-ion batteries have emerged as the best-suited technology to meet the demands of both of these applications. However, the cost-sensitivity of these applications and the concerns over the limited reserves of Li precursors motivates the need to develop alternative strategies for low-cost electrical energy storage.

1.2 History and overview of Li-ion batteries

In 1976, after extensive research at Exxon, Stanley Whittingham reported a breakthrough rechargeable electrochemical energy storage device.[1] By today's standards, Whittingham's motivation may appear out of place for a scientist working at an oil company, as he sought to develop technology that would enable "electric vehicle propulsion and the storage of off-peak and solar power". More than 40 years later, this goal remains a major motivation for continued research into new battery technologies, and is the driver of my thesis research.

Using a TiS_2 cathode, a Li metal anode, and an electrolyte of $LiClO_4$ dissolved in a mixture of ether solvents, dimethoxyethane (monoglyme) and tetrahydrofuran (THF), Whittingham demonstrated a high specific energy battery capable of reversible cycling. The cell as assembled was in a charged state. During discharge, the Li metal anode oxidized, releasing Li ions into the electrolyte that were inserted

into the layered TiS_2 cathode as it was reduced. The discharge of the cell would continue until either all of the Li metal was depleted or all of the TiS_2 was saturated with Li, forming $LiTiS_2$. This limit on the charge stored is referred to as the capacity, often expressed with respect to the mass of the electrodes. Here, the Li anode has a high capacity of 3860 mAh/g (owing to its exceptionally low atomic mass, 0.53 g/cm^3) and the TiS_2 cathode has a capacity of 240 mAh/g (corresponding to one electron per TiS_2). Accordingly, to balance this cell with respect to capacity, the mass of the cathode would need to be 16 times the mass of the anode. The voltage of the cell was determined by the difference in the electrochemical potential of the two electrodes, with the difference between Li metal and the $Ti^{3+/4+}$ redox couple providing a maximum of 2.5 V, but an average discharge of 2.12 V. The corresponding specific energy of this cell can be calculated with respect to the mass of the electrodes as follows:

$$E = \frac{Q_A Q_C}{Q_A + Q_C} \times (\mu_A - \mu_C)/e \qquad \text{(Eq. 1)}$$

where Q is the specific capacity of the anode or cathode, and μ is the electrochemical potential of the anode or cathode. The specific energy of Whittingham's Li cell was calculated as 480 Wh/kg with respect to the active materials, far surpassing the aqueous Ni-Cd batteries.[1, 2]

Despite Whittingham's monumental work, early efforts to commercialize rechargeable Li metal batteries proved problematic.[3] The high reactivity of the Li metal anode, with its electrochemical potential above the lowest unoccupied molecular orbitals (LUMO) band of the organic electrolyte led to the corrosion of the Li metal and the continuous growth of a solid-electrolyte interface (SEI) layer consisting of decomposed electrolyte. To compensate for the inadequate cycling efficiency (<99%), a large excess of Li was required. (Notably, even a 1% charge loss per cycle would causes a battery to lose over 60% of its capacity in 100 cycles.) Moreover, the lack of a host material to store the Li at the anode led to the rapid shape change of the Li, with the uneven deposition of Li during charging creating

needle-like growths (referred to as dendrites). Such dendrites posed a safety risk as they could short the cell, creating a fire hazard.

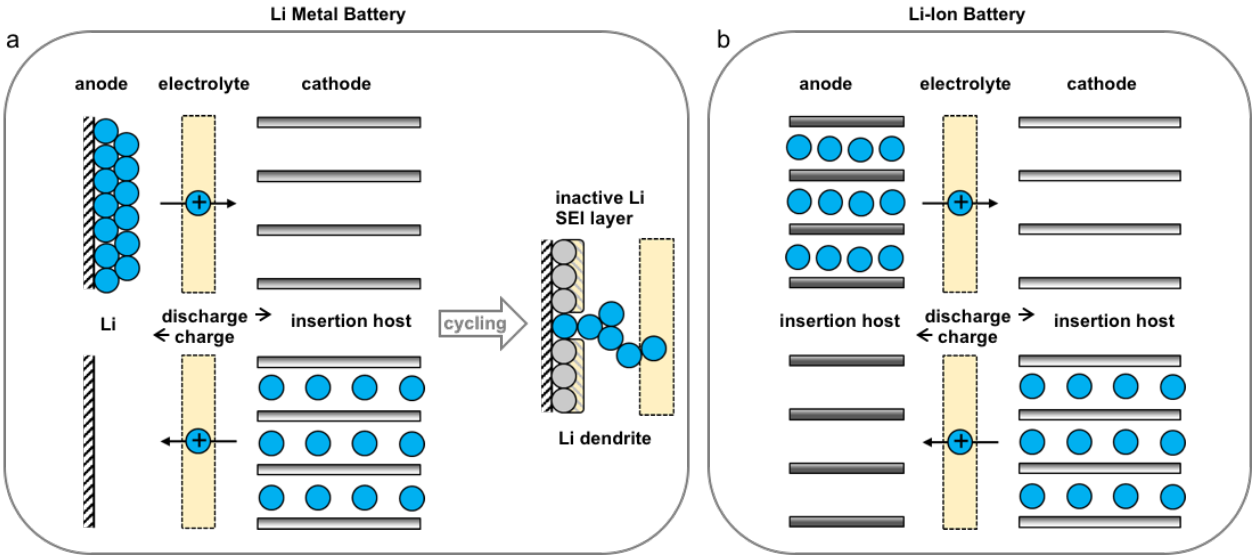

Figure 1: Battery configurations: (a) Li metal battery using Li metal anode, (b) Li-ion battery with anode host.

To solve the problems of the Li metal battery, researchers aimed to create Li-ion batteries, where Li ions could be transferred back and forth between two host materials without the use of Li metal.

Figure 1 shows illustrations of the Li metal and Li-ion batteries. In the case of the Li-ion battery, the use of a host material provides structure to the anode, alleviating the concerns with Li plating and enhancing the lifespan and operation stability of the Li-ion cells. However, the added mass of the host and the inevitable decrease in the electrochemical potential of the reaction at the host decreased the achievable specific energy. In addition, lithiated cathodes were required to provide the Li, as the new anode hosts did not contain Li. This requirement was met by John Goodenough and others, who developed a family of lithiated transition metal oxide cathodes of the form $LiMO_2$ (where M is a transition metal) that could supply cells with Li and offer higher operating voltages. Among the array of

materials studied, $LiCoO_2$ (abbreviated as LCO) emerged as the most favorable, with Sony selecting it for its Li-ion battery released in 1991.

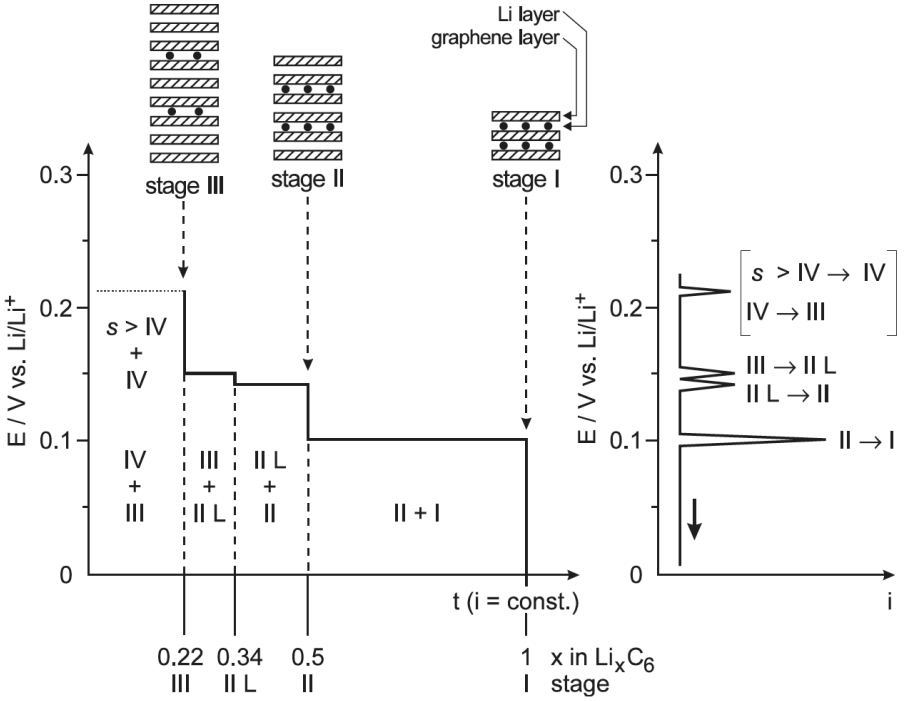

Figure 2: Illustration of the stage formation that occurs during the electrochemical intercalation of Li ions into graphite. Reproduced from Ref. 4 with permission. Copyright 1998, Wiley.

To serve as the anode host, researchers considered a range of materials, including Li-alloying metals, transition-metal oxides, and carbons.[4] Although the alloying metals, such as Al, could provide higher capacities, graphite proved to be the material of choice as it offered a higher electrochemical potential, a flat voltage profile, and eventually would allow for high reversibility. The process by which ions insert into graphite is known as intercalation. Intercalation into graphite and the resulting graphite intercalation compounds had already been extensively researched and characterized over the previous 50 years by material scientists, notably including the late Mildred Dresselhaus, because of their unique structures and electronic properties.[5] Following a remarkably ordered fashion, Li (as well as a number of

other known guest species) can electrochemically intercalate into graphite (illustrated in Figure 2). During this process, a series of stages are sequentially formed, where the Li ions occupy galleries between separated layers of graphene. Since it is thermodynamically favorable to maximize the out-of-plane distance between layers of intercalated guests, a long-range periodic ordering is maintained during this process. The stage number, which corresponds to the number of graphene layers between each gallery of guest species, decreases as more guest species are inserted. When the final stage 1 compound is reached, galleries of ions separate each graphene layer.

To enable the stable performance of the graphite anode, it was found that the intercalation of Li ions needed to be exclusive. When using solvents such as propylene carbonate (PC), however, researchers learned that solvated Li ions, rather than naked Li-ions, preferentially intercalated into the graphite. This cointercalation of ion and solvent proved to be highly detrimental. As the reaction proceeded, the electrochemical potential surpassed the LUMO energy level of the PC and caused it to decompose inside the graphite. As a result, the graphite was shown to undergo exfoliation, which was accompanied by a rapid drop in performance (as illustrated in Figure 3).[4, 6] To prevent cointercalation, researchers discovered that ethylene carbonate (EC), with its decreased cathodic stability (lower LUMO energy level), decomposed before inserting into the graphite. The SEI layer that was formed with EC conveniently allowed Li ion conduction into the graphite, but blocked solvent and further electron transfer to the electrolyte. In order to utilize EC in Li-ion cells, EC, which is a solid at room temperature, was mixed with less viscous carbonates, such as diethyl carbonate (DEC).

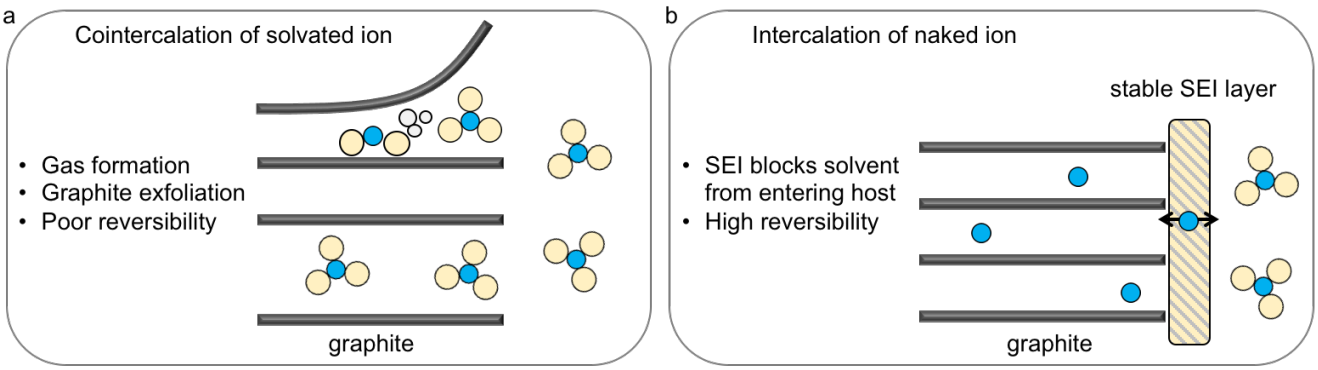

Figure 3: (a) Problematic cointercalatian of ion and solvent molecule, (b) intercalation of naked ion enabled by a stable SEI layer.

Progress with the graphite anode enabled the development of the Li-ion battery that is still used today. While a multitude of cathode materials are commercially used, such as $LiFePO_4$ (LFP) and $LiMn_2O_4$ (LMO), to serve a range of niche applications, the LCO-graphite cell has remained the industry standard for over twenty years.[7] Unlike the Li-TiS_2 cell introduced by Whittingham, the Li-ion battery is assembled in a discharged state. During charging, the $LiCoO_2$ cathode serves as the source of Li ions, with the Li deintercalating until $Li_{0.5}CoO_2$ composition is reached, providing a capacity of 136 mAh/g at a voltage of ~4 V vs. Li/Li^+. (Further delithiation of $Li_{0.5}CoO_2$ is avoided, as it results in irreversible structural changes and undesirable reactions with the electrolyte). At the anode, the Li ions intercalate into graphite, with a maximum capacity of 372 mAh/g (forming LiC_6) at an average potential of ~0.1 V vs. Li/Li^+. The specific energy of this pairing (using Equation 1) is ~390 Wh/kg. In practice, however, the specific energy of commercial cells is significantly reduced, as additional components are required, including: electrode additives (conductive carbon and polymer binders), polymer separator, metal foil current collectors (Cu at the anode and Al at the cathode), and the packaging (either pouch or can). Furthermore, cells lose approximately 10% of their capacity during the initial charging (due to the formation of the SEI layer and other irreversible processes), and excess anode material is used to prevent

the over-charging of the anode (which problematically results in the plating of Li metal on the anode). As a result, commercial LCO-graphite cells have specific energies of 150-200 Wh/kg.

While as of 2015, the LCO-graphite cells remained the dominant chemistry, the battery industry has now been moving towards $LiNi_XMn_yCo_{1-x-y}O_2$ cathodes (abbreviated as NMC accompanied by 3 numbers corresponding to the atomic ratios of the transition metals).[7] NMC 111 has emerged as an attractive replacement of LCO because it can deliver higher power and improved thermal stability (making it safer), while reducing the amount of cobalt required. Going forward, the trend appears to be to further increase the Ni content to achieve higher capacities, with so-called Ni-rich NMCs (532, 622 or 811).[8] In addition, for the anode, many battery companies are adding (or working to add) Si, which alloys with Li with a specific capacity of up to 4,200 mAh/g, to graphite to increase the capacity.[9] Nevertheless, despite our society's growing dependence on Li-ion technology, the cell-level chemistry and working principles have continued to remain relatively consistent over the last 27 years.

As this brief overview primarily serves as an introduction to the Li-ion battery to provide context to my dissertation work, it skips many of the important achievements that have led to the success of Li-ion technology. I recommend references 2, 4 and 6 for a more comprehensive perspective on the history and current status of Li-ion batteries.

1.3 Overview of Na-ion batteries

Until recently, the high cost of Li-ion batteries has mainly limited their usage to small applications, such as portable electronics and power tools, and excluded them from the larger applications that are more cost-sensitive, such as stationary electric storage and vehicles. This is now beginning to change as a recent decline in the price of Li-ion cells has been accompanied by a rise in the demand for stationary storage and electric vehicles. However, the rapid growth of the Li-ion battery market has led to concerns about the limited supply of Li. In addition, since most of the world's reserves of Li are in Chile and China, the United States may be vulnerable if it begins to rely heavily on Li-ion technology for its electric grid and transportation sector.

Accordingly, there is great interest in developing alternative high-performance batteries that do not use Li. Among the alternative chemistries considered, including: Na, K, Mg, Ca, and Al), Na stands out with its great abundance (approximately 1000 times as abundant as Li in the Earth's crust, with large reserves in the United States) and its similarity to Li (it is one row below Li on the periodic table). In addition to Na precursors (i.e. Na_2Co_3) being ~30 times cheaper than Li precursors (Li_2CO_3), the Cu foil negative current collector used in Li-ion batteries can be replaced, when using Na, by the significantly cheaper and lighter Al foil.[9, 10] This is possible because Na, unlike Li, does not electrochemically alloy with Al.

Prior to the successful development of the Li-ion battery, there was initial research conducted on Na intercalation electrodes.[11] However, research efforts were mainly abandoned as most of the focus shifted to Li-ion. Then around 2010, concerns about the limited reserves of Li and interest in stationary storage revived the Na-ion field.

Table 1: Comparison of Li and Na.

	Li	**Na**
Abundance in Earth's Crust (ppm)	20	23,000
Mass (g/mol)	6.9	23.0
Ionic Radius (pm)	76	102
E^0 vs. Li/Li^+ (V)	0	0.34

While Na-ion batteries are not expected to be capable of competing with Li-ion batteries with respect to specific energy, they have attracted attention for cost-sensitive applications, mainly stationary storage (but potentially transportation as well). The main disadvantages of Na (in contrast to Li) is its lower electrochemical potential (which limits the voltage of the cell), the larger ionic radius, and the heavier atomic mass (shown in Table 1).

The goal of Na-ion research has been to utilize the vast knowledge that has been accumulated in the Li-ion field to develop an analogous Na-ion battery. Unfortunately, this has not proved to be a straightforward endeavor. In comparison to Li cathodes, Na cathodes have shown lower operating voltages, lower specific capacities, and more complicated structural transformations during sodiation/desodiation.[12] Nonetheless, researchers have reported new layered transition-metal oxides,[13, 14] and polyanion compounds (including phosphates, fluorophosphates and hexacyanometalates)[15-19] capable of reversibly storing Na with promising specific capacities. Figure 4a shows many of the reported Na cathodes plotted with respect to their reported capacities and voltages.

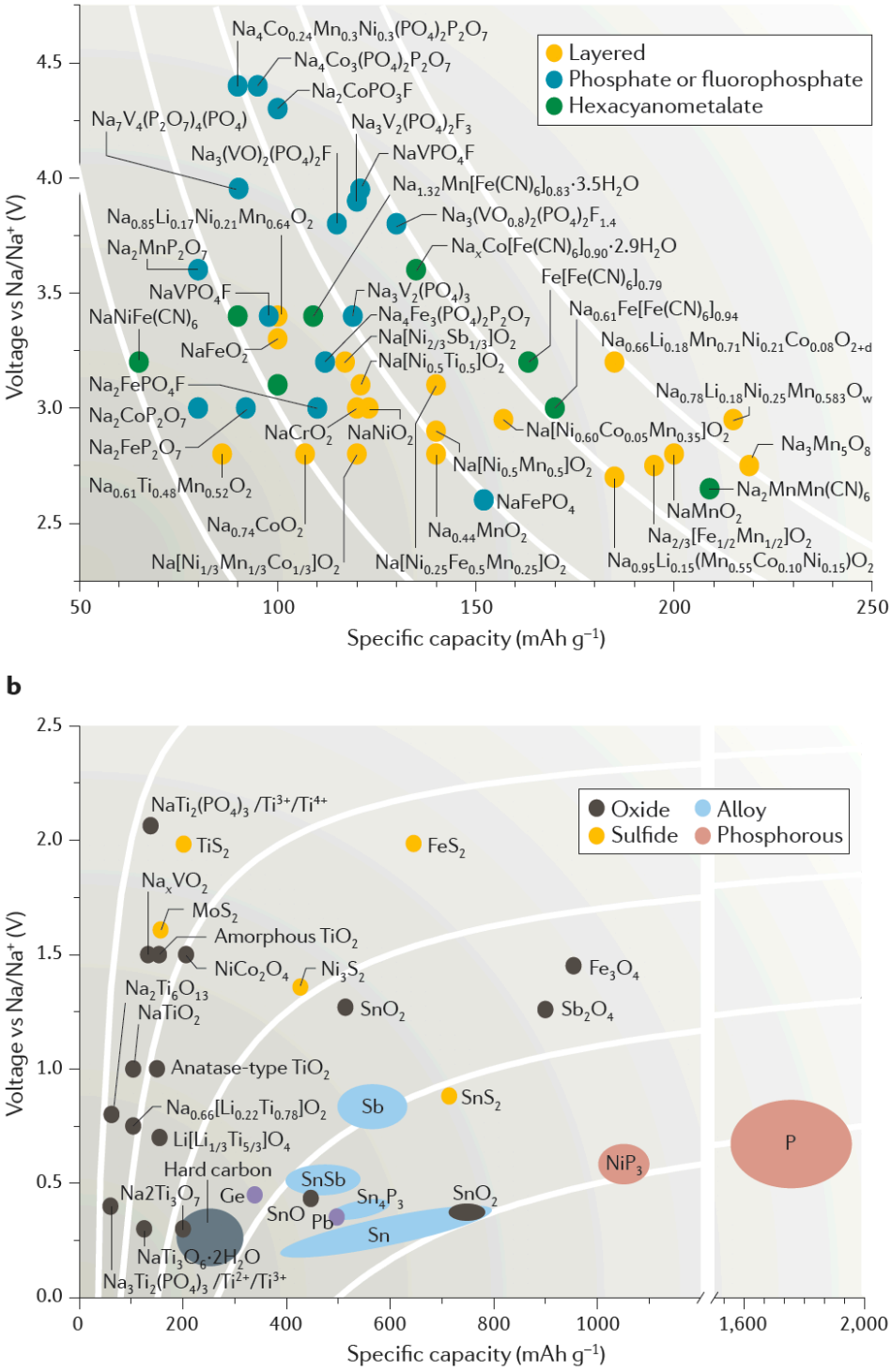

Figure 4: Operating voltage vs. specific capacity for Na-ion (a) cathodes and (b) anodes. The difference between the operating voltage of the anode and cathode determines the full-cell operating voltage. Reproduced from Ref. 9 with permission. Copyright 2016, Nature Publishing Group.

For the anode, the use of graphite was originally ruled out because unlike Li and K, Na was not found to form a binary graphite intercalation compound, such as LiC_6 or KC_8, with significant ion-storage capacity.[20] This critical drawback of transitioning to Na led to the investigation of a range of alternative anode materials. Non-graphitized carbon materials with an increased interlayer spacing known as hard carbons are considered the most practical option, offering up to 300 mAh/g capacity. However, their poor rate capabilities and large irreversibly capacities remain obstacles to Na-ion battery development. Alternatively, elements that alloy with Na, such as Sn, Pb, Bi and P, have been shown to offer higher specific capacities, but the large volumetric change during charging and discharging associated with the high capacity leads to mechanical degradation and poor cycling performance. Figure 4b shows many of the reported Na-ion anodes plotted with respect to their reported capacities and voltages. With a growing interest in Na-ion batteries, researchers continue to report new materials and materials structures, new electrolyte combinations, and new characterization approaches to progress the field.

Building on these advancements, a number of research groups have demonstrated full Na-ion cells. However, in the context of present day Li-ion technology, the current practicality of such Na-ion cells remains questionable, even for applications where cost is more important than performance. This is because the final cost per kilowatt-watt ($/kWh) of a cell is a function of both the specific energy (Wh/kg) as well as the material cost ($/kg). In this respect, the key shortcoming of these Na-ion batteries is the achievable specific energy. Choi and Aurbach highlighted this concern in their recent review article.[9] Comparing the expected cost of Na-ion pouch cell with a Li-ion pouch, they found that the Na-ion battery was actually expected to result in a 27% increase in cost per kWh. In light of this issue, it remains unclear if going forward Na-ion batteries can provide a sufficient material cost savings to compensate for their lower specific energy, and reach cell costs per kWh below state-of-the-art Li-ion

batteries.[9, 21] While rising Li prices can change this calculus, the cost of Li only currently accounts for less than 3% of the cost of a Li-ion cell. This is not to say that Na-ion battery research should be abandoned. Instead, I believe this shortcoming should be more directly addressed by the research community. In addition, there should be a greater divergence of research, with an increased focus on less conventional strategies to develop Li-ion analogues.[22, 23] This is the direction that I take in this dissertation.

Rather than developing Na-ion cells analogous to commercial Li-ion cells, I focus on the unique advantages of Na, in the attempt to develop a battery that offers higher performance than what can be achieved using the analogue strategy. This effort has led me to work on Na systems that are considered highly problematic for Li. Specifically, in this dissertation, I first examine the cointercalation of solvated Na ions into graphitic carbon. In contrast to the cointercalation of Li, which is known to lead to graphite exfoliation, Na ion cointercalation is shown to be highly reversible while offering exceptional rate capability. Then, I explore the electroplating of Na metal, and go on to develop a Na metal battery using an "anode-free" configuration. While such an approach results in instabilities with Li, I demonstrate a stable Na metal battery, achieving a specific energy competitive with current Li-ion cells.

Throughout this work I exclusively use the electrolyte 1M $NaPF_6$ in the linear ether diethylene glycol dimethyl ether (diglyme). While the focus of this work is on the electrode materials, it is important to initially highlight this electrolyte and provide a brief background on its use with Na.

1.4 Na, diglyme and $NaPF_6$

The downfall of Whittingham's original Li battery was the high reactivity of the Li metal with the electrolyte and the resulting unstable SEI layer. Na metal has also been reported to be highly unstable in electrolytes, with reports showing it to be even more problematic than Li. However, as I

discuss here, this was later shown to be solvable using the right electrolyte. The commonly noted disadvantage of Na for battery development is its electrochemical potential that is below Li (or less negative in terms of standard reduction potentials). It makes sense, however, that the lower electrochemical of Na can be advantageous for stable SEI formation. Examining the comparisons between the electrochemical windows of different solvents (shown in Figure 5), the ethers possess the highest cathodic stability (or highest LUMO energy level), meaning they require more energy to reduce. (This may be one of the reasons that Whittingham used ethers in his Li battery.) In this respect, the combination of Na with ethers provides a unique opportunity for increased stability.

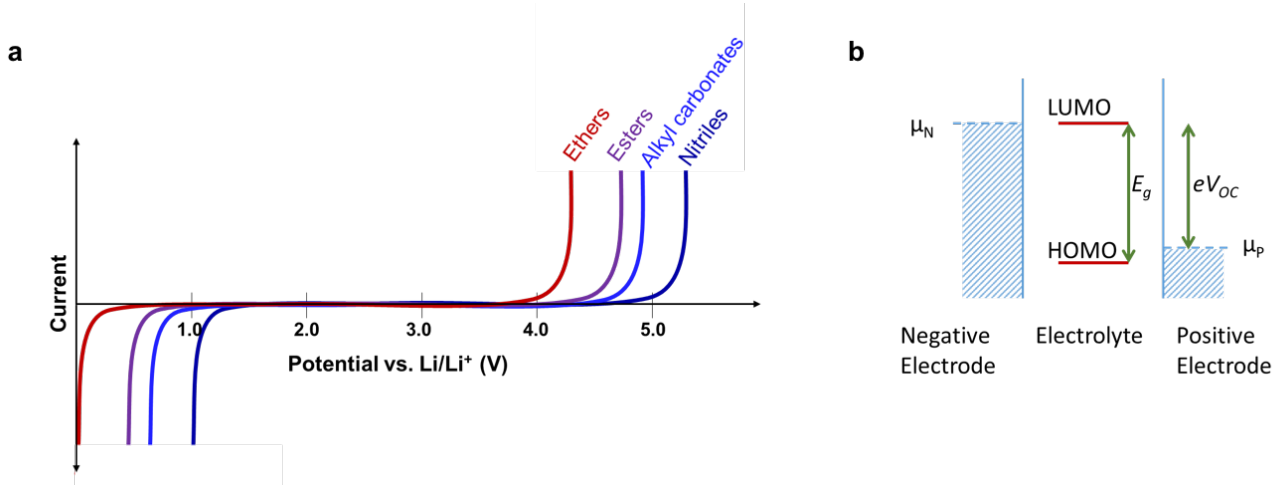

Figure 5: (a) Illustration of the electrochemical window of different solvent families using tetraalkyl ammonium salts. Adapted from Ref. 6 with permission of The Royal Society of Chemistry. (b) Illustration of the relative energies of the anode and cathode with respect to the electrolyte window (E_g).

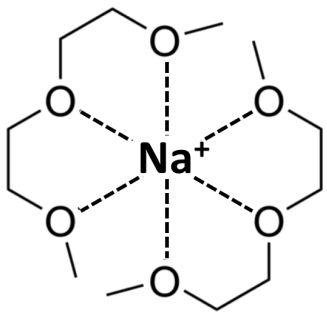

Figure 6: Illustration of a Na ion coordinated to two diglyme molecules.

In 2013, P. Hartmann (working with P. Adelhelm and J. Janek in Germany) reported a Na-O_2 cell using a diglyme electrolyte with surprisingly promising performance, concluding that Na-O_2 batteries may be preferable to Li-O_2 batteries. [23] The following year, B. Jache and P. Adelhelm reported that Na ions and solvent could reversibly cointercalate into graphite, again using a diglyme electrolyte.[24] In contrast to the early problems reported for cointercalation for Li-ion cells, the reversible cointercalation of diglyme and Na ions appeared to be due to the stability of the electrolyte, with significant decomposition of the electrolyte in the graphite not occurring. (Around this time, I was using a diglyme-based electrolyte to determine if Mg ions could be stored in carbon. However, I shifted my focus to Na cointercalation after reading the report by Jache and Adelhelm.)

In 2015, Z. Seh (working with Y. Cui at Stanford) reported an extensive study of the stability of Na metal in different electrolytes, testing different glymes and carbonates as well as five different Na salts. This work showed Na to be remarkably stable in monoglyme, diglyme, and tetraglyme when using a $NaPF_6$ salt. In contrast, Na was shown to be highly unstable in carbonates (as had been previously reported), and glymes using other Na salts, including: $NaN(SO_2CF_3)_2$, $NaSO_3CF_3$, $NaN(SO_2CF)_2$, and $NaClO_4$. To better understand their findings, x-ray photoelectron spectroscopy (XPS) with depth profiling was conducted on the SEI layers formed on the surface of the Na in these different electrolyte combinations. Seh found that the $NaPF_6$-glyme combination produced a very thin (~4 nm), compact SEI layer that mainly consisted of inorganic species (NaF and NaO_2). The underlying reason for this, as I understand it, goes as follows: PF_6^- or the impurities found in $NaPF_6$ (NaF is mentioned to be potentially important) preferentially reduce at the surface of the Na metal prior to the reduction of glymes (owing to their higher reductive stability). The reduction of the inorganic species first promotes the formation of a compact inorganic film that effectively passivates the Na metal, blocking further side reactions with the electrolyte. In contrast, the use of carbonates or other Na salts either favors the reduction of the solvent

first (creating a porous organic SEI layer that poorly passivates the Na) or still leads to the reduction of the salt first, but the SEI layer created by these other salts does not sufficiently prevent the continued reduction of the solvent. (At the time this paper was published, I was already experimentally realizing the stability of Na plating on/under graphene films using 1M $NaPF_6$ in diglyme electrolyte, but I was mainly unaware of why this electrolyte was special.)

Since the publication of these initial successes, diglyme-based electrolytes have been utilized for a range of different Na-ion electrodes. Notably, significant improvements in the cycle lifespan and rate capability have recently been shown for bulk pyrite,[25] bulk Sn,[26] bulk Bi,[27], and bulk Pb (K. Wolfe et al., manuscript in preparation).

1.5 Dissertation organization

This dissertation is organized as follows:

Chapter 2 presents the investigation of the cointercalation of Na ions with glyme molecules into graphitic carbon. Following initial work showing promising performance, the reaction is characterized using a few-layer graphene electrode, demonstrating remarkably high rate capability and cycle lifespan. In order to better understand the cointercalation phenomenon, in-situ Raman spectroscopic experiments are performed. New insight on the staging process is provided, including the Fermi level of the first and second stage compound.

Chapter 3 presents the first anode-free Na metal battery. It is shown that a nucleation layer can facilitate the stable plating and stripping of Na metal. Half-cell testing is shown, with 1000 stable cycles. Finally, a proof-of-concept full cell is demonstrated using a pre-sodiated pyrite cathode to achieve a specific energy of 400 Wh/kg, surpassing the theoretical value for the LCO-graphite cell and all previous reports on Na-ion batteries.

Chapter 4 presents a follow-up study comparing different nucleation layer compositions. A range of carbon materials and alloying metals are evaluated as nucleation layers. The initial Na-ion storage characteristics and the nucleation energetics are highlighted to be important in determining the performance of Na metal plating and stripping on these different nucleation layers. Carbon black is demonstrated to promote the best performance. In addition, it is shown that the problem of high first-cycle charge loss can be overcome by using the anode-free approach.

Chapter 5 presents the further development of the anode-free Na metal battery with a focus on the cathode and full-cell testing. The selection and synthesis of a carbon-coated $Na_3V_2(PO_4)_3$ cathode is described. Anode-free cells are shown to exhibit a high energy efficiency of 98% and a flat operating voltage at 3.35 V. In addition, cells cycled 100 times at 0.25 mA/cm^2 (~C/6) and 0.5 mA/cm^2 (~C/3), are shown to retain 70.4% and 82.5% of their initial capacity, respectively.

Chapter 6 presents the use of a cathode with a Na surplus to extend the cycle life of anode-free cells. Half-cell testing shows that a Na metal surplus facilitates improved Coulombic efficiency. In addition, the initial plating current is highlighted as a variable that can further control the cycle lifespan. Finally, a $Na_4V_2(PO_4)_3$ cathode is used to extend the lifetime of an anode-free cell to over 200 cycles.

Chapter 7 summarizes my work and discusses future opportunities.

Chapter 2: Cointercalation of Solvated Na Ions into Few-Layer Graphene

2.1 Introduction

In this chapter I investigate the cointercalation of Na ions and glyme into few-layer graphene foam electrodes using standard electrochemical testing and a series of in-situ Raman experiments in order to gain a better understanding of the cointercalation process.

2.2 Background

The most practical anodes for Na-ion batteries are considered to be hard carbons. However, their poor rate capabilities and large irreversible capacities remain to be critical obstacles to Na-ion battery development. In this respect, since power-balancing applications for the electric grid require energy storage devices that can provide fast response times and long cycle lives, the viability of Na-ion batteries for this important application remain in question.

However, an exciting new opportunity for Na-ion anodes was presented 2014. While the cointercalation of Li ions and solvent into graphite is considered a significant problem for Li-ion batteries, the cointercalation of Na ions and solvent has been reported to exhibit remarkable reversibility. This is especially of interest because graphite does not allow the intercalation of "naked" Na ions with any considerable capacity, and graphite is the industry-standard anode for Li-ion batteries. This successful cointercalation of Na ions and solvent into graphite was first reported in 2014 by B. Jache and P. Adelhelm, with 1000 cycles of stable operation.[24] A follow-up study conducted by H. Kim et al. in 2015 confirmed the finding, and also showed exceptionally fast kinetics.[28] Despite the impressive performance, many questions remained about this cointercalation process, and the origin of this promising performance. These questions include: (1) how does the graphite structure change during

cointercalation? (2) how does cointercalation differ from “naked” intercalation? (3) why are the kinetics so fast? (4) does an SEI layer form on the graphite? (5) why does exfoliation not occur?

In order to better understand the unique cointercalation into graphite, I first conducted initial electrochemical tests using a few-layer graphene foam electrode, and then carried a series of in-situ Raman experiments.

2.3 Methods

2.3.1 Material fabrication and characterization

Few-layer graphene (FLG) foam was grown using chemical vapor deposition (CVD) on a nickel foam substrate[29] (110 ppi from MTI) using a C_2H_2 precursor using a 1” quartz tube in a Lindberg/Blue tube furnace. The foam was heated to 850 ^oC under flows of A_r and H_2 and annealed for 10 minutes. Then C_2H_2 was introduced with respective flow rates of C_2H_2:H_2:A_r at 0.3:3:500 sccm for 6 minutes. Finally, the C_2H_2 flow was halted and the system was cooled to room temperature.

Raman measurements were performed using a Renishaw inVia Confocal Raman spectrometer. Micro-Raman maps were conducted using a 2.33 eV laser using an L50x object with a laser spot size of ~1.5 μm and a laser power of 350 μW. X-ray diffraction measurements were conducted using a using a Scintag XGEN 4000 system with a CuKα radiation source. SEM characterization was performed using a Zeiss MERLIN with GEMINI II SEM. TEM characterization was performed using a FEI Tecnai Osiris.

2.3.2 Electrochemical testing

Coin cells were assembled in an Ar filled glove box using a Na metal (Sigma Aldrich, 99.95%) counter/reference electrode, an electrolyte of 1M $NaPF_6$ (Strem, 99%) in anhydrous diglyme (Sigma Aldrich, 99.5%), and a Whatman grade GF/F glass fiber microfiber filter separator (Sigma Aldrich).

Galvanostatic measurements performed at 0.2 A/g and the extended cycling at 1 A/g were conducted using a MTI 8 channel battery analyzer. Higher rate measurements, including the 12 A/g cycling, were performed using a Metrohm Autolab multichannel electrochemical workstation. Cycling data presented was performed after initial device characterization (approximately 50 cycles). Working electrodes were composed of FLG on Ni foam with an active loading mass of ~100 μg/cm^2. The underlying Ni foam mass was not included in the active mass due to the negligible capacity of bare Ni foam.

2.3.3 In-situ Raman measurements

A homemade test cell was assembled using a thin glass coverslip window (see Figure 7) and an O-ring seal. The FLG foam was pressed under the window, with the separator and Na reference electrode below. Galvanostatic measurements were performed using a single-channel Metrohm Autolab. Raman measurements were performed using a Renishaw inVia Confocal Raman spectrometer with an L50x objective. The laser powers were kept below 700 μW for both the 1.58 eV and 2.33 eV lasers. Most measurements were performed using static scans over the range of 1000 to 2000 cm^{-1}. It should be noted that 2.33 eV laser locally prevented the deintercalation reaction from taking place, even when laser powers <50 μW were used. This was one of the reasons both lasers were used to probe the system. Also, during some in-situ experimentation, a D peak was observed to emerge at low voltages when using the 2.33 eV. We attribute this to the high sensitivity of the material to the laser as seen with the G peak enhancement. For this reason, caution was taken and lower laser powers were used. Individual, low-power measurements were also performed to confirm that no D peak was exhibited even when the device was fully shorted (0 V vs. Na/Na$^+$).

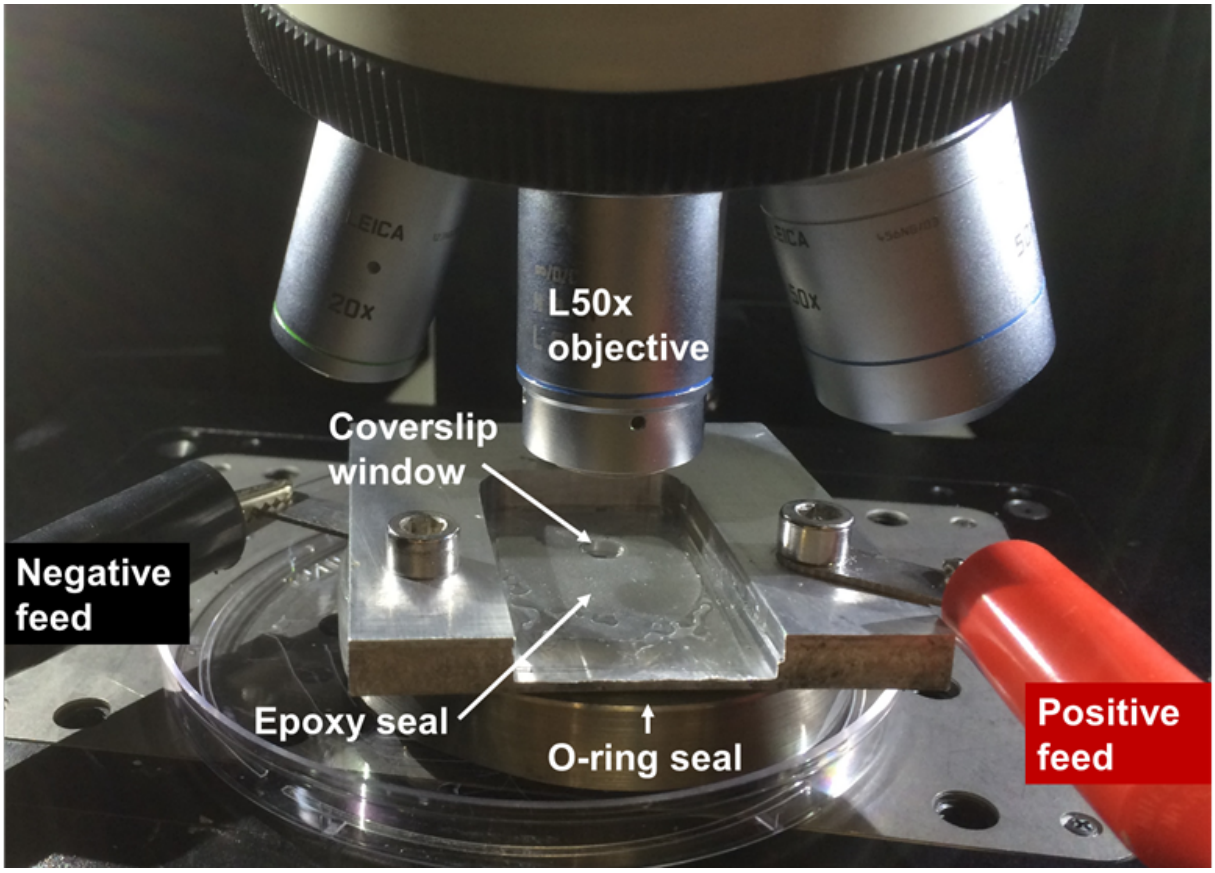

Figure 7: Photograph of the in-situ Raman setup.

2.4 Results and discussion

The surface of the graphene foam is shown in Figure 8a, with the inset showing the 3D structure. To characterize the graphene material grown on the Ni foam, a micro-Raman map was performed covering a ~50um x 50um region, collecting 225 spectra. Representative Raman spectra are presented in Figure 8b, with the three characteristic Raman peaks labeled. The D peak (~1350 cm^{-1}) arises from defect-activated in-plane breathing modes and corresponds to sp^3 carbon bonding, the G peak (~1580 cm^{-1}) arises from in-plane optical phonon modes at the Γ point and corresponds to sp^2 carbon bonding, and the 2D peak (~2700 cm^{-1}) arises from a two-phonon process that is sensitive to the electronic band structure.[30, 31] The line shape, position, and relative intensity of the 2D peak can be used to approximate

the layer thickness, and the D/G relative intensity ratio is used as a measure of carbon crystallinity. In this manner, the presented spectra correspond to highly crystalline, few-layer graphene typical of previous reports of graphene grown on nickel.[29, 32] High-resolution transmission electron microscopy (TEM) (Figure 8c) show sheets consisting of 2-10 graphene layers.

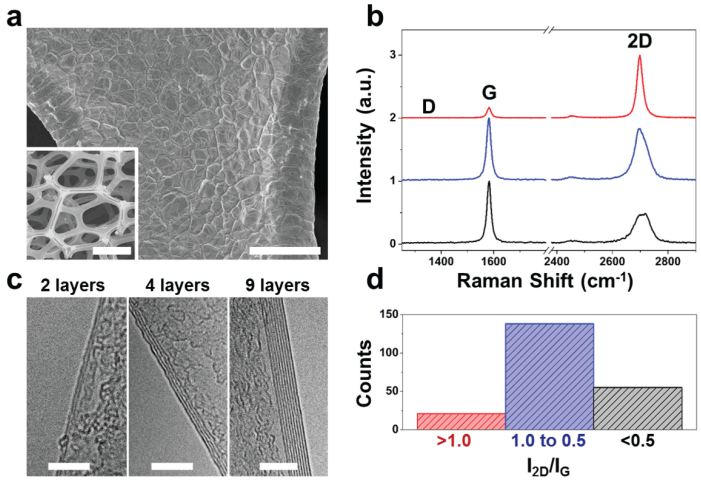

Figure 8: (a) SEM image showing the surface of the few-layer graphene foam; scale bar, 20 μm. Inset, SEM image showing 3D foam; scale bar, 400 μm. (b) Representative Raman spectra acquired using 2.33 eV laser. (c) TEM characterization of thickness of graphenic sheets: scale bars, 5 nm. (d) Distributions of Raman spectra acquired over ~50 um x 50 um region (225 spectra) with respect to the relative 2D peak intensity. Reprinted with permission from A. P. Cohn, K. Share, R. Carter, L. Oakes and C. L. Pint, Nano Lett., 2016, 16, 543-548. Copyright 2016 American Chemistry Society.

2.3.2 Electrochemical testing

Galvanostatic cycling was carried out at varying rates in the potential range of 0.01 to 2.0 V vs. Na/Na^+. The first 5 cycles performed at 0.2 A/g presented in Figure 9a show stable cycling after initial Na^+ insertion with a reversible capacity of ~150 mAh/g, suggesting a stoichiometry we propose to be ~$Na(Diglyme)_xC_{15}$, which is in agreement with previous reports on chemically derived stage 1 Na^+ ternary graphite intercalation compounds (GIC).[33] We attribute the initial irreversible capacity to the partial reductive decomposition of the electrolyte. Whereas the overall shape of the charge-discharge

profiles closely matches previously reported curves for diglyme cointercalation into natural graphite,[24, 28] testing the FLG material at higher rates (Figure 9b and c) demonstrates rate capability exceeding previously tested carbon materials. Remarkably, the FLG foam electrode maintains ~125 mAh/g (~80% maximum capacity) at a rate of 10 A/g and ~100 mAh/g (~65% maximum capacity) at a rate of 30 A/g (corresponding to a ~12 second charge). In comparison, Lin *et al.* utilizes solvent cointercalation for Al-ion batteries and report up to 4 A/g rate capability (~ 60 second charge) with 50% capacity drop, and Kim *et al.* report ~50% capacity drop at 10 A/g for Na-ion cointercalation into graphite.[28, 34] We attribute the exceptional rate capability observed to a combination of fast diffusion through the electrode, the high surface area of the graphene foam, and the lack of desolvation at the electrode-electrolyte interface which has been shown to be rate-limiting in other systems.[35]

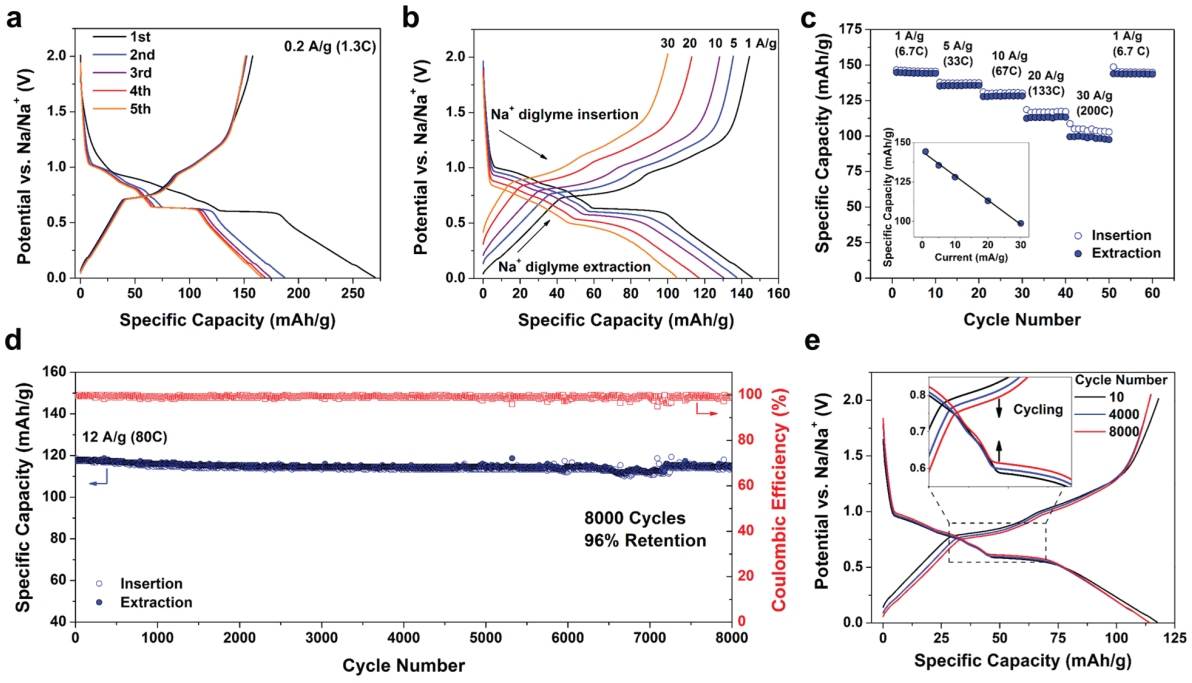

Figure 9: (a) First 5 Galvanostatic charge-discharge profiles at current density of 0.2 A/g. (b) Galvanostatic charge-discharge profiles at current densities ranging from 1 A/g to 30 A/g with the corresponding cycling performance (c). Inset shows the linear relation between specific capacity and current density. (d) Extended cycling performed at current density of 12 A/g over 8000 cycles with selected Galvanostatic charge-discharge profiles (e). Inset, the decreasing overpotential with cycling. Reprinted with permission from A. P. Cohn, K. Share, R. Carter, L. Oakes and C. L. Pint, Nano Lett., 2016, 16, 543-548. Copyright 2016 American Chemistry Society.

In order to evaluate the reversibility of this process, extended cycling was performed (Figure 9d). Over a span of 8,000 cycles, the FLG electrode retained 96% of its initial capacity with an average Coulombic efficiencies of 99.2%. We also observed a decreasing overpotential with cycling (Figure 9e), which may indicate a slight change in the electrode morphology or SEI layer. In contrast to the avoided cointercalation of Li and solvent into graphite, the near-perfect capacity retention observed here indicates that exfoliation[36] is not an issue.

2.3.3 Post-cycling characterization

To examine the impact of cycling on the carbon structure, a second micro-Raman map was performed covering a ~50um x 50um region, collecting 225 spectra from a FLG electrode after 8000 cycles. Figure 10 presents distributions of the relative D peak intensities found in the pristine and the post-cycling FLG. We see that even after 8,000 cycles, the distribution of I_D/I_G ratios remains centered < 0.05. This demonstrates that a high degree of crystallinity is preserved through cycling and explains the near-perfect capacity retention. In contrast, the I_D/I_G ratio in graphene has been reported to increase to >1.0 after only 5 lithiation cycles.[37] We attribute the retention of crystallinity to weaker ion – host lattice interactions due to solvent screening. This is in comparison to intercalation occurring after desolvation at the electrode-electrolyte interface, where stronger interactions between ions and the crystalline carbons (*e.g.* LiC_6) yields enhanced electrode degradation and irreversibility over successive cycling.

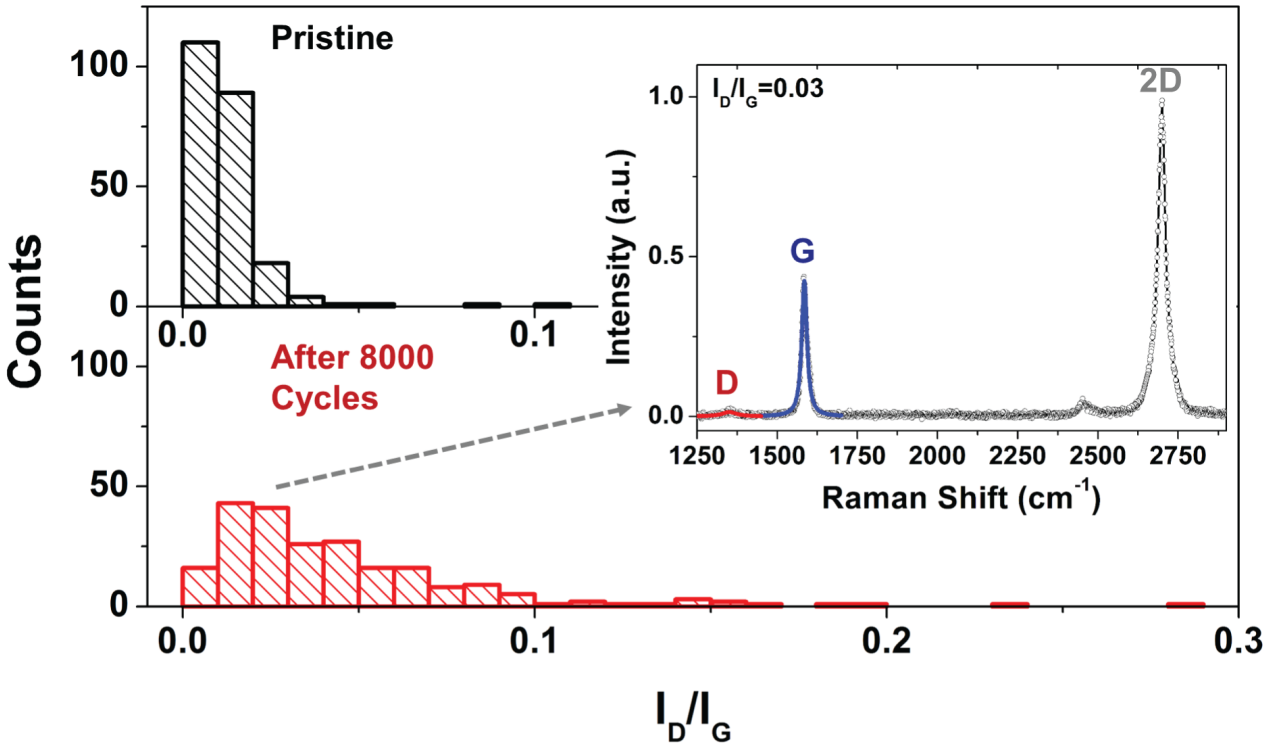

Figure 10: Distributions of 225 Raman spectra (acquired over ~50um x 50um region using 2.33 eV laser) with respect to relative D peak intensity prior to testing (above) and after 8,000 Galvanostatic charge-discharge cycles (below) showing minimal cycling-induced degradation. Inset, individual spectrum acquired after cycling with D and G components fitted with Lorentzian peaks. Reprinted with permission from A. P. Cohn, K. Share, R. Carter, L. Oakes and C. L. Pint, Nano Lett., 2016, 16, 543-548. Copyright 2016 American Chemistry Society.

2.3.4 Cointercalation of K ions

While the focus of this thesis is my work developing Na-ion and Na metal batteries, it is worth noting that I demonstrated that K ions can similarly cointercalate into graphitic materials using gylme solvents. This finding shows that cointercalation electrodes can be used to develop both high-rate Na-ion and K-ion batteries, broadening the selection of cathode materials. Figure 11 shows the K-ion cointercalation with a reduced capacity and rate capability in comparison to K. X-ray diffraction measurements and Raman characterization show that electrodes retain their crystallinity after 1000 cycles. Details on this work can be found in our 2016 publication.[38]

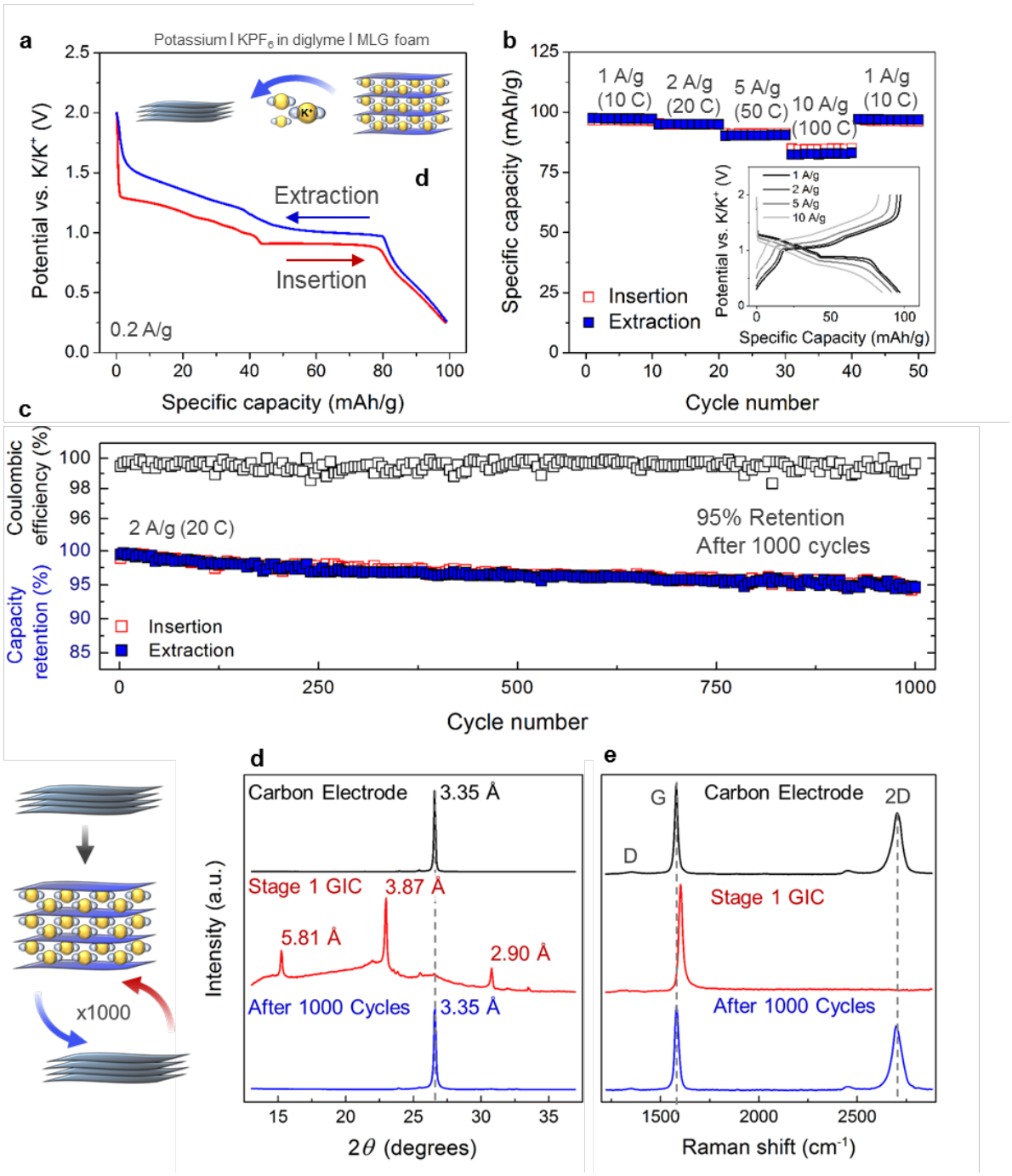

Figure 11: (a) Galvanostatic charge-discharge curves at 0.2 A/g in 1M KPF_6 in diglyme. (b) Galvanostatic rate performance at current densities ranging from 1 to 10 A/g. Inset, corresponding charge-discharge curves. (c) Long-term stability test showing the Coulombic efficiency and capacity retention over 1000 cycles. (d) Comparing the x-ray diffraction pattern of the pristine carbon electrode (black) to the stage 1 GIC formed through cointercalation (red) and the final deintercalated state after 1000 galvanostatic cycles. (e) Corresponding comparison using Raman spectroscopy. Reproduced from Ref. 38 with permission from The Royal Society of Chemistry.

2.3.5 In-situ Raman characterization

To further understand the mechanisms associated with this fast and stable reaction, we performed *in-situ* Raman spectroscopy to optically probe the FLG material during Na-diglyme cointercalation. While performing these tests, a vibrant color change was observed in the carbon foam which is valuable to discuss prior to the Raman results. By optically monitoring the reaction in real time,[39] it was possible to correlate the color changes in the material to the electrochemical potential as shown by the images of the FLG foam (Figure 12a). A video (available in the supporting information of our 2016 publication[40]) shows this color change over four successive cycles. The FLG foam initially appears grey/silver with the color darkening to black as the potential reaches the start of the pronounced plateau. Then, individual grains begin switching to red/orange, with most of the grains taking on this color by the end of the plateau. Finally, by full sodiation, the color gradually transitions to yellow. Upon Na removal, these color changes repeat in reverse order and successive cycles show matching color transitions. Notably, insertion of Na ions into FLG with capacity of 150 mAh/g corresponds to an electron concentration of ~2.5×10^{14} cm^{-2} for each graphene layer, which is a much higher electron concentration than is achievable using a top-gate method.[41-43] As a result, the Fermi level shift is sufficient enough to block optical interband absorption and increase the transparency[44, 45] for photons with $\hbar\omega < 2E_F$, with greater description of this phenomenon for Li intercalated ultrathin graphite described by Bao *et al*.[44] With this in mind, we attribute the red/orange and yellow colors to the increased transmittance of the graphene material for lower-energy visible photons and the subsequent reflection of the transmitted photons back off the Ni substrate.

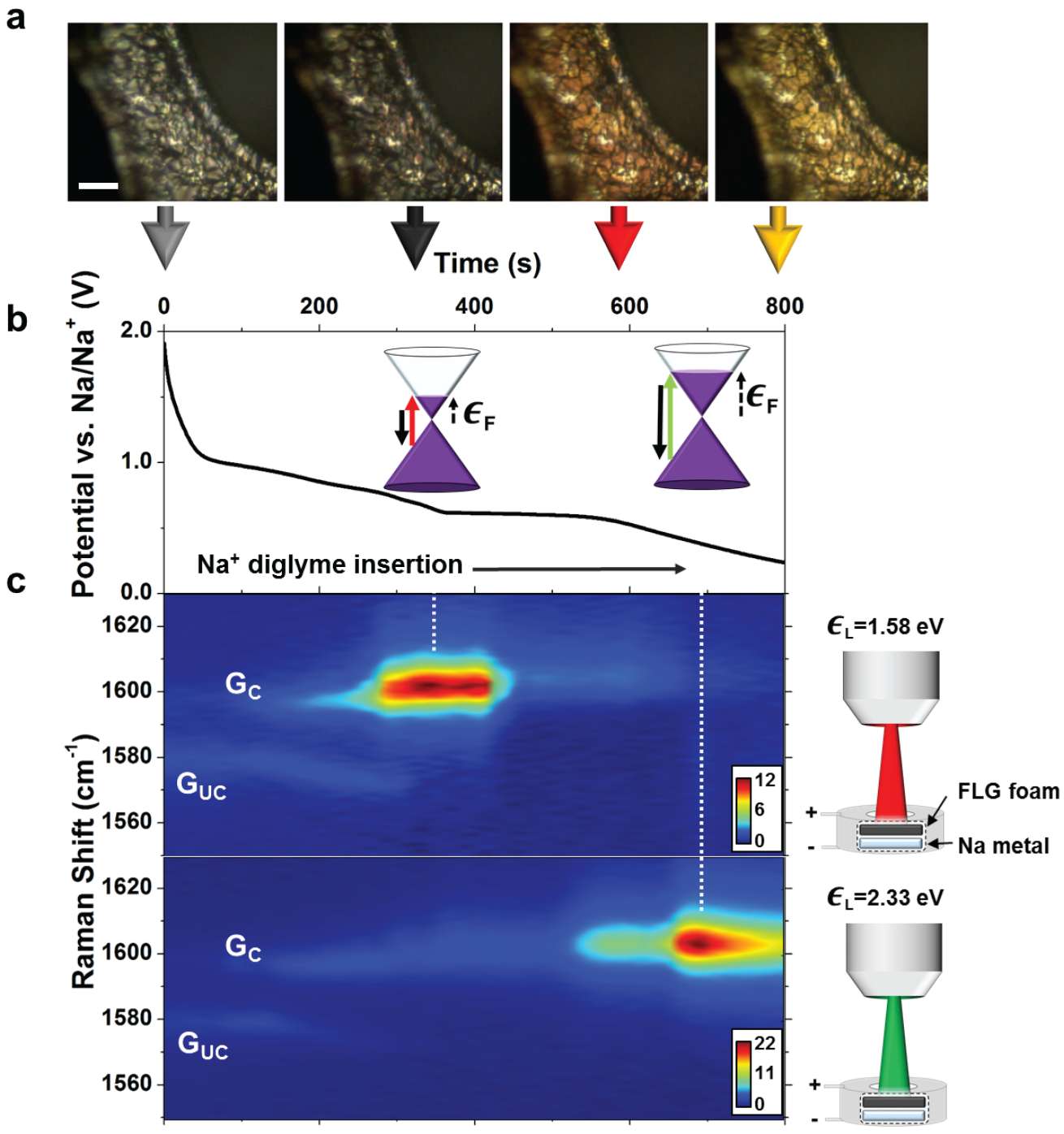

Figure 12: (a) Microscope images showing the vibrant color change in the FLG during cointercalation; scale bar, 20 μm. (b) Galvanostatic discharge (~0.6 A/g) profile recorded during in-situ Raman measurements with band illustrations showing corresponding Fermi levels. (c) In-situ Raman intensity plots normalized to the initial G peak intensity acquired using 1.58 eV laser (top) and 2.33 eV laser (bottom) consisting of 40 spectra each with schematics depicting the setup shown on the right. Reprinted with permission from A. P. Cohn, K. Share, R. Carter, L. Oakes and C. L. Pint, Nano Lett., 2016, 16, 543-548. Copyright 2016 American Chemistry Society.

To gain more insight, *in-situ* Raman measurements were conducted. Figure 12c presents intensity plots comprised of 40 spectra (with 20 s exposure times) for both 1.58 eV (785 nm) and 2.33 eV (532 nm) laser excitations acquired during the electrochemical intercalation (at ~0.6 A/g) of FLG shown in Figure 12B. For 1.58 eV excitations, a single G peak (~1580 cm^{-1}) is initially observed which is denoted as G_{UC} - representing the G mode of an uncharged graphene layer. After ~100 s, a second, blue-shifted G peak emerges at ~1600 cm^{-1}, which is denoted as G_C, as it corresponds to the G mode of a charged graphene layer. This G peak splitting is characteristic of graphite staging reactions,[5, 44, 46-48] arising from the presence of both charged graphene layers in contact with an intercalant layer and uncharged graphene layers that are shielded. Accordingly, the appearance of the G_C peak signifies the beginning of the staging process. As the reaction continues, the intensity of the G_C peak begins to drastically increase as the G_{UC} peak red-shifts and disappears, all coinciding with the time when the pronounced voltage plateau is reached electrochemically. The disappearance of the G_{UC} layer indicates the absence of uncharged layers, which takes place when the reaction reaches a stage 2 compound (where the stage number corresponds to the number of graphene layers in between each intercalant layer). At this point, we see a rapid enhancement of the Gc peak intensity, reaching 12x the initial G_{UC} peak intensity. This dramatic change in the G peak intensity can be attributed to the Pauli blocking of destructive interference Raman pathways[43] that takes place when the Fermi level approaches half the excitation laser energy. Accordingly, we can use this understanding to estimate the Fermi level of the stage 2 compound to be ~0.8 eV, which corresponds to a work function of ~3.8 eV. As the reaction continues to progress, the G_C peak intensity fades and then is completely suppressed by 800 s, which can be attributed to Pauli blocking of all of the G-peak Raman pathways. For this reason, we chose to switch to a 2.33 eV laser to better probe the later portion of the reaction. For the 2.33 eV excitations, G peak splitting similarly occurs but the rapid G_C peak enhancement is delayed until after the pronounced

plateau reaction is completed. At this point, which corresponds to a stage one compound, we observe 22x enhancement and can again estimate the Fermi level as ~1.2 eV, corresponding to a work function of ~3.4 eV. In comparison to our results, the stage 1 LiC_6 compound has been reported with E_F ~ 1.5 eV.[49] Other Raman studies have reported stage 1 $FeCl_3$ intercalated FLG to exhibit E_F ~ 0.9 eV, and stage 2 and stage 1 ammonium persulfate/sulfuric acid intercalation compounds to exhibit E_F ~ 1.0 eV and E_F ~ 1.2 eV, respectively.[46, 50] However, our work is the first to utilize G peak enhancement during *in-situ* electrochemical testing to monitor the Fermi level of a progressing intercalation reaction.

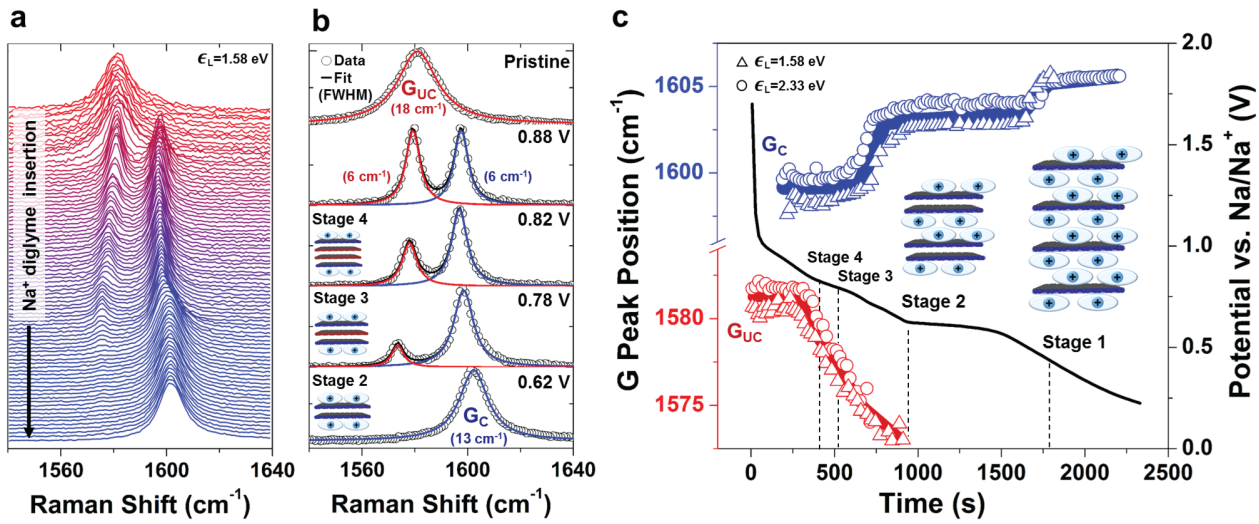

Figure 13: (a) In-situ Raman spectra (normalized) of FLG showing the highly-ordered staging reaction as measured using a 1.58 eV laser with (b) selected spectra and Lorentzian fits of G_C (blue line) and G_{UC} (red line) components. (c) Tracking the positions of the Raman G peak components (G_C shown in blue and G_{UC} shown in red) measured in situ with the 1.58 eV laser (triangles) and the 2.33 eV laser (circles) during the electrochemical intercalation reaction with the corresponding Galvanostatic discharge (~0.2 A/g) profile shown with respect to right y-axis (black line). Reprinted with permission from A. P. Cohn, K. Share, R. Carter, L. Oakes and C. L. Pint, Nano Lett.*, 2016, 16, 543-548. Copyright 2016 American Chemistry Society.*

Next, in-situ Raman measurements were conducted using a decreased rate to better monitor the staging processes. Consecutive Raman spectra taken during insertion with a 1.58 eV laser (Figure 13A) demonstrates a transition from all uncharged graphene layers to all charged graphene layers, with representative spectra and Lorentzian peak fits shown in Figure 13B. Peak positions for *in-situ*

measurements are plotted in Figure 13C for both laser energies with respect to the charging time (using a rate of ~0.2 A/g). The staging process, as observed through Raman measurements, is distinctly different from the lithiation of FLG[44, 51] and graphite[48], which are useful well-studied benchmarks due to their similarities to our system and their comparatively limited rate capability and cycling. These lithiation reactions exhibit an initial blue-shift in a single G-peak corresponding to the formation of a dilute stage 1 compound, followed by peak broadening and splitting into two poorly defined peaks (staging >2). Finally the G peaks evolve into a broad (FWHM ~ 60 cm^{-1}) peak by stage 2 and then disappear by stage 1.[48] In contrast, we do not observe any initial dilute staging and the progressing spectra show extremely sharp, well-resolved Lorenztian peaks through stage 2 formation, indicating a more ordered staging process. Accordingly, these findings demonstrate that minimal in-plane deformation of the lattice occurs during the reaction, which is likely a result of the weak interaction of the ion with the host, and appears to be another key factor facilitating the fast in-plane diffusion and improved cycling stability.

While the narrowing of the G peak can be simply attributed to increasing structural order, it has also been ascribed to increased phonon lifetimes in charge graphene—a result of blocking the decay of G-mode phonons into electron-hole pairs that takes place during the Kohn anomaly process.[30] The blocking of this renormalization process also explains the stiffening of the G mode that has been shown to occur during both electron-doping and hole-doping.[30, 41, 43, 52] Therefore, the G peak is a signature of the charge present on the graphene layers which can identify the staging processes during intercalation. In Figure 5C, after the initial blue-shift (Δpos ~ 18 cm^{-1}) in the position of the G_C peak, there are two additional blue-shifts (Δpos ~ 4 cm^{-1} at ~ 700 s and Δpos ~ 2 cm^{-1} at ~ 1700 s) with increasing Na insertion. The initial blue-shift (the formation of the G_C peak) indicates the start of the staging reaction, the second blue-shift occurs just before the loss of the G_{UC} peak and the start of the pronounced voltage

plateau in the electrochemical data. This shift was not anticipated, since one would expect the charge on the FLG layers to maintain relatively consistent through stage 2 formation.[5] We attribute this to a reconfiguration of the Na^+-solvent intercalated layer that appears to take place prior to stage 2 formation. The last blue-shift, which takes place before the G_C peak disappears in the 1.58 eV laser data is attributed to the formation of a stage 1 compound where each individual graphene layer is surrounded on both sides by an intercalant layer. The G_C peak at this point, as measured using 2.33 eV excitations, displays a sharp, but noticeably asymmetric, line shape (shown in Figure 14) which has been reported to be a signature of stage 1 GICs.[53] Additional in-situ Raman data showing spectra acquired with the 2.33 eV laser, the deintercalation reaction, the evolution of the 2D peak are presented in Figure 15-Figure 18, and illustrations of the different stages and the model for stage transitions are included as Figure 19 and Figure 20, respectively.

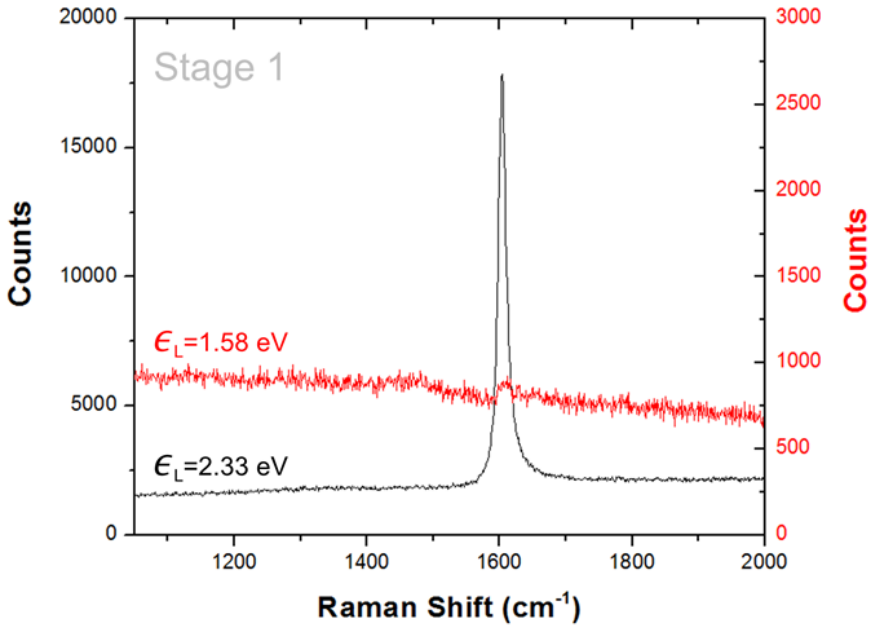

Figure 14: Raman spectra acquired using both a 1.58 eV and 2.33 eV laser of the stage 1 compound (~ 0V vs. Na/Na^+).

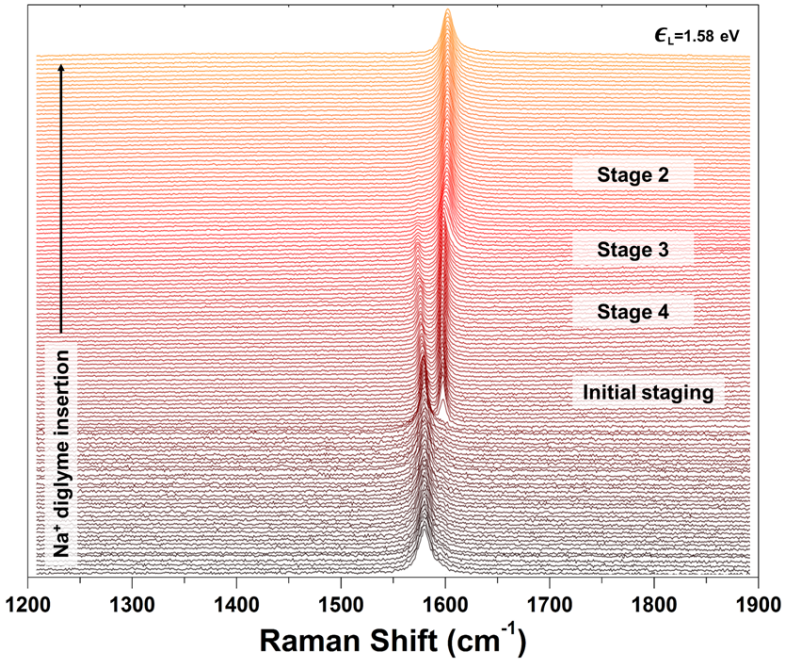

Figure 15: Evolving Raman spectra (normalized) acquired using 1.58 eV laser during electrochemical intercalation

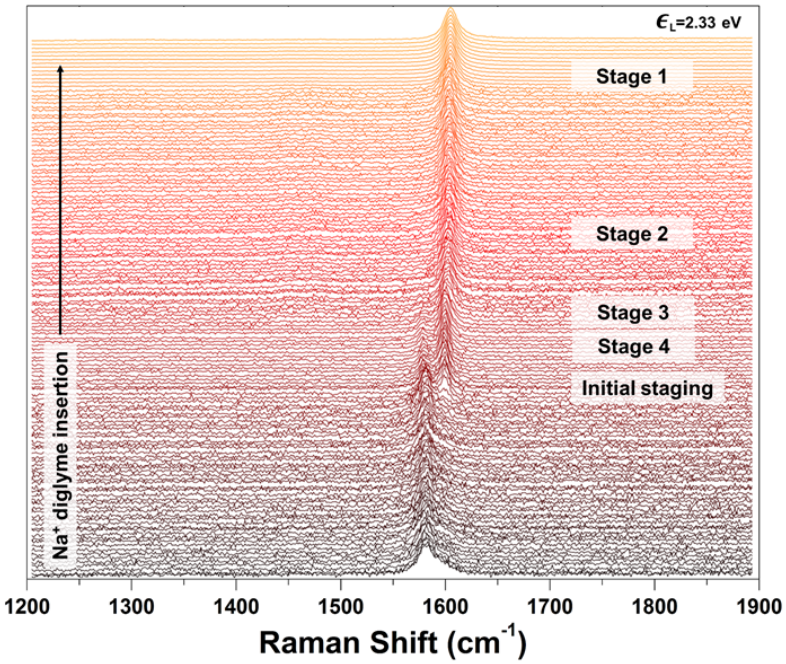

Figure 16: Evolving Raman spectra (normalized) acquired using 2.33 eV laser during electrochemical intercalation.

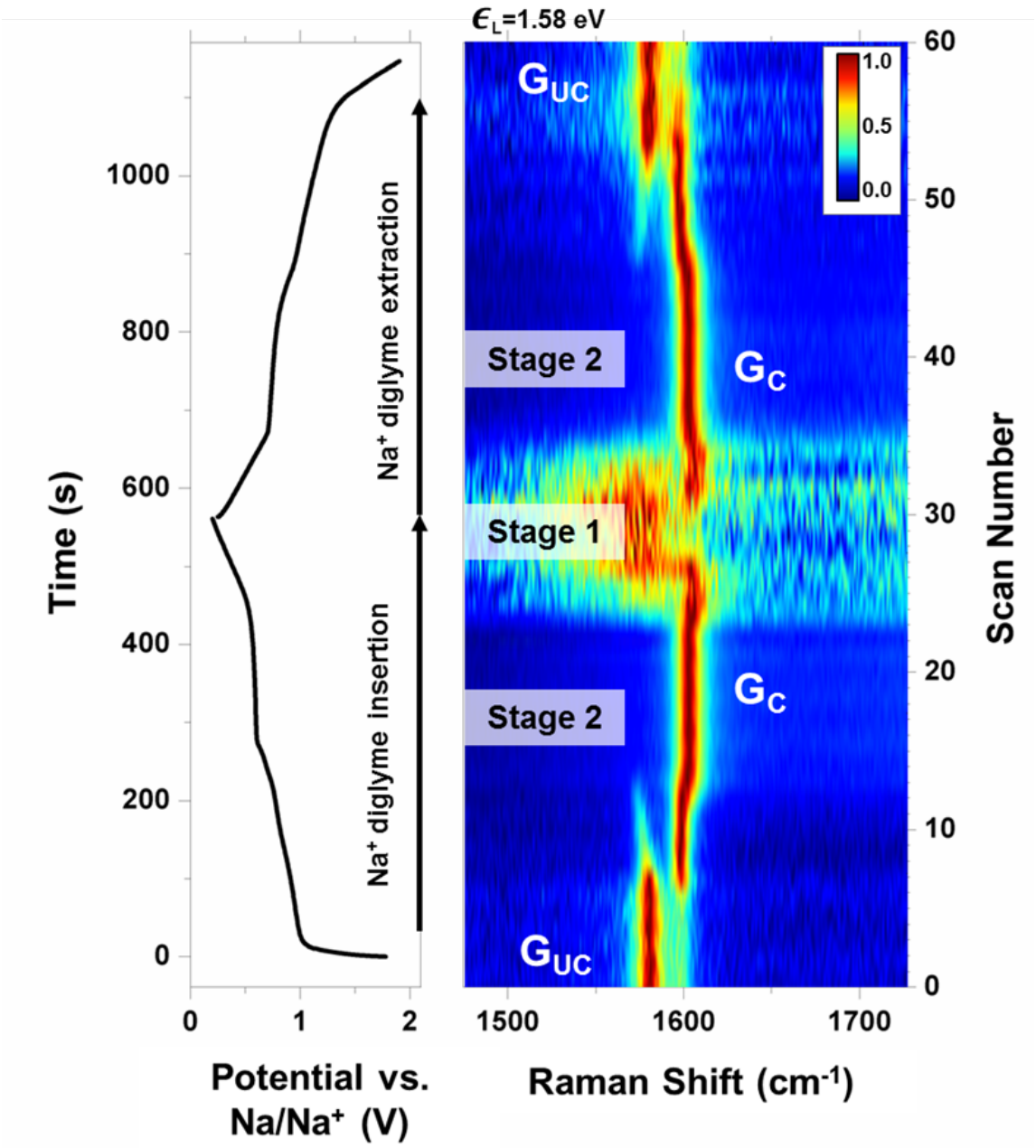

Figure 17: Raman intensity plot (normalized) showing the intercalation and deintercalation reaction using the 1.58 eV laser.

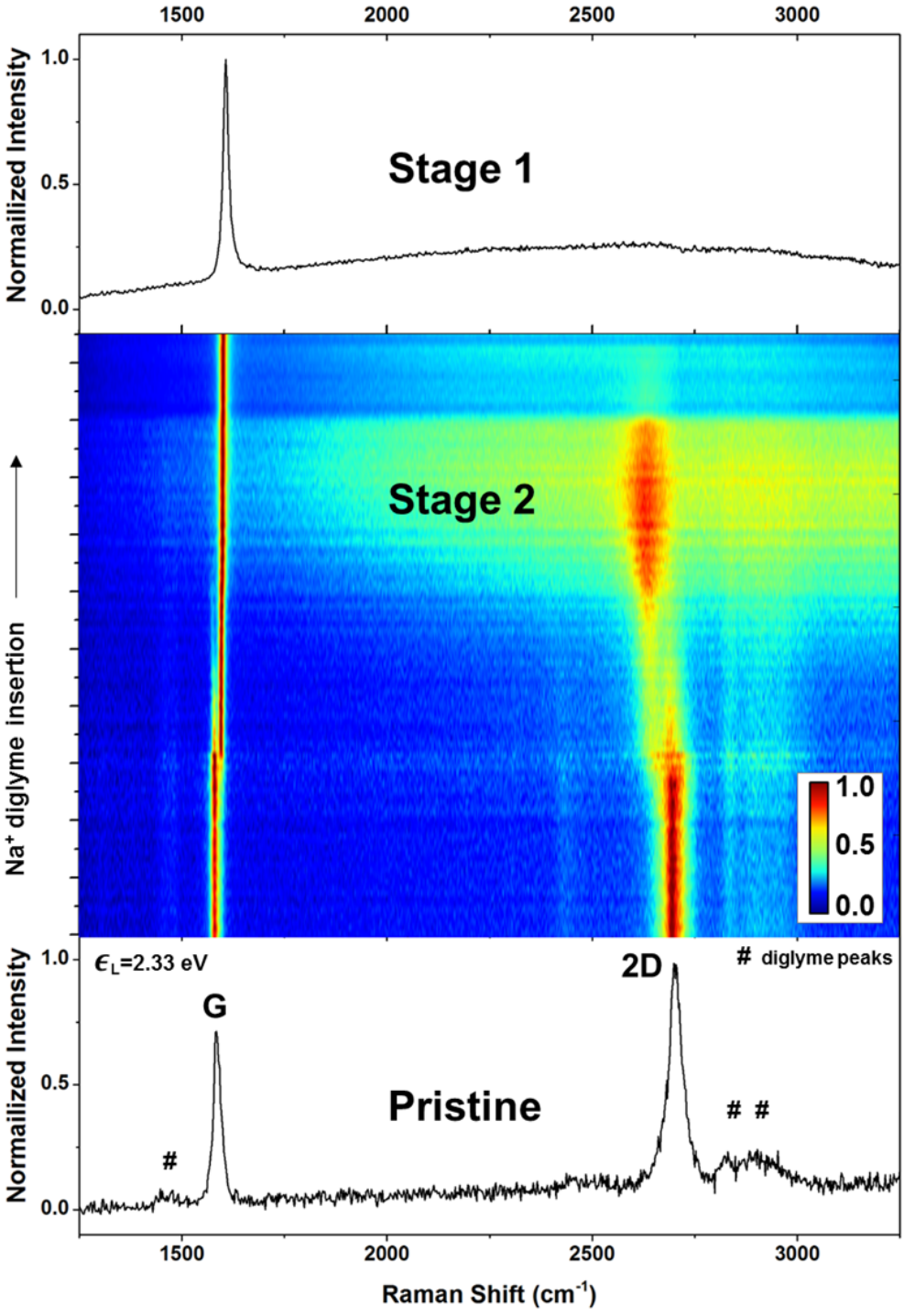

Figure 18: Raman intensity plot (normalized) using the 2.33 eV laser showing both the G peak and 2D peak evolution during the electrochemical intercalation. The 2D peak red-shifts though stage 2 formation (a result of electron doping) and then is suppressed by stage 1 formation.

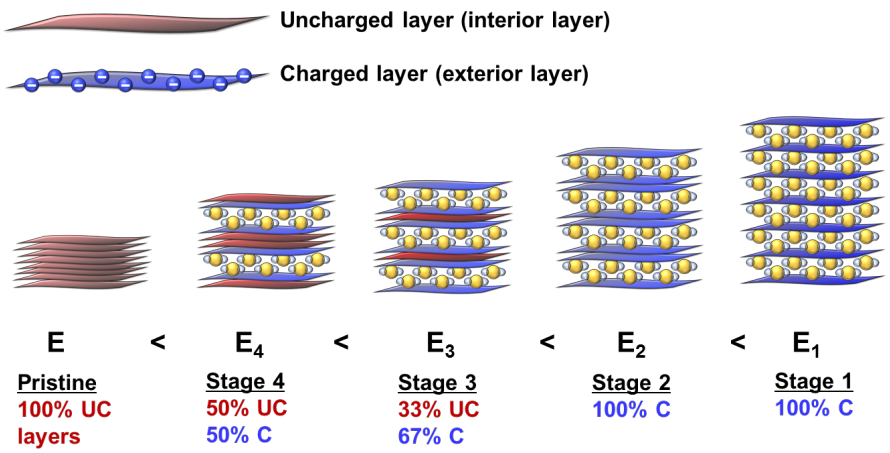

Figure 19: Illustration of the different stages showing the changing ratio between charged and uncharged graphene layers.

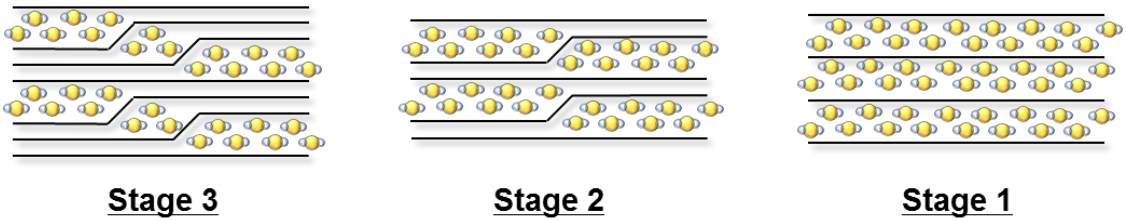

Figure 20: Daumas-Herold model showing the expanding and sliding of ion galleries, which serves to explain the smooth transition between stages.

Lastly, it is worthwhile to discuss the method used for correlating the Raman data to the compound stage number. While it was straightforward to identify the time at which the stage 2 compound was reached from the Raman data (because it coincides with the loss of the G_{UC} peak), determining the earlier stages proved to be more difficult. The following equation has been used in previous Raman studies of GICs to determine the stage number:[47, 48]

$$\frac{I_{UC}(t)}{I_C(t)} = \frac{\sigma_{UC}}{\sigma_C}\frac{n(t)-2}{2} \qquad \text{(Eq. 2)}$$

where I is the peak intensity, σ is the cross section for Raman scattering and n is the stage number. In order to use this equation, the relative cross section for Raman scattering for the two peaks must be known or determined. However, we cannot assume the relative cross sections for Raman scattering to remain constant in our case because we have observed significant changes in the G_C peak intensity during the staging process.

In an attempt to find another method to relate the Raman data to the stage number, we decided to disregard the G_C data and concentrate on the G_{UC} data, assuming that the G_{UC} cross section for Raman scattering remained relatively constant. Examining the peak area of the G_{UC} peak (rather than the peak intensity because we have observed that the FWHM decreases during this period of interest) as shown in Figure 21, we see that G_{UC} peak area remained constant until the emergence of the G_{UC} peak. Afterward, it appears to drop in a step-wise fashion. Since we know that the initial peak area corresponds to 100% of the graphene layers being in an uncharged state, we matched the later peak areas to a percent of the remaining uncharged graphene layers. The first prominent step in the G_{UC} peak area plot (at ~ 410 s) has a value equal to ~50% of the initial peak area, which indicates a stage 4 compound with half of the initial uncharged layers now charged. Then, the second step in the G_{UC} peak area plot (at ~ 520 s) has a value equal to ~33% of the initial peak area, which indicates a stage 3 compound. In this manner, we were able to establish the relationship between the changing G peak area with respect to time and the changing stage number as follows:

$$\frac{A_{UC}(t)}{A_{UC}(t_0)} = 1 - \frac{2}{n(t)} \quad \text{(Eq. 3)}$$

where A is the peak area and n is the stage number. By identifying the stages in this way, we were then able to correlate the stages with the electrochemical data and the 1.58 eV data set as shown in Figure 13.

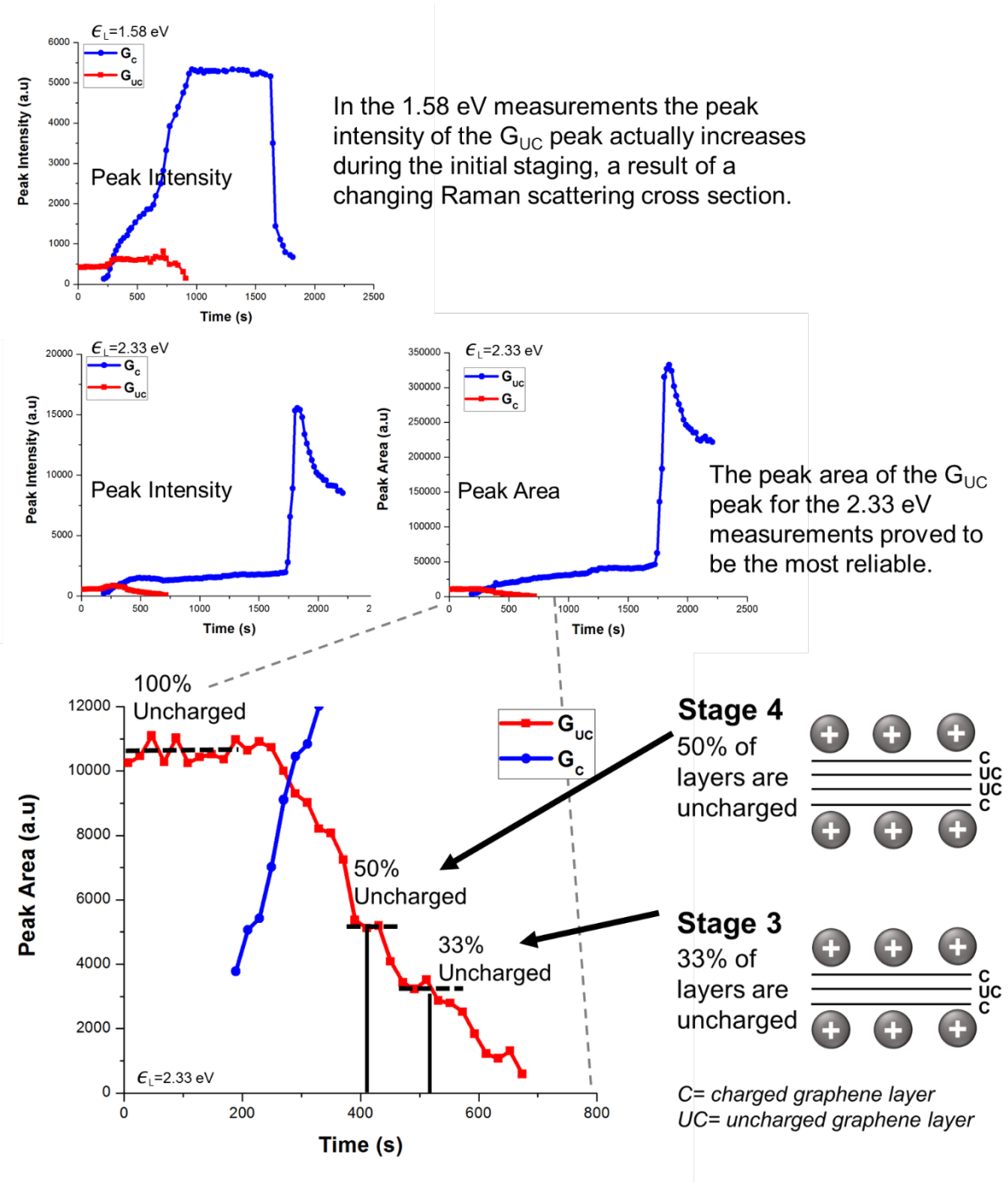

Figure 21: Determining the stage number by examining the changing G_{UC} peak area during the initial staging reaction.

2.5 Conclusion

In this chapter, I explored the fast and reversible cointercalation of Na ions and diglyme molecules into few-layer graphene. Electrochemical testing showed remarkably high rate capability, moderate specific capacity, and exceptional cycling. Conducting in-situ Raman spectroscopy, I resolved the sequential stage formation and determed the Fermi energy of the stage 1 and stage 2 intercalation compounds as 1.2 and 0.8 eV, respectively. These results are promising for the development of high-rate Na-ion batteries, as well a variety of other applications including: other alternative-ion batteries, electrochemical actuators, electrochemical sensors, and electrochemical energy harvesters. In addition, I hope that the extensive Raman characterization will be of interest to battery scientists and material scientists alike.

Chapter 3: Utilizing a Nucleation Layer to Enable an "Anode-Free" Na Battery

3.1 Introduction

In this chapter, I demonstrate a new approach that allows us to overcome the capacity limitations faced by Na-ion anodes by abandoning the anode host material and instead plating Na metal in-situ on an Al current collector equipped with a nucleation layer. In this design, the nucleation layer functions to facilitate the stable electroplating of Na metal. Testing over 1000 plating-stripping cycles shows an average plating-stripping Coulombic efficiency of 99.8% and a low average hysteresis of 14 mV. Imaging of the plated Na reveals island growth, with the islands coalescing to form a smooth Na film. Building on these promising results, I assemble and test the first anode-free Na cell using a pre-sodiated pyrite cathode to provide a specific energy of ~400 Wh/kg with respect to the mass of the cathode and nucleation layer. These results show that Na cells, relying on earth-abundant raw materials such as C, Al, and Na, can be developed with specific energies competitive with current Li-ion cells.

3.2 Background

The growing interest in Na-ion batteries suitable for commercialization has spurred a recent surge in research activity focused on developing electrodes capable of hosting Na ions. However, the larger ionic radius and less negative standard reduction potential (in comparison to Li ions) have limited the specific energy of emerging Na-ion battery technology, with recent state-of-the-art full cells demonstrating only ~200 Wh/kg with respect to active mass of the anode and cathode.[26, 54-56]On this front, the anode side has proven to be the most challenging, as graphite, the standard Li-ion anode, cannot intercalate sufficient Na ions. While alternative anode materials including disordered carbons[57-61] and alloying metals[62, 63] such as Sn ,Sb or Pb, have been extensively researched with notable progress

made, a Na-ion anode that can deliver high capacity and operate at practical currents without sacrificing cycling performance or Coulombic efficiency is yet to be realized.

The continued research effort in this direction begs the question: Is an anode host material truly needed? Transitioning to "host-less" Na metal, in theory, is highly favorable in terms of specific energy as it offers a capacity of 1166 mAh/g (more than double the charged state of the Sn anode: $Na_{15}Sn_4$), as well as the highest electrochemical potential achievable for a Na anode. Furthermore, the density of Na metal (0.97 g/cm^3) also serves to maximize volumetric capacity and achieve high areal loading, eliminating the common tradeoff between gravimetric and volumetric performance. Finally, since the plating/stripping reactions takes place on the surface, there are no solid-state diffusion limitations, and as a result, high-rate capabilities may be achievable without relying on high-surface-area electrodes.

Despite these clear advantages of a Na metal battery, research on room-temperature Na metal electrodes is emergent and currently remains sparse. In 2015, it was shown that Na metal is less stable with carbonate electrolytes than Li metal, due to the organic SEI formed.[64] More recently, there have been initial reports on controlling this SEI layer, either through the use of alternative electrolytes, notably $NaPF_6$ in gylme[65] or highly concentrated NaFSI in gylme[66], to form more stable inorganic SEI layers, or by directly depositing an artificial inorganic SEI layer on Na metal electrodes.[67] However, there has been no research addressing the accompanying issues associated with: (1) the interface between the Na metal and the current collector, (2) the uneven deposition of Na on the current collector, or (3) the large volumetric expansion during deposition, which, in addition to engineering the SEI, have all been identified as critical in recent research on current collectors for Li metal batteries[68-78] and are essential for developing an anode-free Na metal battery.

To maximize specific energy without sacrificing manufacturability, I propose the use of an anode-free design, where the cell is assembled in a discharged state with all the Na contained in the

cathode. While a similar approach was originally demonstrated for thin-film Li batteries using a LiPON electrolyte,[79] the sole effort to adapt this concept for high specific energy Li cells proved challenging due to the limited Coulombic efficiency of Li plating and stripping, and the resulting rapid loss of capacity.[63] In contrast, the high Coulombic efficiency of Na plating and stripping in glyme-based electrolytes makes this a promising approach for developing a Na metal battery.

3.3 Methods

3.3.1 Electrochemical measurements

Carbon films were assembled on Al foil using a mixture of conductive carbon black (TIMCAL Super C45) and Na carboxymethyl cellulose (CMC) with a ratio of 8:2, respectively. Triton X-100 0.35 wt% in deionized water was used at the solvent, avoiding N-methylpyrrolidone (NMP) processing for battery electrodes.[80] Slurries were then spread onto Al foil to obtain carbon films with ~400 μg/cm^2. FeS_2 electrodes were processed similarly using a ratio of 8:1:1 for FeS_2 (325 mesh): carbon black : CMC. FeS_2 electrodes were tested with active mass loading of ~5mg/cm^2.

Electrochemical testing was performed at room temperature in CR2032 coin cells using Celgard 2325 separators. Half-cell testing was performed using ~20 mg of flattened Na metal (Strem Chemicals, 99.95%) as the reference and counter electrode. An electrolyte of 1M $NaPF_6$ in diethylene glycol dimethyl ether (diglyme) (99.5%, Sigma-Aldrich) was used as the electrolyte due to its stability against Na metal and tendency to form stable SEI layers for Na-based chemistries.[40, 65] The $NaPF_6$ salt, acquired from Strem Chemicals with a purity of 99%, was dried at 100 C for 24 hours in Ar before electrolyte preparation.

Prior to plating/stripping testing, all devices were initially galvanostatically cycled 10 times at 0.4 mA/cm^2 from 0.01 to 1.0 V vs. Na/Na$^+$ to remove any surface contamination. Plating/stripping

testing was performed using a stripping cutoff voltage of 100 mV vs. Na/Na^+. Coulombic efficiencies were calculated as the capacity ratio of the Na removed / Na deposited. The voltage hysteresis for each cycle was calculated as the difference between the average voltage measured for corresponding plating and stripping steps. We note that Coulombic efficiency values exceeding 100% for individual cycles may be attributed to the stripping of Na metal that was left behind after previous cycles.

Electrochemical impedance spectroscopy (EIS) was performed on 0.25 mAh/cm^2 of plated Na (0.5 mA/cm^2 for 30 minutes) after the 1^{st}, 2^{nd}, 3^{rd}, 4^{th}, 5^{th} and 10^{th} cycles in half cell configurations with a Na metal reference/counter electrode. EIS was performed using a Metrohm Autolab multichannel electrochemical workstation.

Prior to assembling anode-free cells, FeS_2 electrodes were pre-sodiated in shorted cells with Na metal, a Celgard 2325 separator, and 1M $NaPF_6$ diglyme electrolyte for 24h. The pre-sodiated FeS_2 electrodes were then dried and paired with a carbon/Al negative electrode using a Celgard 2325 separator and 1M $NaPF_6$ diglyme electrolyte and assembled into CR2032 coin cells. After cell assembly, full cells were galvanostatically charged to 3.0 V prior to cycling.

Specific energy calculations were based on the weight of the carbon black on the negative side and the pre-sodiated FeS_2 on the positive side, assuming a stoichiometry of $Na_{1.5}FeS_2$, which would correspond to a FeS_2 specific capacity of ~335 mAh/g.

3.3.2 Na metal imaging

In order to image the plated Na metal, plating was performed in a split-flat cell in an Ar glovebox connected to a single-channel Metrohm Autolab. After plating, electrodes were removed from the glovebox, sealed between two glass slides using a greased O-ring secured with binder clips. To perform the SEM imaging, a “pop-top” transfer cell (shown in Figure 22) was made in the lab utilizing a

taught rubber membrane positioned underneath a needle, so that the membrane bursts when placed under vacuum in the SEM loading chamber to expose the sample to the electron beam in a similar fashion to the cell reported by R. Guame and L. Joubert.[81] A Zeiss MERLIN with GEMINI II SEM was used for imaging.

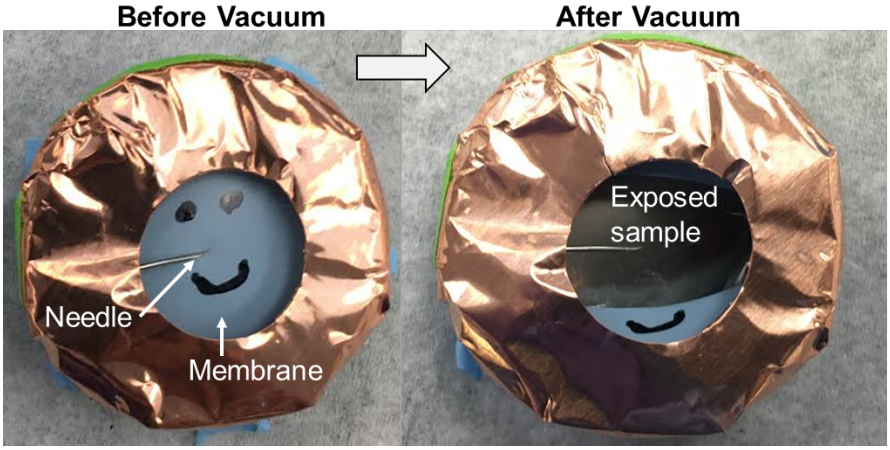

Figure 22: Images of "pop-top" transfer cell used for imaging air-sensitive Na metal samples

3.4 Results and discussion

To evaluate the role of the carbon nucleation layer on the Na plating process, we performed galvanostatic plating at low currents (to minimize diffusion limitations) for both bare Al and carbon/Al substrates. Al was selected instead of Cu because it offers significant cost (~3X cheaper) and weight (~3X lighter) benefits—a key advantage made available by transitioning to Na-based chemistries. Figure 23a shows the sodiation of the carbon/Al current collector, where the sloping potential curve above 0V vs. Na/Na^+ corresponds to the storage of Na ions in disordered carbon, and the steady voltage reached below 0V corresponds to the plating of Na metal. While this figure highlights the sodiation and initial plating that occurs, it is important to note that the capacity provided by the sodiation of the carbon layer, 0.05 mAh/cm^2 (or ~120 mAh/g), is negligible in comparison to the plating capacities, up to 12

mAh/cm^2, we demonstrate in this work. Subsequent plating and stripping testing was performed below 100 mV, so the carbon nucleation layer remained mostly sodiated throughout these tests. Accordingly, we refer to the carbon/Al electrodes as current collectors for anode-free cells as the meaningful capacity is achieved through the in situ plating of the Na metal.

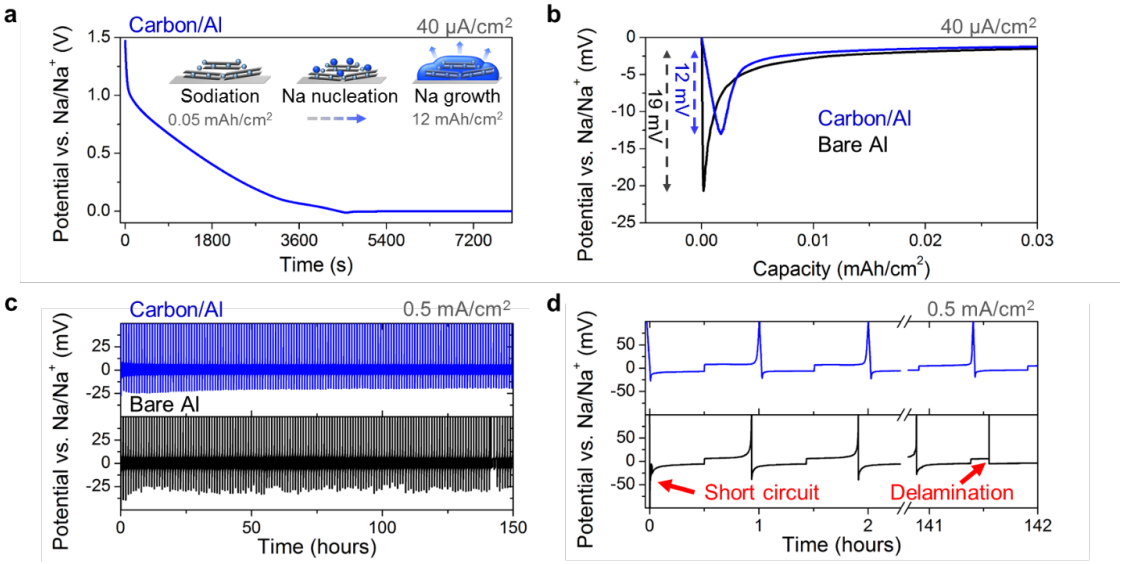

Figure 23: (a) Galvanostatic sodiation and then plating for carbon/Al current collector at 40 μA/cm^2 with carbon loading of 400 μg/cm^2. (b) Comparison of the Na nucleation overpotential for bare Al and carbon/Al current collectors at 40 μA/cm^2. (c) Cycling of bare Al and carbon/Al current collectors at 0.5 mA/cm^2 with 30 minute plating times with (d) enlarged voltage profiles. Reprinted with permission from A. P. Cohn, N. Muralidharan, R. Carter, K. Share and C. L. Pint, Nano Lett., 2017, 17, 1296-1301. Copyright 2016 American Chemistry Society.

Comparing the plating process for a sodiated carbon and a bare Al current collector (Figure 23b), we observe that nucleation overpotential (difference between the bottom of the trough where nucleation occurs and the steady-state plating potential) is reduced from 19 mV to 12 mV by the carbon layer. Reducing this nucleation barrier is critical for facilitating a smoother deposition, minimizing parasitic reactions, and allowing for high-rate performance. The improved performance observed can be attributed to the increased surface area provided by the carbon (~ 180X increase in surface area for a 400 μg/cm^2 carbon layer),[71, 73, 82] the presence of highly-reactive sp^3 carbon sites and oxygen-containing functional groups, and the initial storage of Na ions in the carbon. These observations provide the first

examination of the importance of substrate on the nucleation of Na metal and compliment recent work performed by K. Yan et al. on the effect of substrate on the nucleation of Li metal.[75] Going forward, this work motivates the engineering of carbons nanomaterials for facilitating Na nucleation, bridging the extensive literature aimed at designing carbon materials for Na ion storage forward to higher specific energy Na metal batteries.

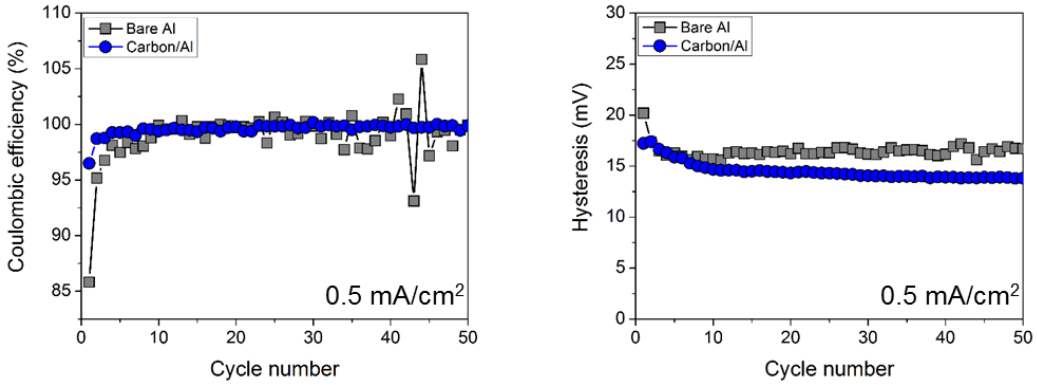

Figure 24: Comparing initial cycling performance for bare Al electrodes and carbon/Al electrodes. We observe higher initial Coulombic efficiency for the carbon/Al electrodes followed by more stable performance. Testing was performed at 0.5 mA/cm^2 for 30 min plating times.

Figure 23c shows 150 hours of plating/stripping cycles performed at an increased rate of 0.5 mA/cm^2. Examining the initial cycles (shown in Figure 23d), we see that during the first plating process, the bare Al electrode exhibits signs of shorting which we attribute to the uneven plating that occurs due to the higher nucleation overpotential. In contrast, the carbon/Al electrodes demonstrate more stable plating and stripping with higher Coulombic efficiency. While we also see sporadic failure in the Al electrodes at later times, as shown in the 141st cycle where a stripping process is cut short due to delamination of the Na metal from the current collector, such occurrences did not take place in the carbon/Al electrodes owing to the improved mechanical stability achieved by utilizing a carbon nucleation layer providing a 3-dimensional interface. A comparison of the Coulombic efficiency and voltage hysteresis for both electrodes is shown in Figure 24.

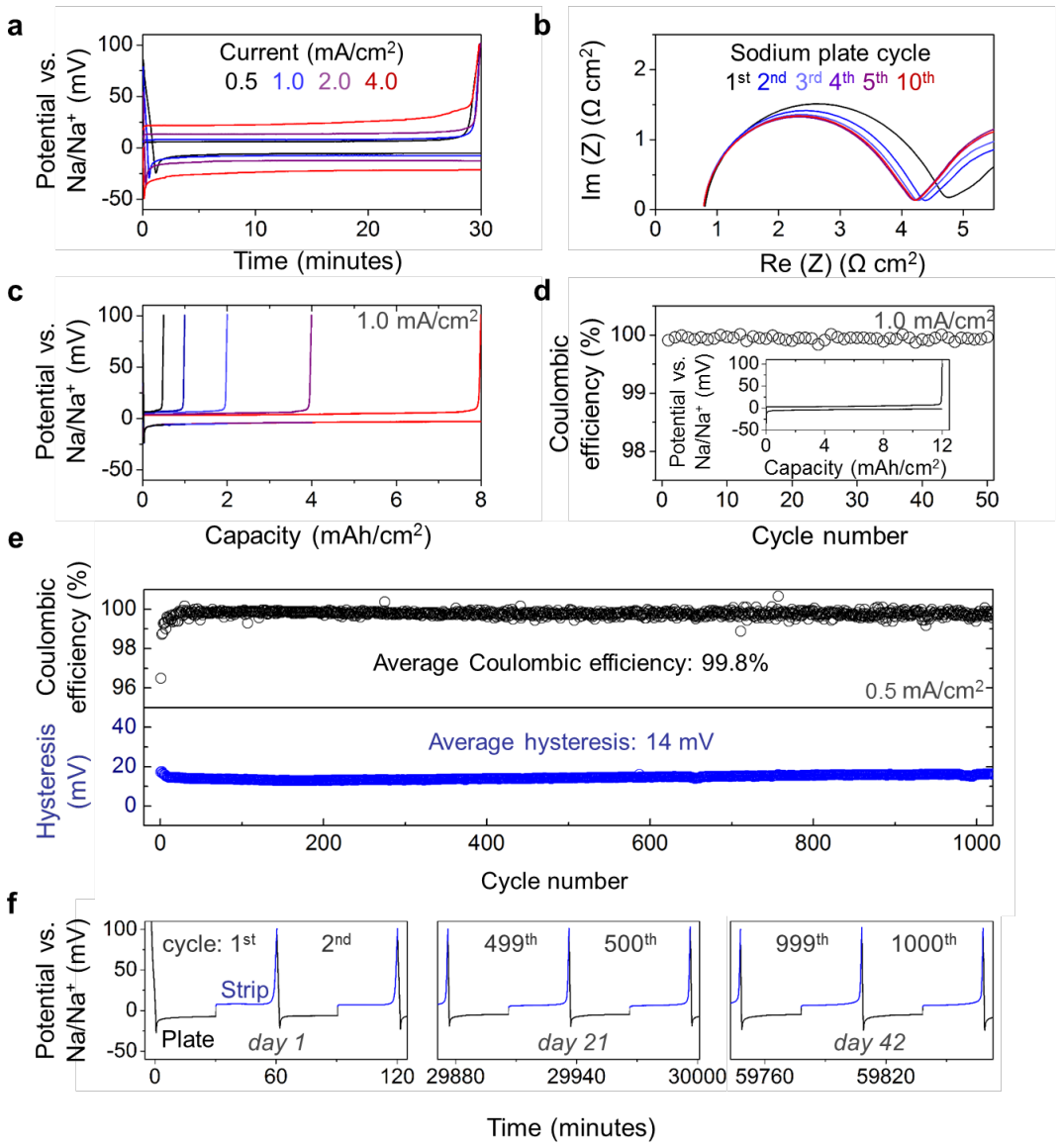

Figure 25: (a) Galvanostatic plating/stripping of Na on carbon/Al current collectors performed over a range of currents for 30 minute plating times. (b) Nyquist curves performed after initial plating cycles with 0.25 mAh/cm^2 loading. (c) Galvanostatic plating/stripping of Na on carbon/Al current collectors performed over a range of times (or loadings) at 1.0 mA/cm^2. (d) 50 cycles performed at 1 mA/cm2 with 12 mAh/cm2 loading of Na with the in set showing a corresponding potential profile (e) Coulombic efficiency and voltage hysteresis from over 1,000 plating/stripping cycles performed at 0.5 mA/cm^2 with 0.25 mAh/cm^2 loading. (f) Corresponding potential profiles of the 1st, 2nd, 499th, 500th, 999th and 1000th plating/stripping cycles. Figure 26: (a) Galvanostatic sodiation and then plating for carbon/Al current collector at 40 μA/cm^2 with carbon loading of 400 μg/cm^2. (b) Comparison of the Na nucleation overpotential for bare Al and carbon/Al current collectors at 40 μA/cm^2. (c) Cycling of bare Al and carbon/Al current collectors at 0.5 mA/cm^2 with 30 minute plating times with (d) enlarged voltage profiles. Reprinted with permission from A. P. Cohn, N. Muralidharan, R. Carter, K. Share and C. L. Pint, Nano Lett., 2017, 17, 1296-1301. Copyright 2016 American Chemistry Society.

To further assess the carbon/Al electrodes, we conducted testing over a range of currents from 0.5 mA/cm^2 to 4 mA/cm^2. As shown in Figure 25a, the carbon nucleation layer enables a low voltage hysteresis even at high currents, with a 45 mV hysteresis at 4 mA/cm^2. In contrast, bare Al electrodes were prone to failure at these currents. To assist our understanding of the low hysteresis, electrochemical impedance spectroscopy was performed after initial plating cycles with 0.25 mAh/cm^2 of fresh Na (Figure 25b). We found the charge-transfer resistance, corresponding to the diameter of the semicircle in the Nyquist plot, to be extremely low and stable with cycling. Next, we performed plating/stripping testing at increased loadings of Na (Figure 25c). We found that the electrodes exhibited stable performance at 1 mA/cm^2 for 30 minute plating times (0.5 mAh/cm^2) up to 8 hour plating times (8 mAh/cm^2), with the Coulombic efficiency slightly increasing with loading, from 99.8% to 99.9%, indicating that the minor losses in the system occur during the initial seeding and/or the final stripping processes. To further demonstrate the versatility of this approach for exceptionally high loadings of Na, 50 cycles were performed at 12 mAh/cm^2 with the average Coulombic efficiency exceeding 99.9% (Figure 25d). These results are promising for the development electrodes with high aerial capacities, a focus of researchers who aim to minimize the cost of current collectors and separators.[59, 80, 83]

To test the long-term durability, we ran over 1000 plating-stripping cycles using 30 minute plating times to maximize the initial seeding and final stripping events that appear most problematic (Figure 25e). Nonetheless, we observed a stable hysteresis averaging 14 mV and a stable Coulombic efficiency averaging 99.8%, with no evidence of short circuiting or delaminating. Figure 25f shows the voltage profiles from the 1st, 2nd, 499th, 500th, 999th and 1000th cycles, which all appear nearly identical, emphasizing the stability maintained during cycling.

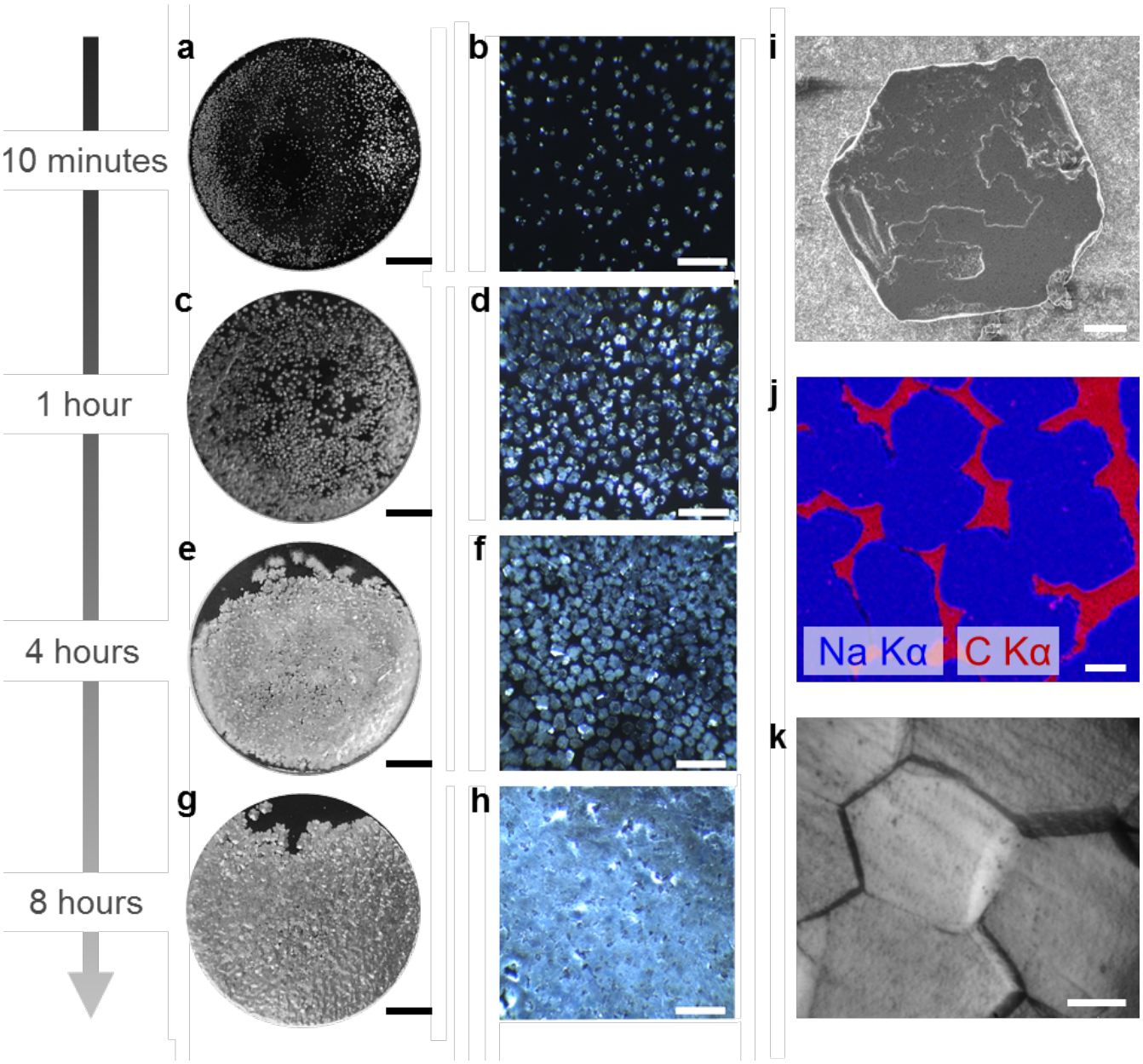

Figure 27: Photographs (SB=2 mm) and micrographs (SB=500 μm) of Na metal on carbon/Al electrodes following plating at 0.5 mA/cm^2 for (a, b) 10 minutes, (c,d) 1 hour, (e, f) 4 hours, and (g,h) 8 hours. (i) SEM image of hexagon-shaped Na metal island (SB=20 μm). (j) EDS map showing coalescing Na metal islands (CB=50 μm). (k) Micrograph of plated Na metal film with 4 mAh/cm^2 loading (SB=20 μm). Figure 28: (a) Galvanostatic sodiation and then plating for carbon/Al current collector at 40 μA/cm^2 with carbon loading of 400 μg/cm^2. (b) Comparison of the Na nucleation overpotential for bare Al and carbon/Al current collectors at 40 μA/cm^2. (c) Cycling of bare Al and carbon/Al current collectors at 0.5 mA/cm^2 with 30 minute plating times with (d) enlarged voltage profiles. Reprinted with permission from A. P. Cohn, N. Muralidharan, R. Carter, K. Share and C. L. Pint, Nano Lett., 2017, 17, 1296-1301. Copyright 2016 American Chemistry Society.

In order to gain insight into the plating process, carbon/Al electrodes were imaged with progressing Na loading. Figure 27 shows electrodes after 10 minutes (a,b), 1 hour (c,d), 4 hours (e,f) and 8 hours (g,h) of plating at 0.5 mA/cm^2. From these images, we see a progression from the seeding of well-spaced islands of Na to the growth and coalescence of these islands to form a smooth, shiny film of Na metal. Interestingly, we found that the islands appear to grow as hexagons, as shown in the scanning electron micrograph (SEM) in Figure 27i, and the hexagonal pattern is maintained as the islands begin to coalesce together (shown in the energy dispersive x-ray spectroscopic map in Figure 27j) and persevered in the formed film, creating the appearance of polycrystallinity with defined grain boundaries (Figure 27k). To the best of our knowledge, this is the first documentation of such a plating process for alkali metals, which is especially interesting as it underlies extremely efficient and stable electrochemical performance. In comparison, the Na film that is deposited on bare Al electrodes appears to exhibit a less defined pattern (Figure 29). Furthermore, examining Na plated at an increased current density of 4 mA/cm^2 (Figure 30), we observed smaller grains, in line with the recent work of A. Pei et al.[84]

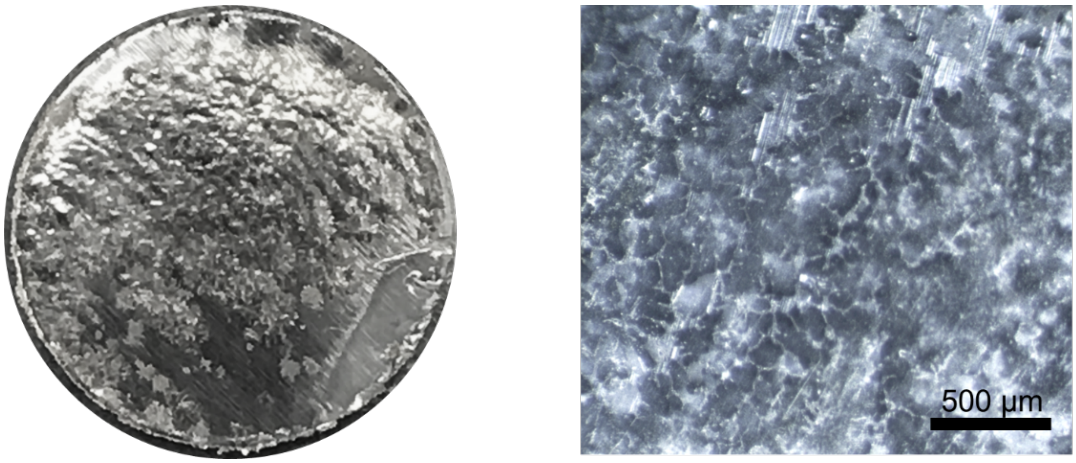

Figure 29: Bare Al electrode (10 mm diameter) with 2 mAh/cm^2 of plated Na metal performed at a rate of 0.5 mA/cm^2 (4 hour plating duration).

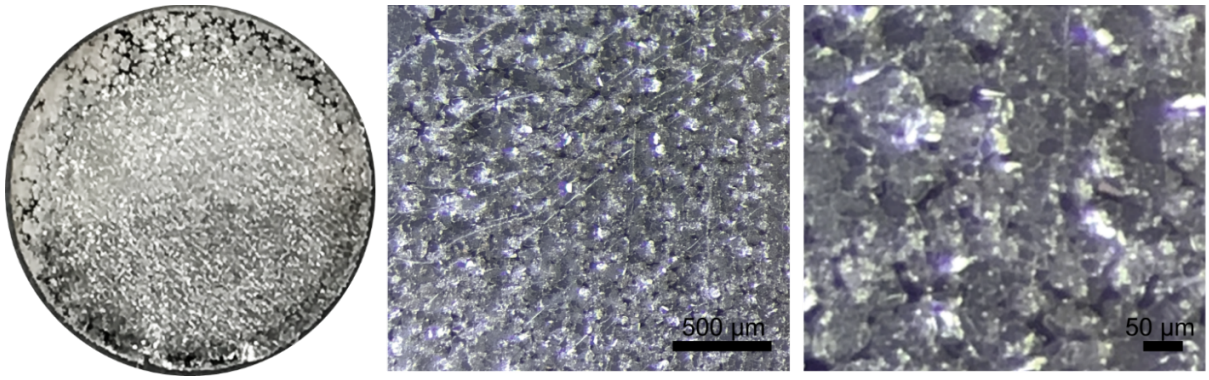

Figure 30: Carbon/Al electrode (10 mm diameter) plated with 2 mAh/cm^2 of plated Na metal performed at a rate of 4 mA/cm^2 (30 minute plating duration).

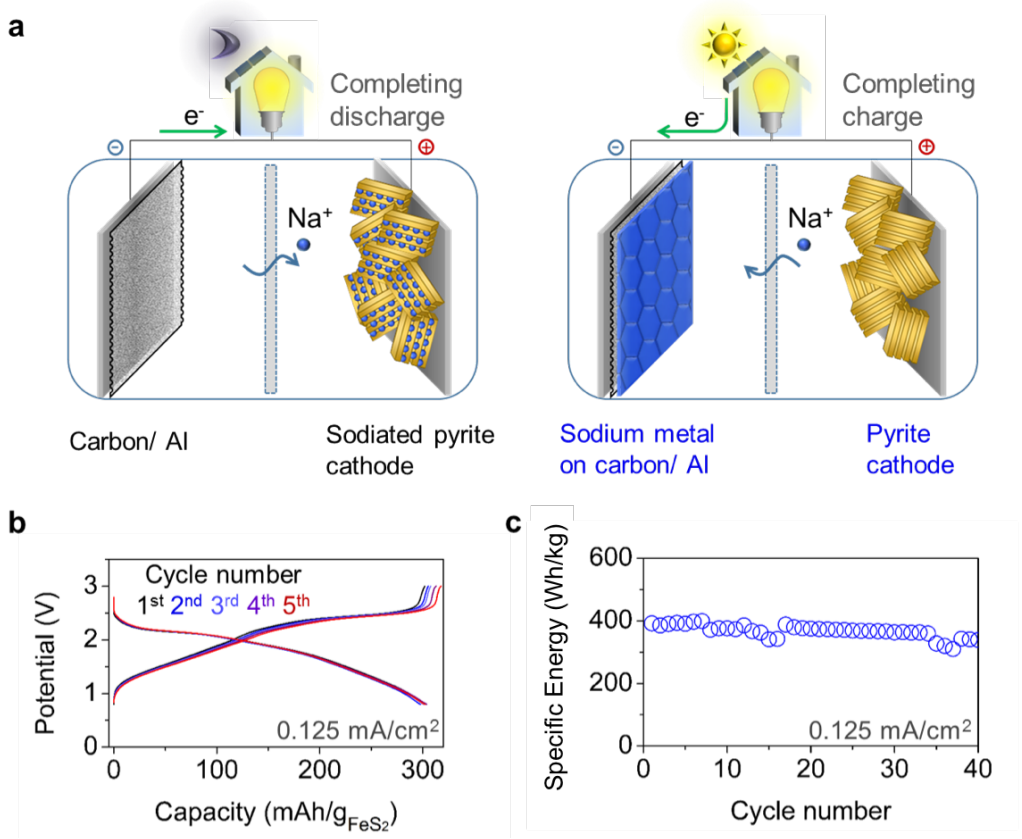

Figure 31: Illustration of the charged and discharged states of the anode-free Na battery utilizing the carbon/Al electrode. (b) Galvanostatic potential profiles of the full cell showing the first 5 cycles at 0.125 mA/cm^2 from 0.8 to 3.0 V with (c) the delivered specific energy of the first 40 cycles with respect to the combined active mass of both electrodes. Figure 32: (a) Galvanostatic sodiation and then plating for carbon/Al current collector at 40 µA/cm^2 with carbon loading of 400 µg/cm^2. (b) Comparison of the Na nucleation overpotential for bare Al and carbon/Al current collectors at 40 µA/cm^2. (c) Cycling of bare Al and carbon/Al current collectors at 0.5 mA/cm^2 with 30 minute plating times with (d) enlarged voltage profiles. Reprinted with permission from A. P. Cohn, N. Muralidharan, R. Carter, K. Share and C. L. Pint, Nano Lett., 2017, 17, 1296-1301. Copyright 2016 American Chemistry Society.

Finally, to demonstrate the feasibility of using this plating approach for an anode-free cell configuration, we developed a full-cell anode-free Na battery. To accomplish this, we employed pyrite (FeS_2) for the cathode as it is a cheap, abundant material that has recently been shown to be an excellent candidate for Na-ion batteries with diglyme-based electrolytes.[25] However, since it natively does not contain Na, we first pre-sodiated the pyrite cathode prior to cell assembly, in a fashion similar to previous reports.[85] Full cells were constructed using pre-sodiated pyrite paired with carbon/Al current collectors, corresponding to a discharged device state, as illustrated in Figure 31. During the initial charge, the Na ions are removed from pyrite during the oxidation reaction and reduced on the carbon/Al current collector to form Na metal *in situ*. In this manner, we have developed a Na metal battery that does not contain Na metal on assembly. To prove that Na metal was indeed forming during the charging process, we dissembled a fully charged full cell and show the plated Na metal on the carbon/Al electrode in Figure 33. Initial voltage profiles exhibited during galvanostatic testing are shown with respect to the mass of the pyrite (assuming a $Na_{1.5}FeS_2$ stoichiometry) in Figure 4b for the full cell following the initial charging process. Figure 31c shows the stability of the delivered specific energy over 40 cycles. The ~400 Wh/kg specific energy, calculated based on the mass of the pre-sodiated pyrite (assuming a $Na_{1.5}FeS_2$ stoichiometry or a FeS_2 capacity of 335 mAh/g) and the carbon nucleation layer, exceeds all previous reports for Na-ion batteries and, assuming a 50% packaging penalty, exceeds current Li-ion technology. Going forward, better optimization of the cathode is expected to allow for increased cycling stability and improved rate capability.

Figure 33: Na metal (1 mAh) plated from pre-sodiated FeS_2 on carbon/Al electrode during the first charging of the device. The image shows that, as expected, Na metal is formed during charging for the anode-free full cells. To open this cell without shorting the device, testing was performed in a split-flat cell in the glovebox for easy disassembly.

3.5 Conclusion

In this chapter, I demonstrated that a carbon nucleation layer can be used to enable highly efficient and stable Na plating and stripping. This finding provided the foundation to develop a new Na battery: the "anode-free" Na battery. I have shown here that this strategy can be used to achieve specific energies competitive with current Li-ion cells while relying on earth-abundant materials. These system is especially promising for cost-sensitive large applications, such as stationary storage and electric vehicles.

Chapter 4: Rethinking Na-Ion Anodes as Nucleation Layers for Stable Na Metal Plating

4.1 Introduction

In the previous chapter, I showed that a thin layer of carbon (the nucleation layer) allowed the use an aluminum negative current collector, rather than denser and more costly copper, while achieving highly reversible Na plating and stripping. However, many key concepts of this system remain unexplored, such as the effect of the material composition of the nucleation layer on Na nucleation and the resulting cycling performance. In this chapter, I explore the use of different materials, including a range of carbons and Na-alloying metals, that have shown stable Na-ion storage properties as anodes in gylme-based electrolytes with the aim of identifying the best-suited nucleation layer composition to use for anode-free full cells.

Based on the work in the previous chapter, the hypothesis going into this set of experiments was that the lower the energetic barrier to Na metal nucleation, the more stable and reversible the Na plating-stripping performance would be. However, as I show in this chapter, I found the opposite to be the case.

4.2 Methods

4.2.1 Material fabrication and characterization

To synthesize hard carbon, an aqueous sucrose solution (1.5 M) was kept at 190 ^{o}C in an autoclave for 5 hours, dried, and then pyrolyzed at 1100 ^{o}C under an Ar flow for 5 hours. X-ray diffraction was performed using a Rigaku SmartLab XRD. X-ray diffraction patterns comparing the carbon black (TIMCAL Super C45) and synthesized hard carbon are presented in Figure 34.

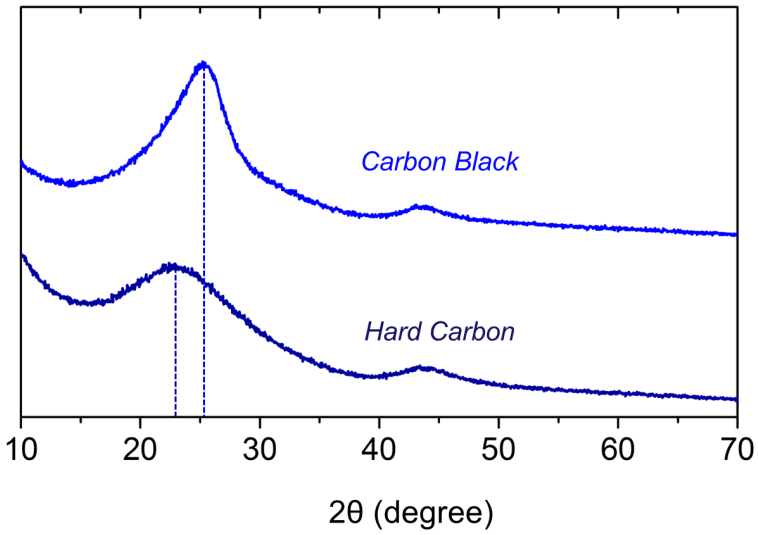

Figure 34: X-ray diffraction patterns for carbon black (TIMCAL Super C45) and synthesized hard carbon

4.2.2 Electrochemical testing

Electrodes were made by mixing active material (70%) with TIMCAL Super C45 carbon black (10%) and CMC binder (20%) using water as the solvent. All slurries were spread onto carbon-coated Al foil (MTI), as shown in Figure 35, and then punched as 1 cm diameter discs and dried in a vacuum oven at 70 ºC prior to device assembly with loadings of of ~1 mg/cm^2. An electrolyte of 1M $NaPF_6$ in diglyme was used for all electrochemical testing. Prior to making electrolyte, $NaPF_6$ salt (Strem, 99%) was dried at 100 ºC overnight in an Ar glovebox and diglyme (99.5%, Sigma-Aldrich) was dried using 4A molecular sieves. Electrolyte was used within a day of preparation. Half cells were assembled using Na metal that was pressed flat onto a stainless steel disc (using a hydraulic crimper (~100 psi) and placing a metal plate and Celgard 2325 separator—to prevent the Na from sticking to the metal plate—on top of the Na metal on stainless steel disc), a Celgard 2325 separator, ~40 µl of electrolyte, and crimped in CR2032 coin cells (~1200 psi). Coin cell assembly and the flattened Na metal is shown in Figure 36.

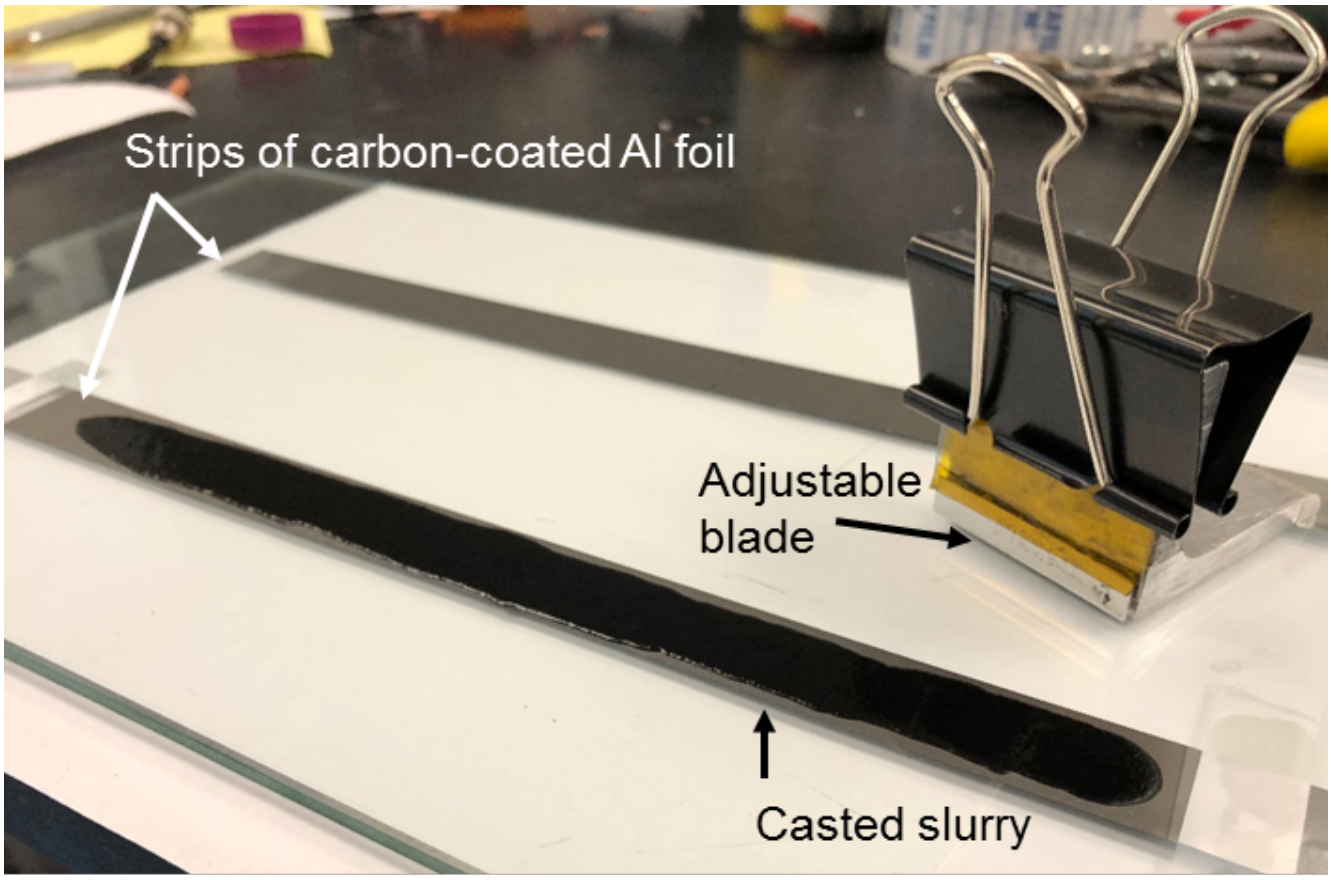

Figure 35: Homemade adjustable film applicator. Blade height was adjusted using a feeler gauge set. Aluminum foil was placed onto a glass plate with isopropyl to keep the foil flat and well adhered.

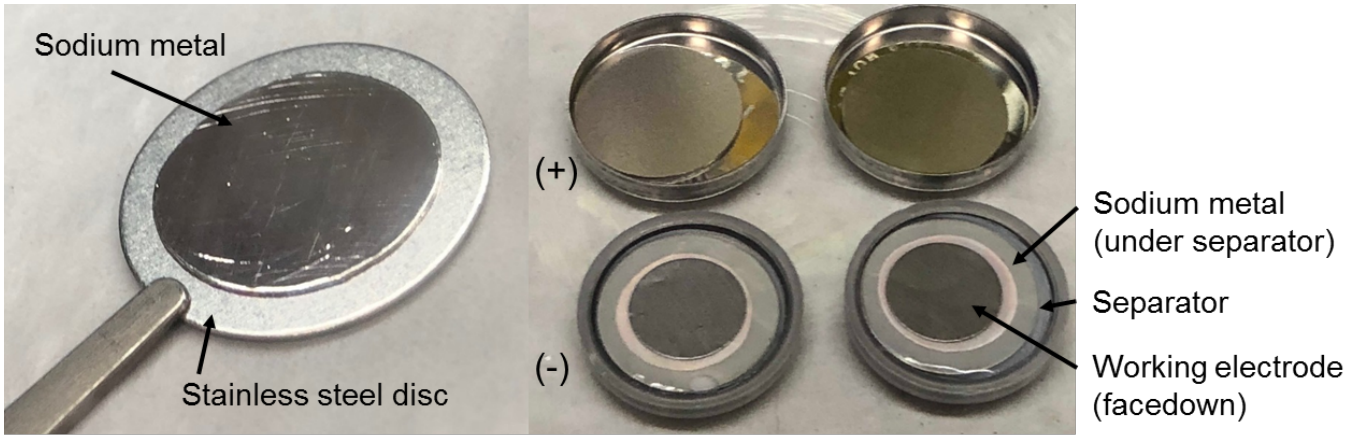

Figure 36: Na metal flattened onto a stainless steel disc (left). Two coin cells prior to crimping (right).

4.2.3 Data analysis

To construct the slippage plots, I wrote a script to import and organize the data using Pandas (a data analysis/data structures toolkit for Python). Each slippage plot consists of ~180,000 data points, with 2 second record intervals over the ~100 hours of cycling.

4.3 Results and discussion

4.3.1 Evaluating anode materials as nucleation layers

To evaluate the performance and nucleation energetics of the different nucleation layer compositions, electrochemical testing was conducted in half cells using Na metal as the counter and reference electrode and an electrolyte of 1M $NaPF_6$ in diethylene glycol dimethyl ether (diglyme). Carbon black and hard carbon were first selected for comparison because they exhibit different Na-ion storage properties despite their similar defective nature. As shown in the insertion-extraction profiles in Figure 37a and b, hard carbon exhibited approximately three times the Na-ion storage capacity of carbon black. The hard carbon plateau at 0.1 V, which accounts for the increased capacity, has controversially been attributed to either the adsorption of Na ions in carbon micropores or the intercalation of Na ions between graphene sheets.[86, 87]

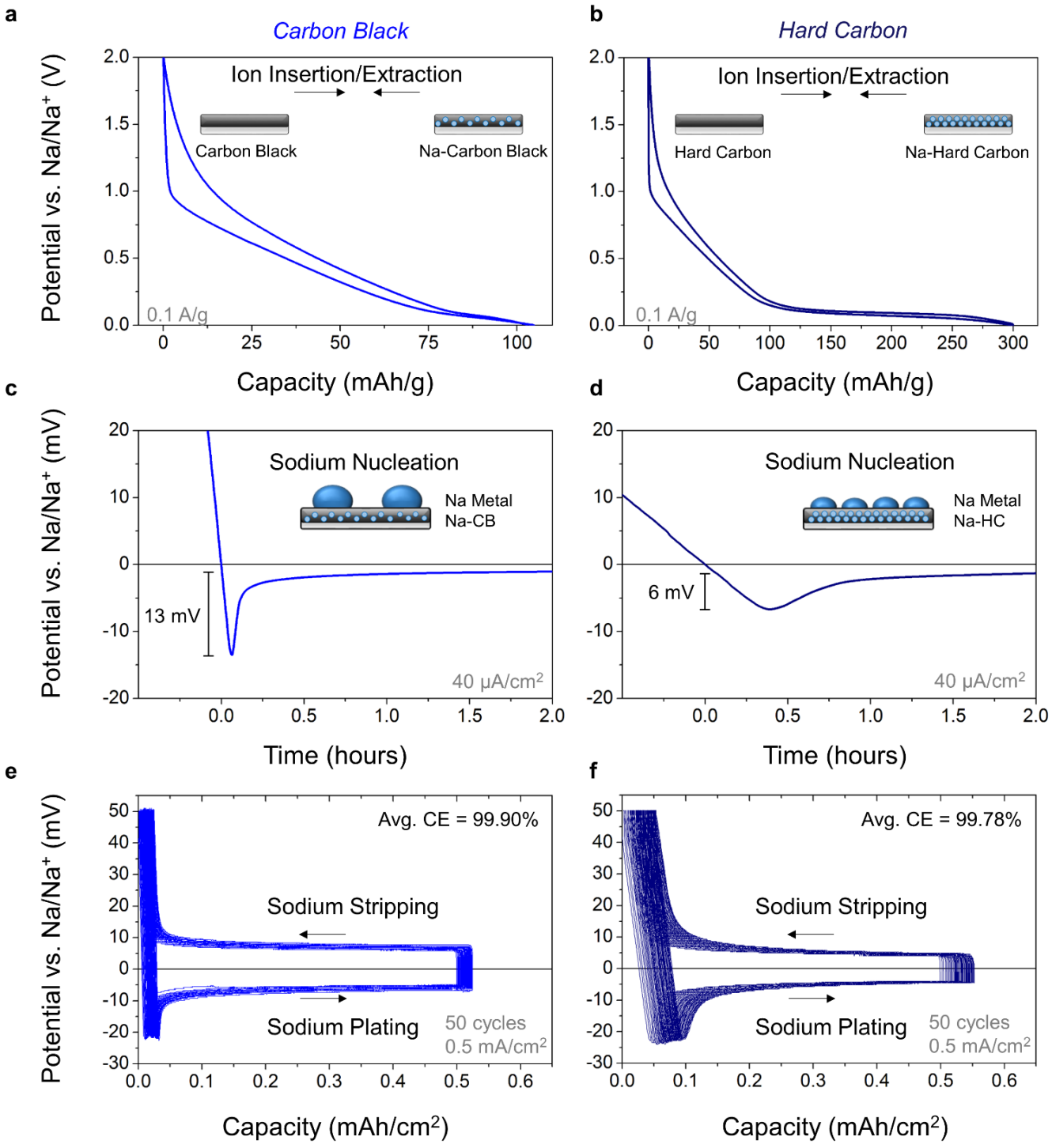

Figure 37: Figure 2. (a,b) Electrochemical voltage profiles for Na ion insertion/extraction at 0.1 A/g for carbon black (left) and hard carbon (right) electrodes. (c,d) Na metal nucleation profiles at 40 μA/cm^2 on sodiated electrodes. (e,f) Slippage profiles for Na metal plating and stripping over 50 cycles at 0.5 mA/cm^2 on sodiated electrodes.

The energy barrier to Na nucleation was measured by plating (allowing the voltage to drop below 0 V vs. Na/Na^+) on fully sodiated electrodes at a low current density of 40 $\mu A/cm^2$ to minimize the effect of mass transfer.[75] We found that the nucleation overpotential (Figure 37c and d) was significantly lower for the hard carbon (6 mV) than the carbon black electrode (13 mV). This difference may be explained in part by the different operating voltages of the Na ion storage in the different carbon materials. The lower operating voltage of the Na ion storage in hard carbon indicates a lower degree of ionicity of the stored Na,[88] resulting in an electrode that is more similar to Na metal. Accordingly, the nucleation overpotential is lower on such an electrode, which is expected to result in smaller and more numerous Na nuclei, as the nuclei critical radius is dependent on the energy barrier.[84]

To assess the Na plating-stripping performance, testing was conducted at an increased current density of 0.5 mA/cm^2, a plating capacity of 0.5 mAh/cm^2, and a stripping cutoff of 50 mV. Figure 37e and f show 50 plating-stripping cycles performed on the carbon black and hard carbon electrodes with the start of each cycle plotted from the capacity endpoint of the previous cycle in order to capture the slippage due to the loss of charge. This form of plot, which has been utilized by Dahn's group to analyze full cells,[89] highlights the total conservation of charge while also showing all the cycle profiles in entirety. Loss of charge, with Coulombic efficiencies deviating from unity, results in a cycle-to-cycle shift to the right. In this manner, the difference in the starting and ending point after 50 cycles corresponds to the cumulative loss of charge. While both electrodes exhibited stable performance, the loss of charge over 50 cycles using the carbon black electrode was approximately half that found when using the hard carbon electrode. Average Coulombic efficiencies were calculated to be 99.90% and 99.78% for the carbon black and hard carbon electrodes, respectively. This difference is expected to be very significant for anode-free cell performance, where the loss of Na is expected to be the limiting factor for cycle life.

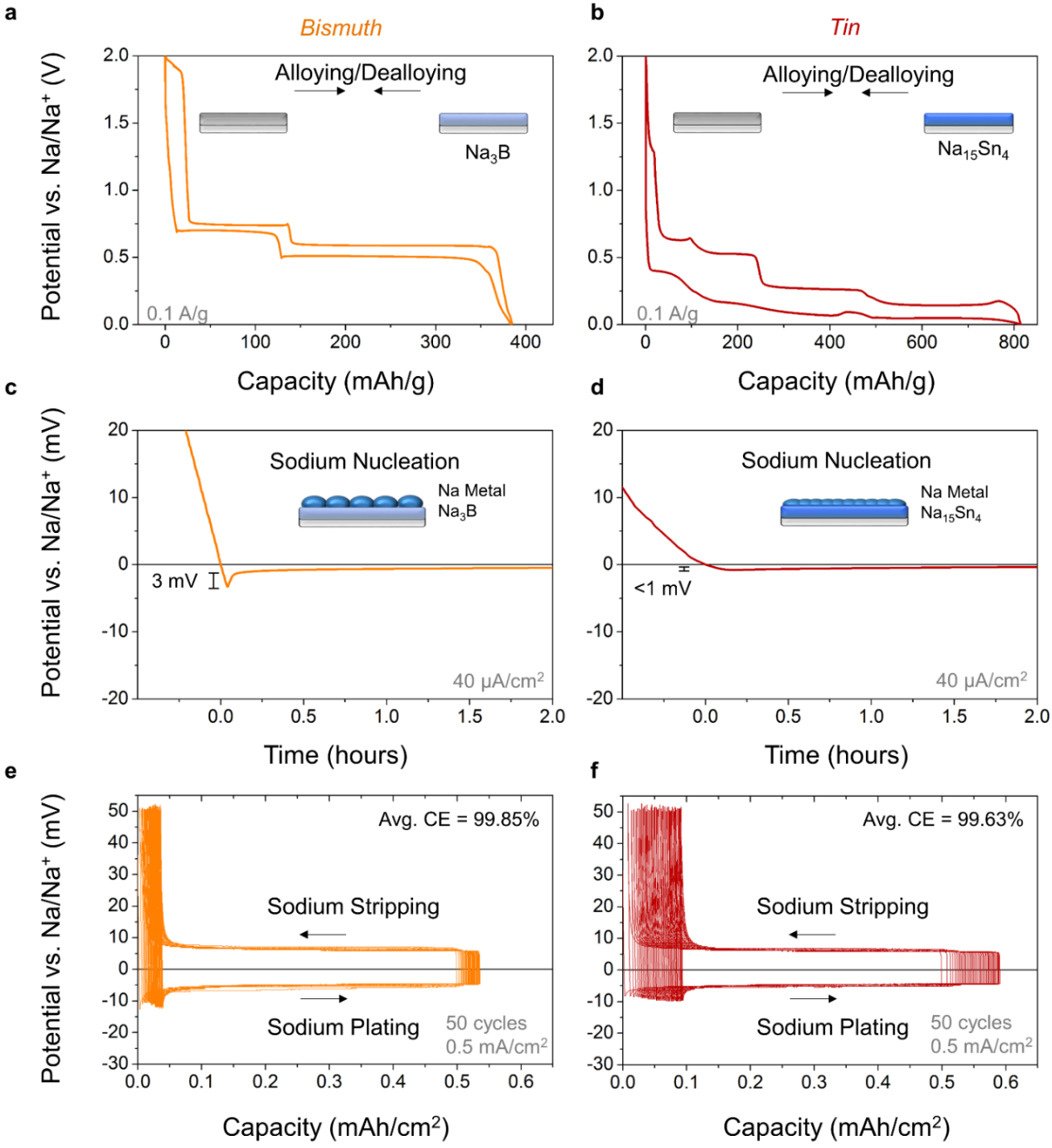

Figure 38: (a,b) Electrochemical voltage profiles for Na ion alloying/dealloying at 0.1 A/g for bismuth (left) and tin (right) electrodes. (c,d) Na metal nucleation profiles at 40 μA/cm^2 on sodiated electrodes. (e,f) Slippage profiles for Na metal plating and stripping over 50 cycles at 0.5 mA/cm^2 on sodiated electrodes.

Next, tin and bismuth were selected for comparison as alloying electrodes because they show different Na alloying behavior and they have both been recently reported to exhibit stable performance as alloying anodes in diglyme-based electrolytes.[26, 27] Electrodes were prepared with microsized particles (325 mesh) in accordance with these previous reports. Figure 38 a and b show the voltage profiles performed at 0.1 A/g between 0 and 2 V vs. Na/Na^+. The bismuth alloying curve displays flat plateaus at 0.7 and 0.5 V, with the lower voltage plateau reaching twice the capacity of the higher voltage plateau. These two distinct plateaus have been identified as the formation of NaBi and Na_3Bi alloys, which is in agreement with the capacity of ~380 mAh/g. In contrast, the tin alloying curve shows more than twice the capacity, approximately forming $Na_{15}Sn_4$, and less distinct plateaus that are closer to the Na/Na^+ potential.

Figure 38c and d show the voltage profiles for the nucleation of Na metal on these alloys. The nucleation overpotentials for the Na-bismuth alloy and the Na-tin alloy are 3 mV and less than 1 mV, respectively. The difference between the two nucleation overpotentials can again be explained in part by the difference in operating voltage of the initial alloying process, with the formation of the Na-tin alloy taking place closer to the potential of Na/Na^+. In addition, the higher Na content of the Na-tin alloy can be interpreted as making the alloy more Na-like.

Where the small barrier to nucleation measured for the Na-bismuth alloy suggests the initial formation of small Na nuclei, the absence of a barrier to nucleation on the Na-tin alloy may indicate layered growth. From the corresponding 50 cycles of plating-stripping shown in Figure 38e and f, it is clear that the Na-bismuth electrode demonstrated less charge loss than the Na-tin electrode. Average Coulombic efficiencies were calculated to be 99.85% and 99.63% for the bismuth and tin alloying electrodes, respectively. Interestingly, the carbon black and the bismuth electrodes, which showed the comparatively lower capacities and higher operating voltages for Na-ion storage, facilitated improved

Coulombic efficiencies for the plating and stripping of Na metal. These findings indicate a correlation between initial plating morphology, which is indirectly measured as the nucleation overpotential, and the resulting Coulombic efficiency. Specifically, we suspect that Na depositions with higher surface-area-to-volume ratios (correlating to lower nucleation overpotentials) are likely to result in more parasitic reactions with the electrolyte than depositions with lower surface-area-to-volume ratios (correlating to higher nucleation overpotentials). However, it is important to point out that we previously showed that plating on materials exhibiting very high nucleation overpotentials, such as bare aluminum, can result in more severe concerns, including: (1) delamination due to poor mechanical connectivity between the Na and the electrode; and (2) problematic dendritic growth due to the high effective current densities produced by non-uniform and poorly-spread Na depositions.[90] In this respect, our use of nucleation layers allows us to overcome these highly problematic events and probe the more subtle differences in Coulombic efficiency that appear to be due to differing nucleation energetics and resulting morphologies. In contrast, recent work examining nitrogen-doped graphene[91] and carbon nanofibers with silver nanoparticles[92] as nucleation layers for Li plating, have been mainly limited to alleviating dendritic growth.

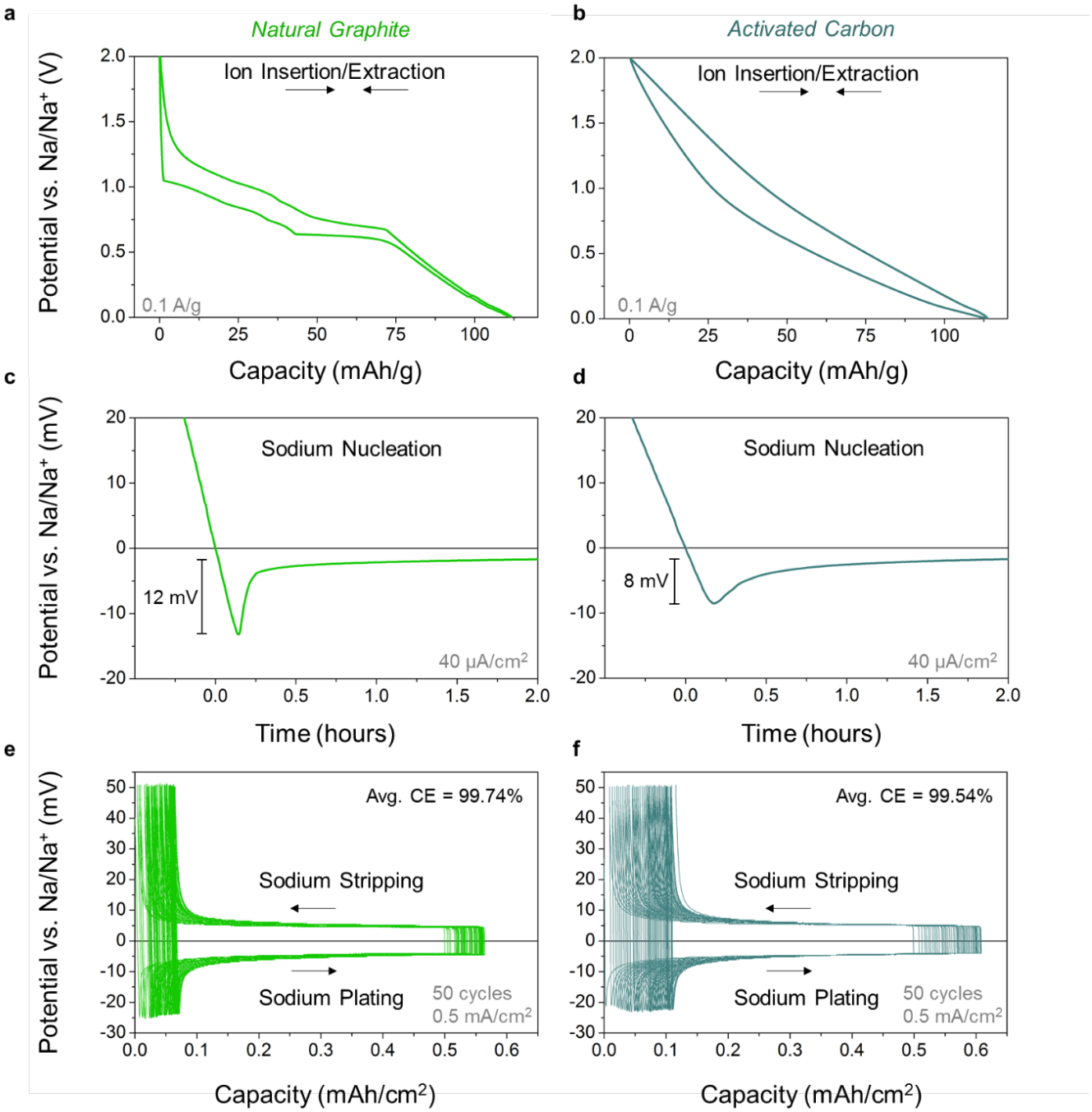

Figure 39: (a,b) Electrochemical voltage profiles for Na ion insertion/extraction at 0.1 A/g for natural graphite (left) and activated carbon (right) electrodes. (c,d) Na metal nucleation profiles at 40 µA/cm^2 on sodiated electrodes. (e,f) Slippage profiles for Na metal plating and stripping over 50 cycles at 0.5 mA/cm^2 on sodiated electrodes.

While all of the tested electrodes exhibited high Coulombic efficiencies and stable performance, carbon black was selected as the nucleation layer for anode-free cells because it demonstrated the highest Coulombic efficiency. Testing to evaluate natural graphite and activated carbon as nucleation layers was also conducted (Figure 39) to determine if either the significantly higher surface area of activated carbon (>1,600 m^2/g) or the significantly lower surface area of the natural graphite flakes (~3 m^2/g) offered an advantage, but neither showed improved performance in comparison to the carbon black (45 m^2/g). However, it is important to note that in addition to differing surface areas, these carbons significantly differ in terms of crystallinity, with the activated carbon containing more defects and sp^3 carbon bonding. Such sites are expected to be more reactive with the electrolyte and maybe the cause of the increase in charge loss observed for the activated carbon electrode.

4.3.2 Additional testing on carbon black nucleation layer

Additional testing using carbon black nucleation layers was performed to evaluate the potential for dendritic growth and evaluate the resting stability of the plated Na metal. Figure 40 shows >30 mAh/cm^2 of continuous plating at 1 mA/cm^2. Disassembling the cell, we see that all of the Na was removed from the negative side of the cell and plated on to the working electrode, forming a shiny, smooth film of Na metal on top of the nucleation layer. This test further confirms that Na can be plated without detrimental dendrites growing, in contrast to a recent report showing that dendritic growth becomes more problematic and apparent with higher plating capacities.[93]

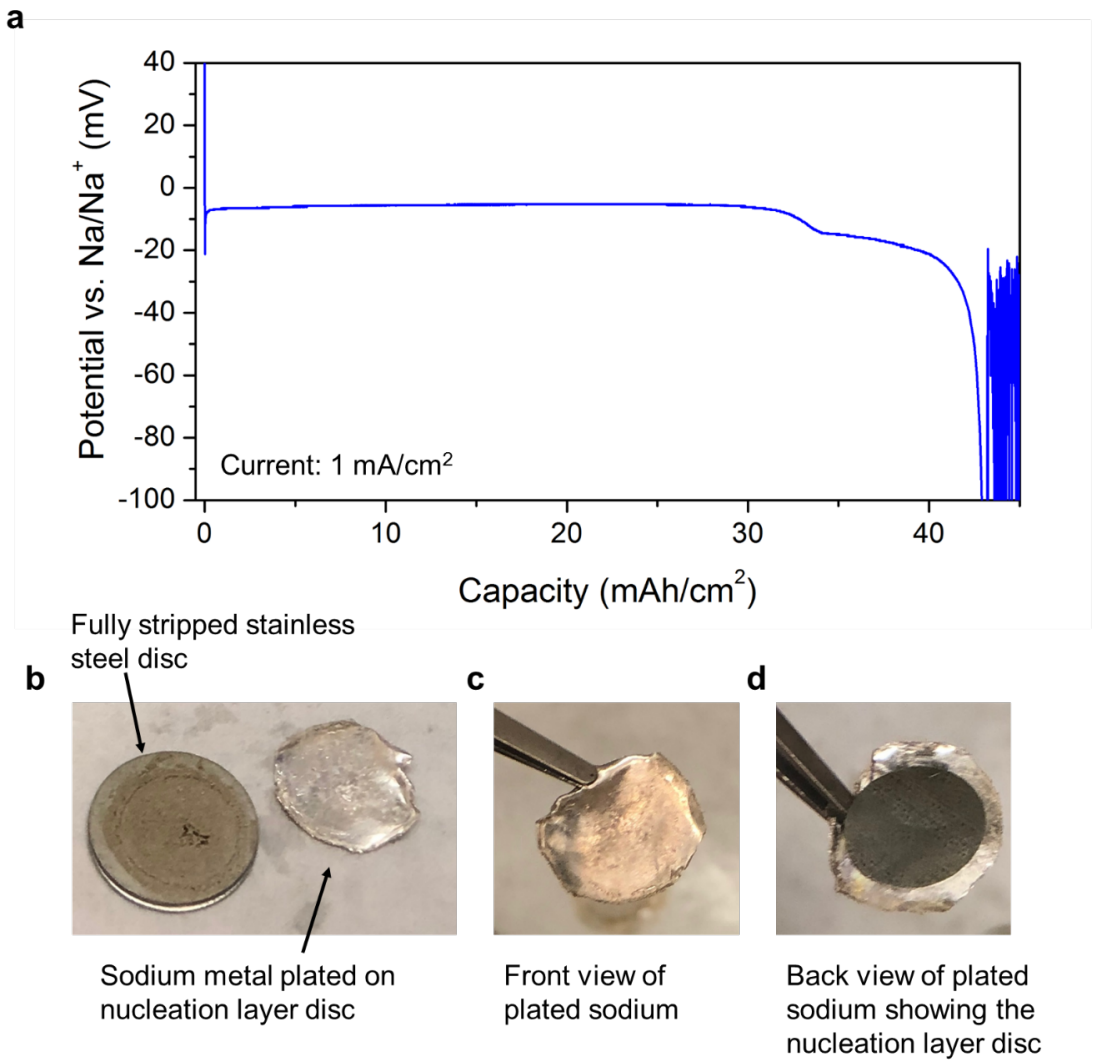

Figure 40: Plating on carbon black nucleation layer in a half-cell configuration until exhaustion of the Na metal counter/reference electrode. Voltage profile shows stable plating over ~30 mAh/cm^2 of operation. Images show the full removal of all the Na metal from the stainless steel disc and the deposition of Na metal on the nucleation layer disc.

Next, the resting stability of the plated Na metal was tested. While battery electrodes are conventionally characterized through galvanostatic cycling, the resting stability of a potentially reactive electrode is very important because commercial batteries are required to store charge in addition to undergoing charging and discharging. Figure 41 shows the Coulombic efficiency of 50 cycles performed at a capacity of 1 mAh/cm^2 with a 10 hour rest period between each plating and stripping step. The

average Coulombic efficiency was found to be 99.73%, which is lower than what we have found without the rest step (~99.9%), indicating additional charge is lost, but the plated Na metal remains relatively well passivated by the SEI layer.

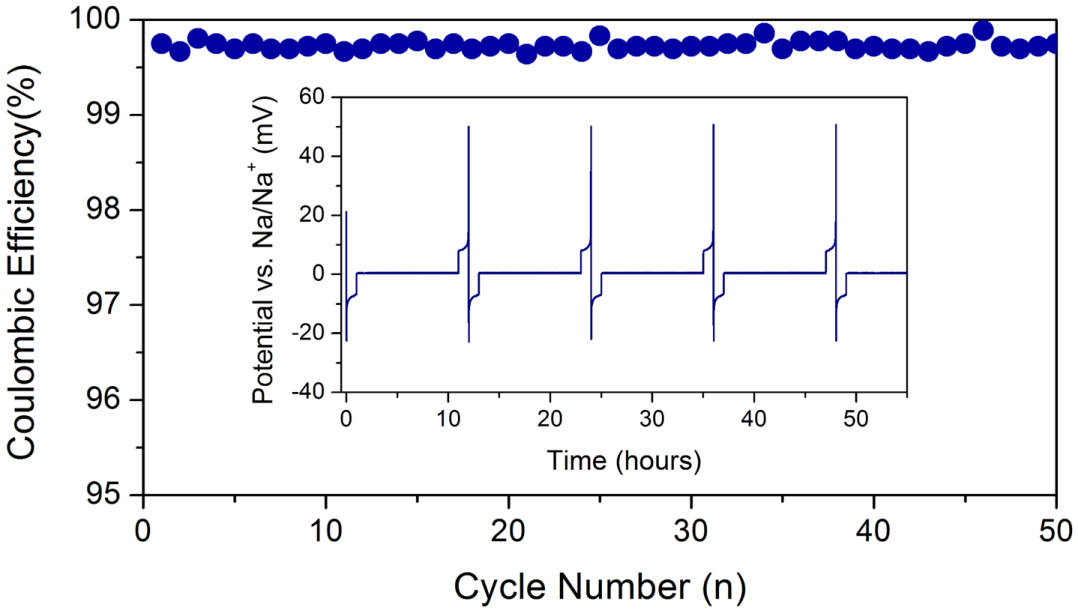

Figure 41: 50 cycles of plating and stripping on a carbon black nucleation layer in a half-cell configuration using a 10 hour rest between each plating and stripping step. The plating current was 1 mA/cm^2 and the plating capacity per cycle was 1 mAh/cm^2. The inset shows the voltage profile for 4½ of these cycles. The average Coulombic efficiency of 99.73% over these 50 cycles indicates that minimal Na is lost during the 10 hour resting period.

4.3.3 Mitigating first-cycle loss

The first-cycle loss of capacity at the negative electrode presents a significant challenge to many new battery chemistries. This is particularly problematic in the case of Na-ion battery development, where hard carbon anodes consume at least 15% of the Na content during the first cycle. While numerous techniques have been proposed to help alleviate this issue, such as pre-charging the anode, adding excess Na/Li to the cathode, and using sacrificial salts, it remains unclear if these techniques can be practically applied for scaled-up manufacturing.[94, 95] Moreover, increasing the mass loading of the cathode is not considered a practical approach to compensate for the loss of Na because this may result

in the unintended plating of Na metal.[96] However, the unbalanced design of the anode-free cell allows us to overcome this key challenge. Although there is first-cycle loss in the anode-free cell that results from the initial sodiation of the nucleation layer and the formation of a solid electrolyte interphase (SEI) layer, the percent loss can be simply reduced by increasing the areal loading of the cathode. In Figure 42, we illustrate this distinction between an insertion anode and a nucleation layer using half-cell testing. Figure 42a shows the first-cycle profile for hard carbon, exhibiting a 16% first-cycle loss. Importantly, this percent will not significantly change with areal loading. In contrast, Figure 42b shows the first-cycle profile for a carbon black nucleation layer (0.25 mg/cm^2), exhibiting only 3.5% first-cycle loss after plating 2 mAh/cm^2. As expected, we observed that this percent loss is dependent on the plating capacity, with lower capacities showing a greater percent loss (Figure 43). In the context of commercial cells, with cathode areal loadings greater than 2 mAh/cm^2, this unique feature of the anode-free approach will be highly advantageous and allow for higher achievable energy densities.

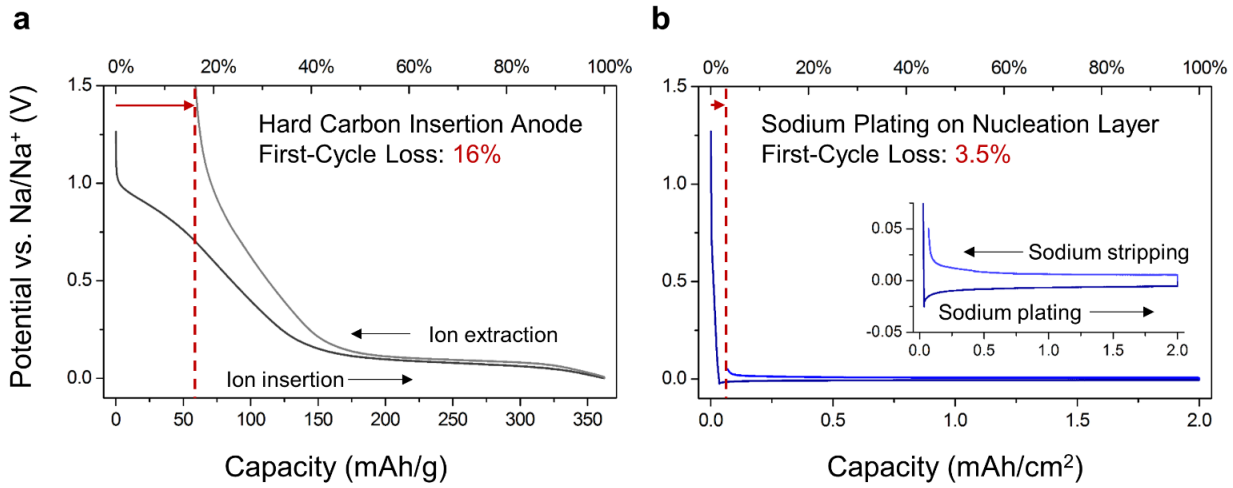

Figure 42: First-cycle voltage profiles for (a) Na-ion storage in hard carbon at 0.1 A/g and (b) Na metal plating on a 0.25 mg/cm^2 carbon black electrode at 0.5 mA/cm^2 for a capacity of 2 mAh/cm^2.

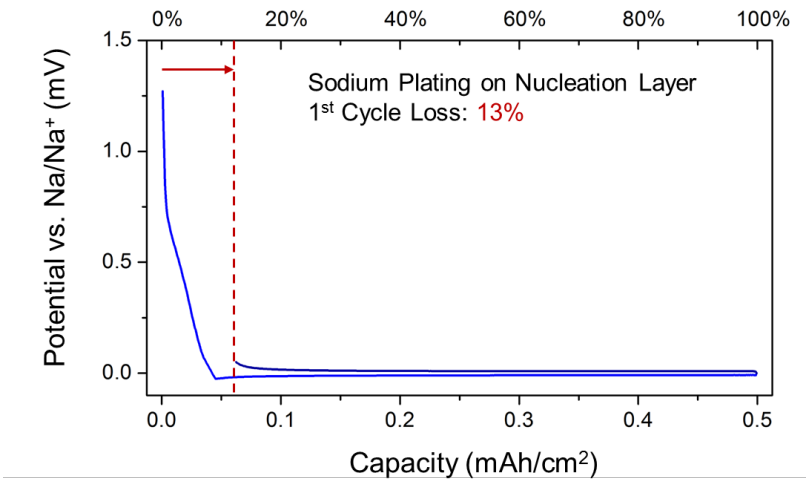

Figure 43: First-cycle voltage profiles for Na metal plating on a 0.25 mg/cm^2 carbon black electrode at 0.5 mA/cm^2 for a capacity of 0.5 mAh/cm^2.

4.4 Conclusion

In this chapter, I focused on a series of materials that exhibit stable performance in glyme-based electrolytes as insertion anodes, and reconsidered their utility as nucleation layers. I found that carbon black, a relatively poor Na-ion anoded, provided the best-suited platform for Na metal deposition. In contrast, both hard carbon and Sn, two of the most promising Na-ion anodes, showed higher irreversible losses as nucleation layers. Building on these findings, I conducted addition half-cell testing using carbon black nucleation layers to show remarkably low first-cycle loss as well as other attractive features.

Chapter 5: An Anode-Free Battery with a $Na_3V_2(PO_4)_3$ Cathode

5.1 Introduction

In chapter 3, I presented a proof-of-concept anode-free Na cell. However, the use of the pre-sodiated pyrite cathode only offered limited cycling at low rates. To make a more commercially viable cell, an air-stable cathode with a higher operating voltage is preferable. In this chapter, I build on my findings from the previous two chapters to report an anode-free cell that operates at 3.35 V, with an exception energy efficiency of 98%, and a longer lifespan. To achieve this, I synthesize a carbon-coated $Na_3V_2(PO_4)_3$ cathode material and assemble full cells with relatively high cathode loadings (~12 mg/cm^2).

5.2 Methods

5.2.1 Material fabrication and characterization

Carbon-coated $Na_3V_2(PO_4)_3$ was synthesized as follows: V_2O_5, $NaH_2PO_4 \cdot H_2O$, and citric acid were combined in a molar ratio of 1:3:3 and then ball milled in ethanol in a planetary ball mill (FRITZ, Pulverisette 7) at 300 RPMs for 24 hours. The resulting green slurry was dried (Figure 44a), hand ground using a mortar and pestle, and subsequently sintered at 350 ^oC in Ar for 4 hours. Afterwards, the powder was hand ground again using a mortar and pestle, pressed into 1 cm diameter discs, and sintered at 800 ^oC in Ar for 8 hours (Figure 44b). Finally, the discs were ground into powder using a mortar and pestle and carbonized under Ar and C_2H_2 (90:10 volumetric flow ratio, respectively) for 30 minutes, while ramping from 600 ^oC to 690 ^oC. Photographs of the dried precursor after ball milling and the discs after sintering are presented in Figure 44. SEM imaging was performed using a Zeiss MERLIN with GEMINI II SEM. XRD was performed using a Rigaku SmartLab XRD.

Figure 44: (a) Dried precursor after ball milling. (b) Sintered $Na_3V_2(PO_4)_3$ discs in ceramic boat.

5.2.2 Electrochemical measurements

High-loading NVP electrodes were made using 5% CMC binder, 5% polyolefin grafted acrylic acid copolymer, and 10% carbon black. These electrodes were processed with water:IPA (80:20 wt%). Slurries were spread onto carbon-coated Al foil (MTI) and then punched as 1 cm diameter discs and dried in a vacuum oven at 70 ^{o}C prior to device assembly. An electrolyte of 1M $NaPF_6$ in diglyme was prepared as described in the previous chapter. Anode-free cells were assembled using a 1 cm diameter

nucleation layer disc, a Celgard 2325 separator, a Whatman glass fiber separator, and a 1 cm diameter cathode disc, ~100 μl of electrolyte, and crimped in CR2032 coin cells.

5.3 Results and discussion

5.3.1 Evaluating the $Na_3V_2(PO_4)_3$ cathode

In choosing a cathode to demonstrate the anode-free approach, it was important to select an air-stable material that is not Na deficient to allow for facile processing. With the target of reaching Li-ion performance, we also sought a cathode to allow for extended cycling, a high specific energy, a stable discharge voltage, and stability in the electrochemical window of the 1M $NaPF_6$ in diglyme electrolyte (Figure 45). After careful consideration, we selected $Na_3V_2(PO_4)_3$: a NASICON compound with an open 3D structure that allows for rapid Na-ion conduction. Specifically, carbon-coated $Na_3V_2(PO_4)_3$ nanoparticles were prepared using a solid-state synthesis after wet ball-milling of the precursors.[97] Figure 46a and b show the synthesized particles and the corresponding x-ray diffraction pattern. To evaluate the cathode properties, half-cell testing was conducted using 1M $NaPF_6$ in diglyme. Figure 46c shows one full cycle between the range of 3.0 and 3.7 V vs. Na/Na^+. The measured capacity of 105 mAh/g is about 90% of the theoretical capacity of 117 mAh/g. The stable discharge voltage at ~3.35 V provides a cathode-specific energy of ~350 Wh/kg. The low voltage hysteresis of 30 mV at a rate of C/6 is less than one hundredth of the operating voltage, allowing for round-trip energy efficiencies approaching 99%. In addition, half-cell cycling without significant capacity decay over 100 cycles is shown in Figure 47.

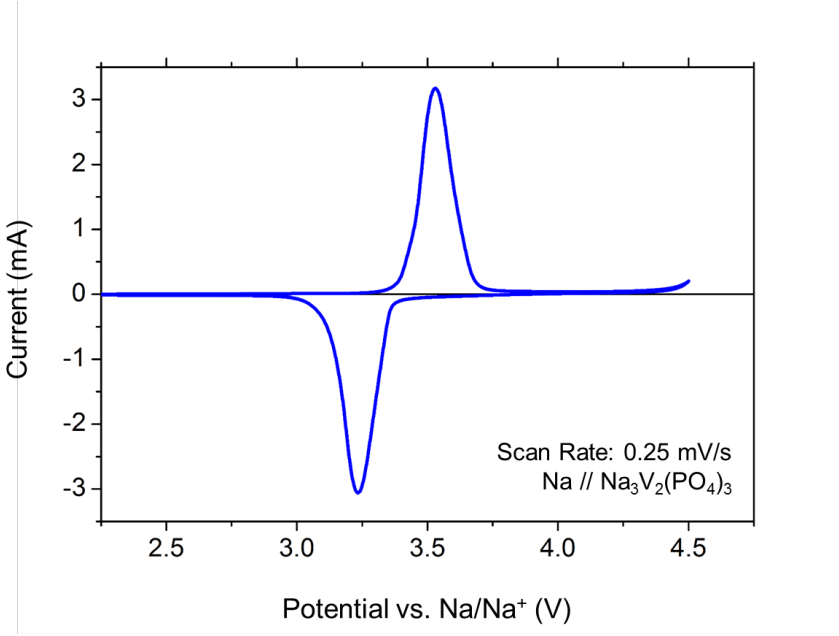

Figure 45: Cyclic voltammogram of $Na_3V_2(PO_4)_3$ half cell performed at 0.25 mV/s to 4.5 V vs. Na/Na^+ using an electrolyte of 1M $NaPF_6$ diglyme.

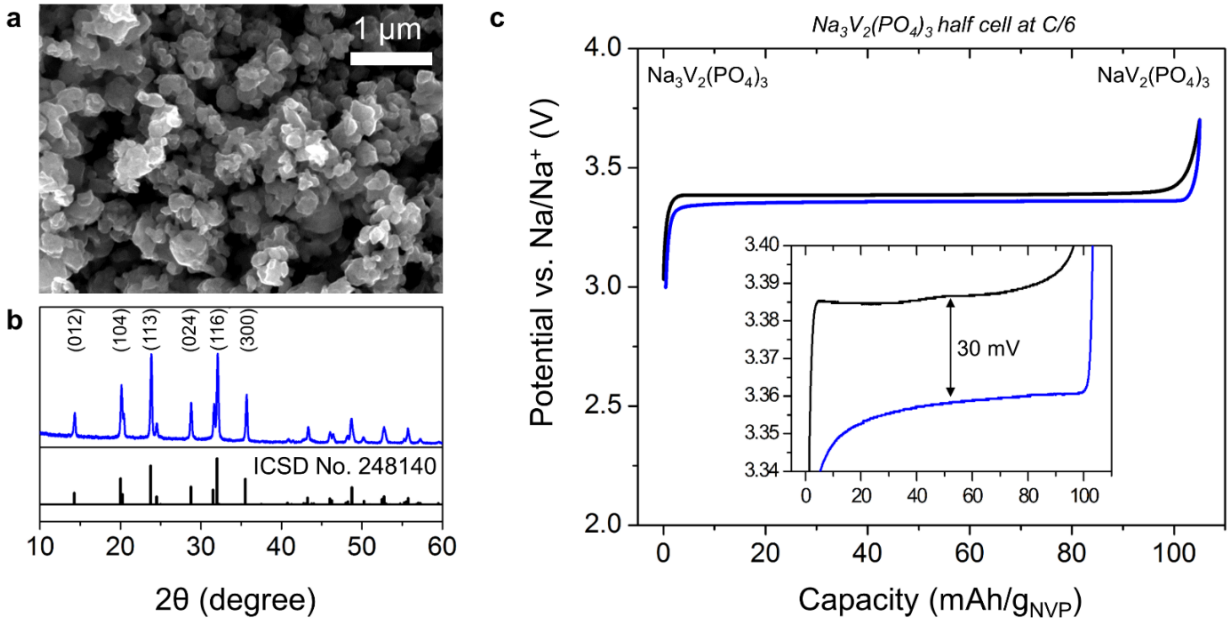

Figure 46: (a) SEM image of $Na_3V_2(PO_4)_3$ particles and corresponding (b) XRD pattern. (c) Voltage profile for $Na_3V_2(PO_4)_3$ half cell at C/6 (where C=117 mA/g).

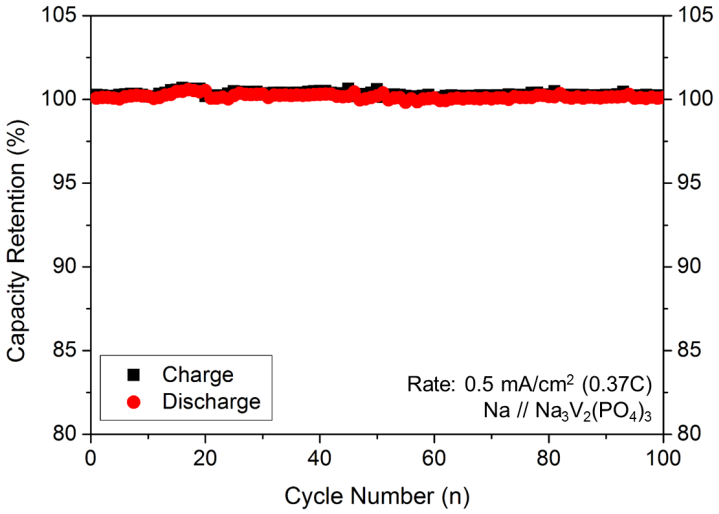

Figure 47: Cycling of $Na_3V_2(PO_4)_3$ in a half-cell configuration performed at 0.5 mA/cm^2 (0.37C) for 100 cycles.

5.3.1 Comparing the anode-free Na battery to the Na-ion battery

A Na-ion battery and an anode-free Na battery using a nucleation layer are both illustrated in Figure 48a. In contrast to a Na-ion battery, the anode-free battery is intentionally unbalanced, and operates through the plating and stripping of Na metal on the nucleation layer at the negative electrode. The use of a nucleation layer, as opposed to plating directly on the Al current collector, stabilizes the plating and stripping of Na (alleviating problems of Na delamination and dendritic growth) and increases the Coulombic efficiency.[90] Figure 48b shows the specific energy of different negative electrodes paired with a $Na_3V_2(PO_4)_3$ cathode, including the anode-free configuration. The reported energy densities are from recent work conducted by Tarascon and coworkers.[26] The maximum specific energy of 388 Wh/kg for the anode-free cell is calculated assuming the mass of the nucleation layer is 1% of the mass of the cathode. The 318 Wh/kg demonstrated in this work is notably 40% higher than the recently reported value for the tin//$Na_3V_2(PO_4)_3$ cell.

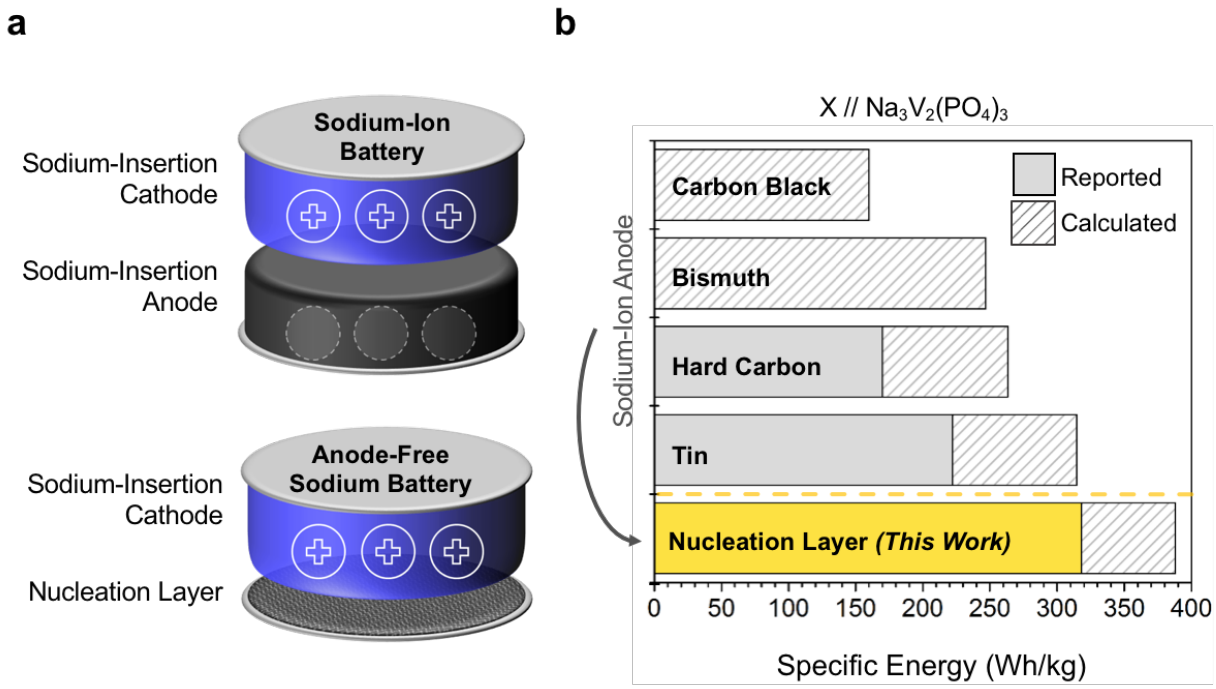

Figure 48: (a) Schematic diagram illustrating the difference between the Na-ion battery and the anode-free Na battery. (b) Specific energy comparison between battery configurations using different negative electrodes with a $Na_3V_2(PO_4)_3$ cathode; the anode-free approach using a nucleation layer is highlighted on the bottom.

5.3.3 Anode-free cell testing

Anode-free cells were assembled and tested (Figure 49) using carbon black (~0.2 mg/cm^2) on Al foil as the negative electrode and $Na_3V_2(PO_4)_3$ (~12 mg/cm^2) on Al foil as the positive electrode. To achieve mass loadings of >10 mg/cm^2 without electrode cracking, isopropyl alcohol was added to the aqueous solution to reduce surface tension.[98] Importantly, no Na metal was used in making these cells, and no modification to the electrodes were made such as pre-sodiation or pre-cycling. Accordingly, this design should allow for manufacturing in line with current methods employed for Li-ion batteries.

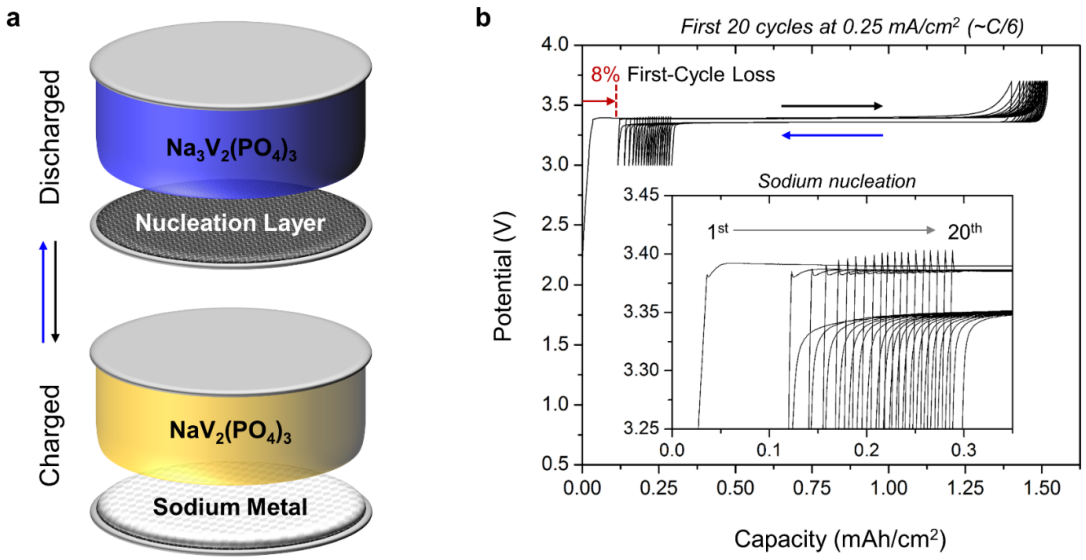

Figure 49: (a) Schematic of the charged and discharged state of the anode-free cell. (b) Slippage profile for the first 20 cycles of the anode-free cell. Inset, nucleation spike during charging.

Figure 49b shows the first 20 cycles of an anode-free cell cycled galvanostatically at 0.25 mA/cm^2 (~C/6 with respect to the cathode) between 3.0 and 3.7 V. In the first cycle, starting at ~0.8 V, the carbon black nucleation layer is sodiated (taking place prior to the flat charging plateau). The transition from Na-ion storage in the carbon black to Na plating is marked by a nucleation spike. In this first cycle, the nucleation spike appears small on the left shoulder of the charging curve (as shown in inset in Figure 49b), but then becomes more pronounced in the subsequent cycles. We attribute this to nucleation initially occurring prior to the cathode reaching its plateau. After Na is lost in the first few cycles, the cathode is never fully sodiated, so the nucleation event aligns with the plateau, and as a result, it is more evident in the voltage profiles. It is also worth noting here that the presence of the nucleation spike observed at the start of each charging step indicates that Na metal is freshly plated on the nucleation layer during each cycle (Figure 51 shows how the magnitude of the nucleation spike evolves with cycling).

In the first cycle, the discharge capacity was 96 mAh/g with respect to the mass of the cathode, or 1.26 mAh/cm^2. The maximum specific energy discharged was 318 Wh/kg with respect to the mass of the cathode and the nucleation layer. The first-cycle loss of 8% includes oxidation of the electrolyte at the cathode in addition to carbon sodiation and SEI formation at the nucleation layer. Stable performance is observed over the first 20 cycles with some evidence of electrolyte oxidation (slippage in the upper right corner of the plot), and additional loss of charge at the negative electrode (further slippage on the left side of the plot). Accordingly, the Coulombic efficiency that levels out around 99.4% after the first five cycles indicates minor parasitic reactions at both electrodes, rather than a direct loss of 0.6% Na per cycle.

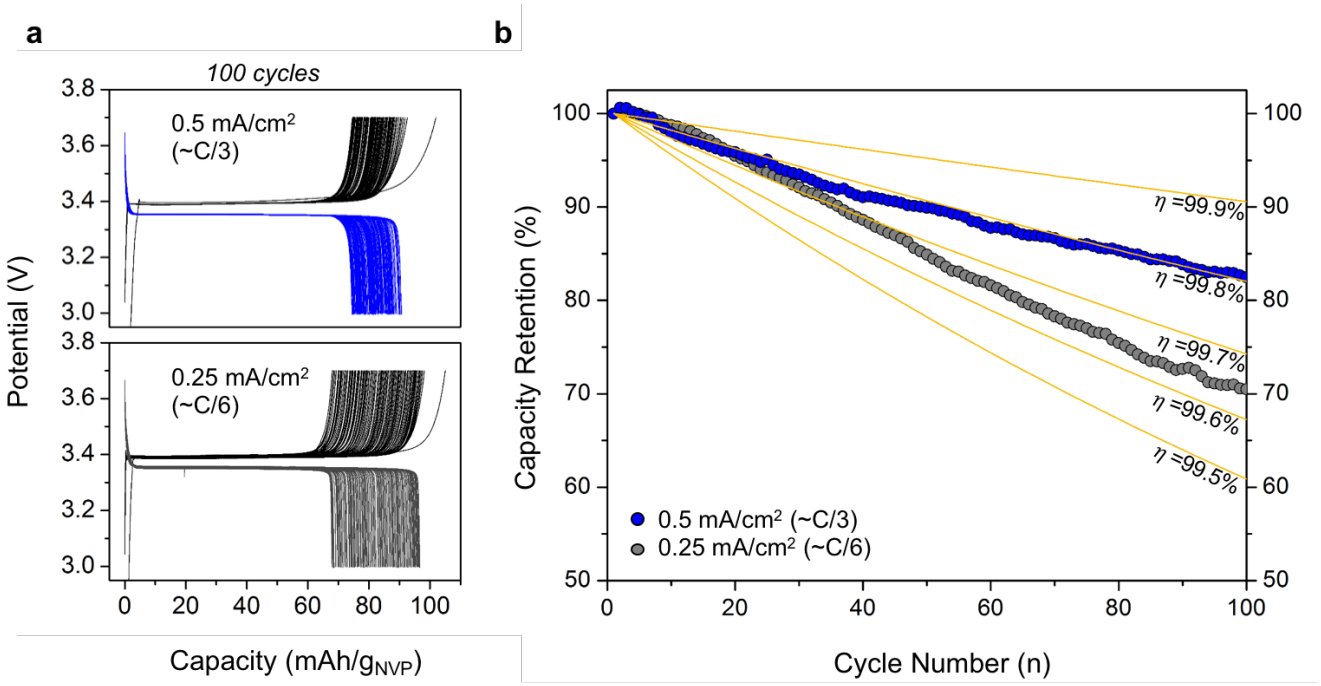

Figure 50: (a) 100-cycle voltage profiles for anode-free cells at 0.50 mA/cm^2 (above) and 0.25 mA/cm^2 (below). (b) Corresponding cycling capacity retention with decay curves plotted for guidance.

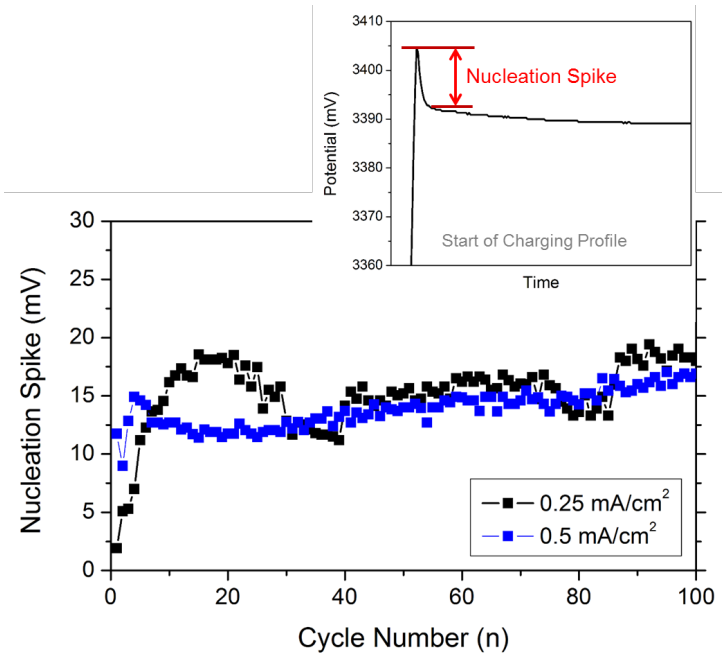

Figure 51: Nucleation spike voltage for anode-free cells cycled at 0.25 mA/cm^2 and 0.5 mA/cm^2. Above, example of the nucleation spike measurement.

Figure 50a and b show the voltage profiles for cells cycled at 0.25 mA/cm^2 (~C/6) and 0.5 mA/cm^2 (~C/3) over 100 cycles, and the corresponding capacity retention with respect to cycle number. Over the first 100 cycles, the capacity retention was 70.4% and 82.5% for the devices cycled at 0.25 mA/cm^2 and 0.5 mA/cm^2, respectively. Additional plots of energy efficiency, Coulombic efficiency, and average charging/discharging voltages over the first 100 cycles are presented in Figures S9 and S10. Since the cathode material exhibited stable performance in half-cell testing, we assume the capacity fade is primarily due to Na loss. This assumption was later confirmed by removing the cathode from an anode-free cell and testing it in a half cell, with the cathode reverting back to full capacity. Accordingly, the capacity retention with respect to cycle number can be described as follows:

$$Q(n) = Q_0\eta^n \qquad \text{(Eq. 4)}$$

where Q is the cell capacity, n is the cycle number, and η is the Na retention per cycle. Decay curves for x= 99.9%, 99.8%, 99.7%, 99.6% and 99.5% are plotted for comparison. The η = 99.9% line corresponds

to the Coulombic efficiency of the plating and stripping on carbon black nucleation layer measured in half cell testing. Our results approximately follow η =99.8% for the device cycled at 0.5 mA/cm^2 and η =99.65% for the device cycled at 0.25 mA/cm^2. The deviation from the half-cell testing may be due to changes in the electrolyte caused by the cathode and/or the deactivation of some Na metal during cycling. The difference in cycling between the two rates can be attributed in part to cycling time,[99] as the device cycled at the slower rate cycled for approximately twice the duration, providing more time for parasitic reactions. In comparison, recent work testing anode-free Li batteries with a $LiFePO_4$ cathode supplied by A123 and a highly concentrated electrolyte showed a capacity retention of ~35% after 100 cycles at 0.2 mA/cm^2,[63] corresponding to η < 99.0%, with cycling at 0.5 mA/cm^2 showing similar performance. The significantly improved capacity retention demonstrated in our work underscores the advantage of using a nucleation layer and the pairing of Na with the 1M $NaPF_6$ in diglyme electrolyte.

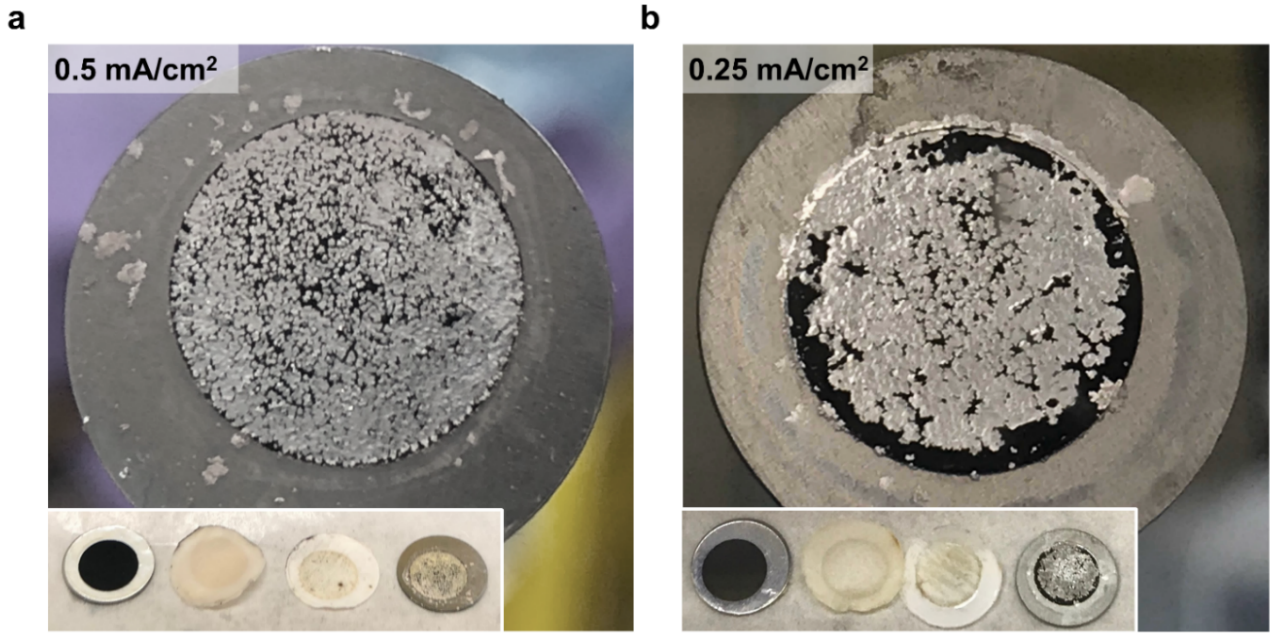

Figure 52: Disassembled anode-free cells after 100+ cycles showing deposited Na metal (charged state) for devices cycled at (a) 0.5 mA/cm^2 and (b) 0.25 mA/cm^2.

Next, to better understand the observed capacity fade with cycling, the anode-free cells characterized in Figure 50 were disassembled in a fully charged state (3.7 V) after 100+ cycles and photographed (Figure 52). Here, we note a relatively uniform covering of the 1 cm diameter nucleation layers (black) with shiny Na metal. As expected,[84] the islands of Na appear smaller in the cell operated at higher current. Interestingly, Na metal is also found adhered to the edges of the nucleation layer discs with patches of duller-gray Na spread onto the larger stainless steel discs. The presence of potentially inactive Na on the stainless steel discs may be due to the geometry of the assembled cells, which produces non-uniform current distributions at the edges of the electrodes. In addition, variations in pressure due to the stack arrangement and the crimping process can deform separators, and have been reported to result in spatial variations in deposition near the edges.[100] With some of the measured cell capacity loss likely explained by the spreading and deactivation of Na, we are optimistic that scaled-up devices will show improved cycling through the reduction of these edge effects. Additional promising routes to reach lifespans competitive with Li-ion batteries include increasing the Coulombic efficiency through the optimization of the nucleation layer and developing methods to incorporate surplus Na into the cells.

Finally, it is worthwhile to note additional unique battery attributes that are enabled by our anode-free approach that are particularly important for system-level integration. First, the voltage during discharge is remarkably stable, with 98% percent of the discharge occurring between 3.4 and 3.3 V when operated at 0.25 mA/cm^2 from 3.7 to 3.0 V. This capability to maintain a constant voltage during discharge may eliminate the need for power electronics (such as boost converters) at the system level that are costly and consume energy. Second, the round-trip energy efficiencies of the anode-free cells were found to be exceptionally high, with averages of 98.1% (0.5 mA/cm^2) and 98.0% (0.25 mA/cm^2) over 100 cycles. This feature is especially attractive in the context of stationary electric storage, where

energy losses reduce the value of batteries as resources to the grid and accumulate to be significant over long operational lifetimes.[101] High energy efficiencies are also expected to allow for simpler and potentially less costly thermal management.

5.4 Conclusion

In this chapter, I developed a Na metal battery using an anode-free assembly, where all the Na is initially stored in an air-stable cathode material for ease of manufacturing. Using the anode-free approach with a $Na_3V_2(PO_4)_3$ cathode, a full-cell was demonstrated to achieve attributes unattainable with the use of conventional Na-ion anodes, including: high specific energy (up to 318 Wh/kg at 0.25 mA/cm^2 with respect to the mass of the cathode and nucleation layer), minimal first-cycle capacity loss (down to 8%), exceptional round-trip energy efficiency (98%), and a stable discharge voltage at 3.35 V. Going forward, additional work needs to be focused on improving the lifespan of these cells, as this remains their key disadvantage.

Chapter 6: Extending the Cycle Life of Anode-Free Batteries using a Cathode with an Ion Reservoir

6.1 Introduction

In this chapter, I present a new strategy to increase the cycle life of anode-free cells by incorporating an additional reserve of metal ions in the cathode. To demonstrate this concept, I utilize Na-enriched NVP, where an additional Na ion is stored through the V^{3+}/V^{2+} redox couple, providing a ~50% surplus of Na, and enabling a full cell with 325 Wh/kg capable of 230 stable cycles with >80% capacity retention. Since a collection of techniques to add a surplus of metal ions to the cathode have already been established for both Li-ion[94, 102-104] and Na-ion[95, 105-107] batteries to offset first-cycle loss, I expect this strategy to be broadly applicable to different chemistries with an array of embodiments, and allow for the design of anode-free batteries capable of significantly longer lifespans.

6.2 Methods

$Na_4V_2(PO_4)_3$ electrodes were prepared as follows: (1) $Na_3V_2(PO_4)_3$ electrodes were prepared as reported in the previous chapter with loadings of ~12mg/cm^2. (2) Half cells using an electrolyte of 1M $NaPF_6$ in diglyme with the $Na_3V_2(PO_4)_3$ electrodes were assembled. (3) Half cells were pre-cycled and then discharged to 1V vs. Na/Na^+. (4) Half cells were disassembled in an Ar glovebox and the $Na_4V_2(PO_4)_3$ electrodes were removed for testing in anode-free cells. All additional methods used in this chapter have been previously described elsewhere in this dissertation.

6.3 Results and discussion

Figure 53a illustrates the projected cycling performance of an anode-free cell with and without an ion reservoir. By considering a reservoir with a 50% excess of ions and a 99.9% Coulombic

efficiency for both cells, we project that the addition of the reservoir can provide a 224% extension of the cell's cycle life with >80% capacity retention. During the first charge, the excess of ions will be electroplated to form a metal surplus at the negative electrode. During the subsequent cycling, this surplus will compensate for the cycle-to-cycle loss of charge. In this manner, the projected cycling of the anode-free cell with the ion reservoir can be segmented into two distinct regimes. First, there is a period of surplus-enable stable cycling. During this period, the surplus is expected to decrease linearly with cycling and allow for a stable capacity to be maintained. This period of stable cycling will continue until the surplus is depleted. In this second period, where there is no longer a surplus, the cell capacity is projected to decay exponentially with cycling, as expected for anode-free cells without the incorporation of an ion reservoir.[63]

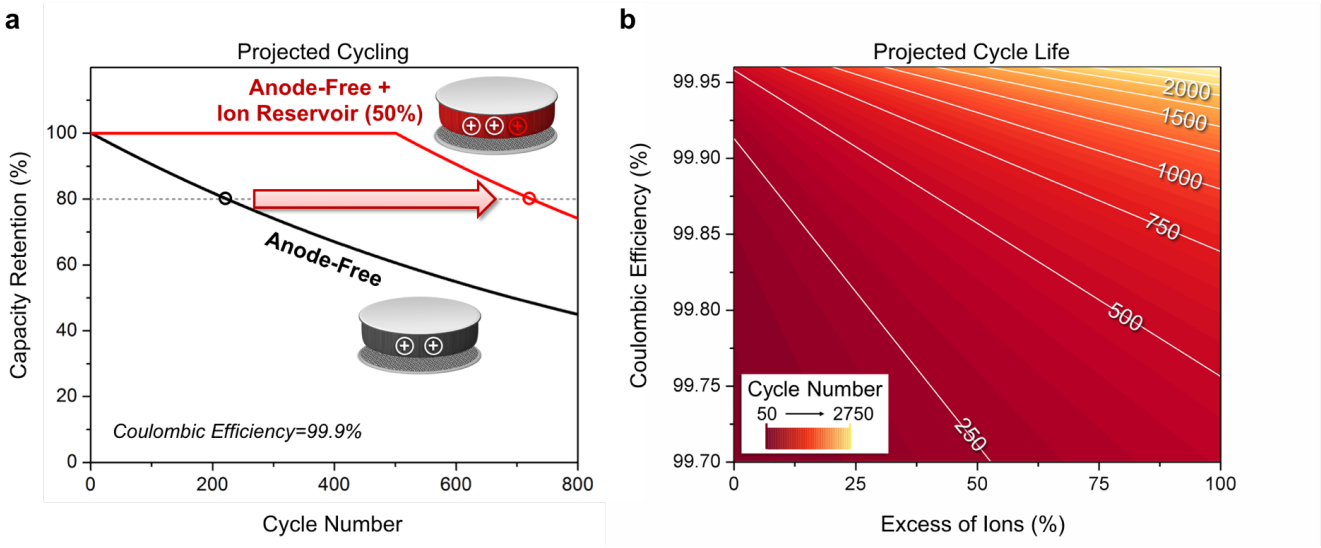

Figure 53: (a) Projected cycling performance of an anode-free cell with (red line) and without (black line) an ion reservoir, assuming a plating-stripping Coulombic efficiency of 99.9%. (b) Projected cycle life where >80% of the initial capacity of an anode-free cell is retained, considering a range of plating-stripping Coulombic efficiencies and ion reservoir sizes, expressed as the excess of ions as a percent of the operating capacity.

Considering this system more generally, we can map out the projected cycle life of cells based on the excess of ions in the reservoir and the plating-stripping Coulombic efficiencies as shown in Figure 53b. Equation 5 shows N, the number of cycles with ≥ 80% capacity, as a function of η, plating-stripping Coulombic efficiency, and Q_R, the excess of ions, expressed as a percent of the cell operating capacity.

$$N(\eta, Q_R) = \frac{\ln(0.8)}{\ln(\eta)} + \frac{Q_R}{1-\eta} \quad (Eq.\ 5)$$

Figure 53b shows that >2000 cycles can be reached when operating at 99.95% Coulombic efficiency with an ion reservoir. While incorporating an ion reservoir into the cell will come at the expense of cell energy density, with this specific relationship dependent on the capacity of the reservoir, this general strategy provides a pathway to engineer anode-free cells to reach specific cycle life and energy density targets.

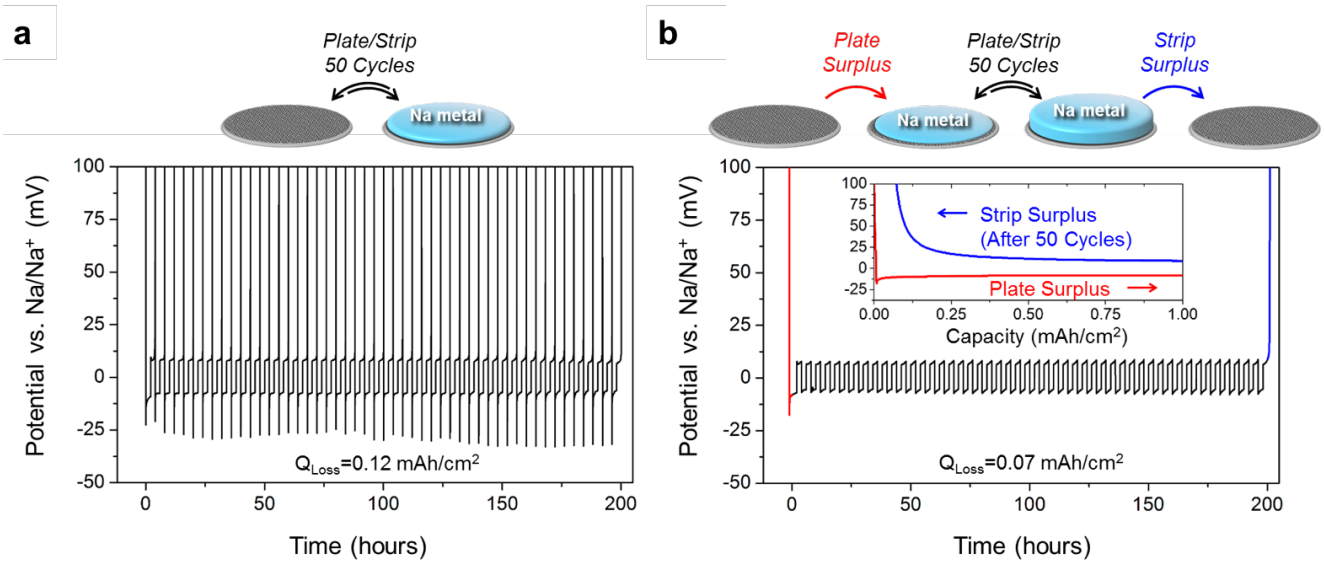

Figure 54: Voltage profiles of 50 cycles of Na metal plating and stripping on carbon black nucleation layers at a current of 1.0 mA/cm^2 with a plating capacity per cycle of 2.0 mAh/cm^2 performed (a) without a Na surplus, using a voltage cutoff per cycle of 100 mV vs. Na/Na$^+$, and (b) after a surplus of 1.0 mAh/cm^2 of Na was first plated (red line), using a 2.0 mAh/cm^2 capacity cutoff per cycle for the 50 cycles, and a final full strip (blue line) with a voltage cutoff of 100 mV vs. Na/Na$^+$ after the 50 cycles. The cumulative loss of charge is shown for both tests as Q_{Loss}.

Underlying our projected cycle life calculations is the assumption that after charging the cell for the first time, the excess ions in the reservoir can be converted to form a surplus of alkali metal at the negative electrode that can be stored without a significant increase in parasitic reactions. To assess this assumption, half-cell testing was performed using an aluminum foil current collector equipped with carbon black nucleation layer as the working electrode. Figure 54 shows the voltage profiles with respect to time from two different cycling protocols. Figure 54a shows a cell cycled with a plating capacity of 2 mAh/cm^2, and a 100 mV voltage cutoff. In this test, fresh Na metal is plated each cycle and then fully removed at the end of the cycle. The average Coulombic efficiency per cycle can be calculated as the total stripped capacity divided by the total plated capacity, and was found to average 99.88%, with 0.12 mA/cm^2 total loss in the first 50 cycles. Figure 54b shows a cell where 1 mAh/cm^2 of Na metal was first plated before the start of the cycling (red line), serving as a 50% surplus. During the subsequent cycling, 2 mAh/cm^2 of Na metal was plated and stripped each cycle, using a stripping capacity cutoff of 2 mAh/cm^2. After 50 cycles, all of the Na metal was fully stripped (blue line) using a voltage cutoff of 100 mV. Since a surplus of Na is left behind each cycle during this cycling protocol, the negative voltage spike characteristic of nucleation present in every cycle in Figure 54a is only observed in the first cycle in Figure 54b. The inset in Figure 54b compares the final stripping capacity (blue line) to the capacity of the initially plated surplus (red line). The difference in capacity of 0.07 mA/cm^2 is the cumulative loss of charge over the 50 cycles, corresponding to an average Coulombic efficiency of 99.93% per cycle. Figure 55 shows a similar test, where the current used to plate the surplus was reduced from 1 mA/cm^2 to 0.1 mA/cm^2, highlighting the initial current as another variable that can be optimized to extend the cell cycle life. Overall, our half-cell testing shows that the surplus of Na metal did not lead to an increase in side reactions over the 50 cycles, an encouraging sign for full cell development using an ion reservoir.

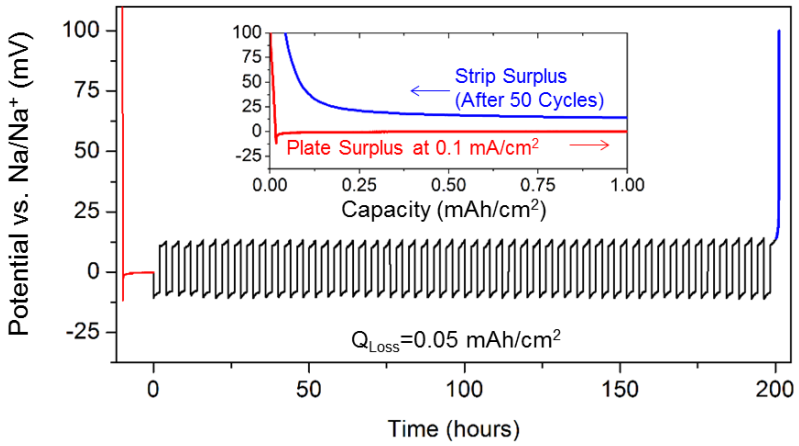

Figure 55: Voltage profiles of 50 cycles of Na metal plating and stripping on a carbon black nucleation layer at a current of 1.0 mA/cm^2 with a plating capacity per cycle of 2.0 mAh/cm^2 performed after a surplus of 1.0 mAh/cm^2 of Na was first plated at a current of 0.1 mA/cm^2 (red line), using a 2.0 mAh/cm^2 capacity cutoff per cycle for the 50 cycles, and a final full strip (blue line) with a voltage cutoff of 100 mV vs. Na/Na$^+$ after the 50 cycles. The cumulative loss of charge is shown as Q_{Loss}.

In order to demonstrate this strategy in an anode-free configuration, carbon-coated $Na_3V_2(PO_4)_3$ nanoparticles were synthesized to function as the Na-ion cathode. While the NASICON-structured $Na_3V_2(PO_4)_3$ is reported to provide a capacity of up to 117 mAh/g during oxidation at 3.4 V vs. Na/Na$^+$, it has also been reported to store an addition 59 mAh/g during reduction at 1.6 V vs. Na/Na$^+$, forming $Na_4V_2(PO_4)_3$.[19] While the potential functionality of this secondary reaction has remained unclear for Na-ion batteries, here, we identify this reactions as an excellent opportunity to create a Na-enriched cathode to provide an ion reservoir for an anode-free cell. To make the $Na_4V_2(PO_4)_3$ phase, we performed an electrochemical reduction, although we expect that ball milling $Na_3V_2(PO_4)_3$ with Na metal can also be carried out in a manner similar to recent work from B. Zhang et al., where they reported the synthesis of $Na_4V_2(PO_4)_2F_3$.[95] The comparative X-ray diffraction patterns of the Na vanadium phosphate before and after electrochemical reduction is shown in Figure 56, with the later matching recent reports of the $Na_4V_2(PO_4)_3$ phase.[108]

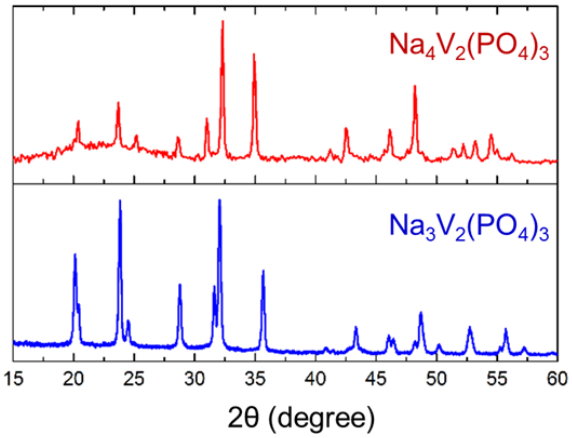

Figure 56: XRD patterns of NVP before (bottom) and after (red) electrochemical reduction. The top pattern was acquired using an air-sensitive sample holder with the pattern from the holder baseline subtracted.

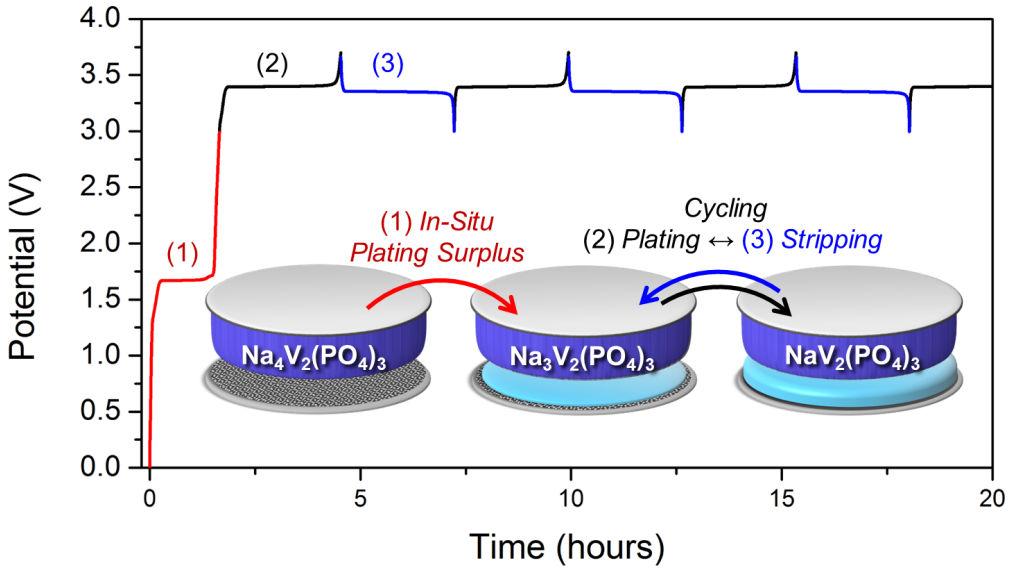

Figure 57: Voltage profile of the first 3 cycles of the anode-free cell with ion reservoir performed at a current of 0.5 mA/cm^2 (~C/3).

Anode-free cells with an ion reservoir were assembled using the $Na_4V_2(PO_4)_3$ cathode, (~12 mg/cm^2) and a carbon black nucleation layer (~0.2 mg/cm^2). Figure 57 shows the first three cycles of an anode-free cell performed galavanostatically at 0.5 mA/cm^2 (~C/3). During the first charge, the cell voltage rises until reaching a flat plateau at 1.6 V where the $Na_4V_2(PO_4)_3$ is oxidized, releasing the excess Na ions that are plated onto the nucleation layer, forming a surplus of Na metal. The end of this

low-voltage plateau signals that the cathode has reached the $Na_3V_2(PO_4)_3$ phase. The subsequent plateau at 3.4 V corresponds to the further oxidation from $Na_3V_2(PO_4)_3$ to $NaV_2(PO_4)_3$, releasing additional Na ions that are plated onto the surplus layer of Na metal. Then, during the discharge process, the Na metal is oxidized at the negative electrode and the ions are stored in the cathode, with the cathode returning from $NaV_2(PO_4)_3$ back to $Na_3V_2(PO_4)_3$. To prevent the stripping of the surplus layer of Na metal, a 3 V discharge cutoff is used. Accordingly, as in the half-cell testing in Figure 54b, a surplus of Na metal is stored on the nucleation layer. In this manner, the incorporation of the ion reservoir creates a cathode-limited cell until the surplus of Na metal is depleted.

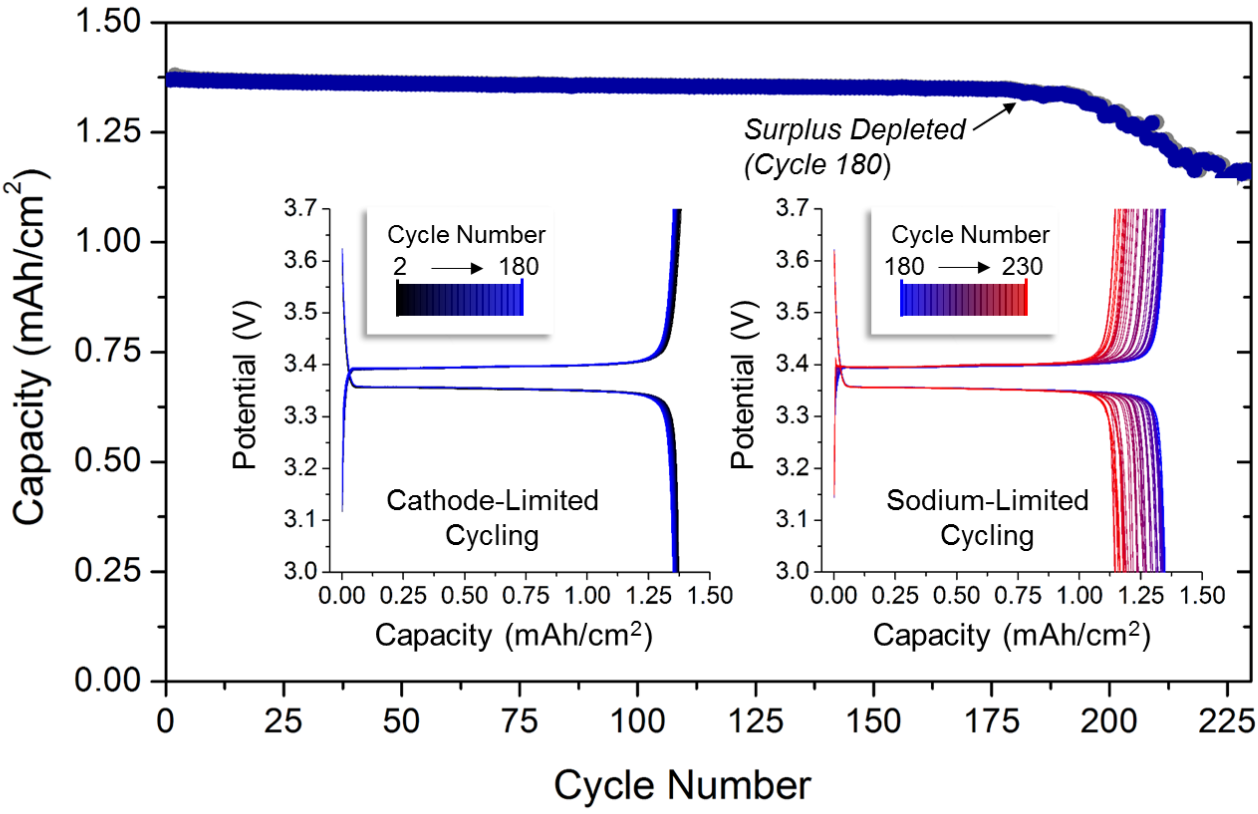

Figure 58: Capacity of anode-free cell with ion reservoir over 230 cycles performed at a current of 0.5 mA/cm² (~C/3). The left inset shows the voltage profile for all cycles from cycle 2 to 180, and the right inset shows the voltage profile for all cycles from cycle 180 to 230.

Figure 58 shows the corresponding cycling performance of this cell performed at a current of 0.5 mAh/cm² (~C/3). As predicted, we observe an extended period of stable cycling followed by a steady

decline in the cell capacity. During the stable period, the cell capacity of 1.37 mAh/cm^2 corresponds to a capacity of 97 mAh/g and a specific energy of 325 Wh/kg, both with respect to the mass of the $Na_4V_2(PO_4)_3$ and the carbon black nucleation layer. Over the first 180 cycles, the capacity retention is >98%, and the average Coulombic efficiency is 99.88% (this corresponds to the $Na_3V_2(PO_4)_3$ Coulombic efficiency). In addition, the low overpotential of both the Na metal plating/stripping and $Na_3V_2(PO_4)_3$ intercalation/deintercalation provides a remarkably high energy efficiency, averaging 98.4% during this period. Surprisingly, this is, to the best of our knowledge, the highest energy efficiency reported to date for a battery system. The voltage profile for every cycle from the second to the 180th are plotted on top of each other in the left inset in Figure 58, showing both a stable capacity and a stable voltage profile. After 180 cycles, the cell capacity begins to steadily decline. The onset of the capacity decline signals that the surplus of Na metal that was plated during the first cycle has been depleted. As a result, the cell transitions from being cathode limited to Na-metal limited. Evidence of this transition can be seen with the appearance of a nucleation spike at the start of the charging voltage profile in these later cycles, as Na metal is re-nucleated at the negative electrode at the start of every cycle (Figure 59). Despite the slow decline in capacity, the right inset in Figure 58 shows that the voltage profile remains consistent in this period. This is important to point out because dendritic growth is reported to cause erratic changes in voltage caused by dendrites momentarily short-circuiting cells.[93] Accordingly, we can conclude from our cycling data that problematic dendritic growth is not an issue. Figure 58 shows 230 cycles with a >80% capacity retention, a significantly extended life span in comparison to other reports,[63, 90, 109] which serves to highlight the impact of our ion-reservoir strategy.

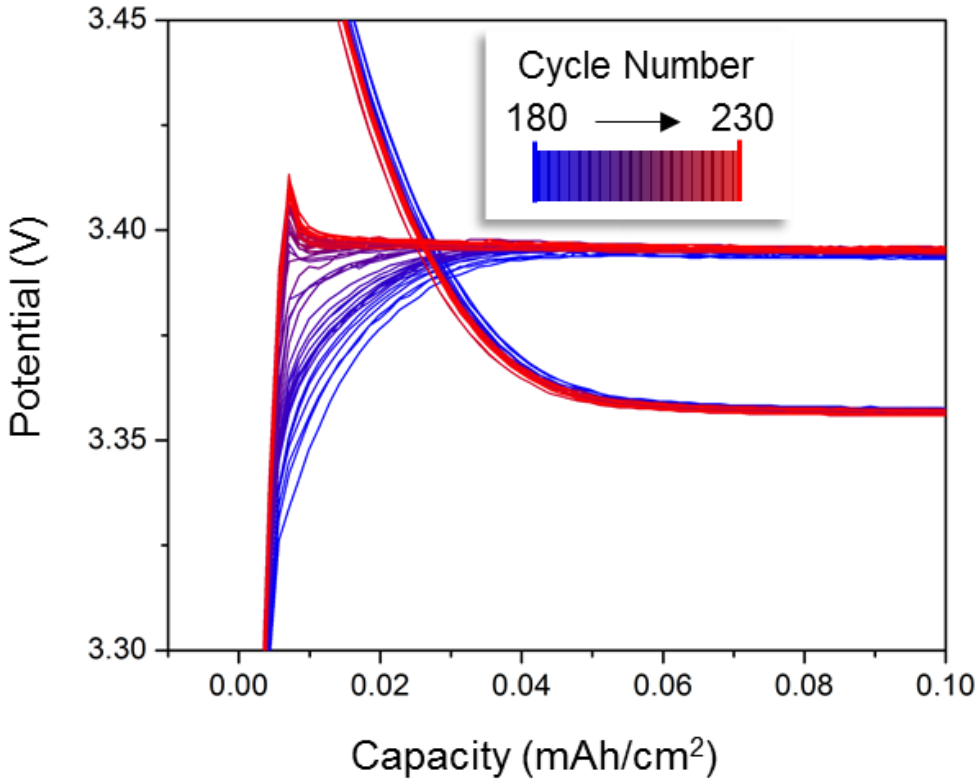

Figure 59: Voltage profile showing the beginning of the charging profile for all cycles from cycle 180 to 230. The spike that emerges corresponds to the nucleation of Na metal. The delay in the emergence of this spike (as the surplus appears depleted by cycle 180) is due to the alignment of the NVP voltage plateau with the nucleation event, requiring the additional loss of Na content from the NVP before the spike aligns with the flat plateau and becomes apparent.

6.4 Conclusion

In conclusion, this work introduces the use of ion reservoir to extend the cycle life of anode-free cells. I demonstrated the feasibility of this approach by first performing half-cell tests using a Na metal surplus, showing >99.9% Coulombic efficiencies, and then full cell testing using Na-enriched Na vanadium phosphate nanoparticles, to reach 230 cycles with >80% capacity retention, a high energy density of 325 Wh/kg, and an exceptional energy efficiency of >98%. By providing a strategy by which cells can be engineered to attain both high energy densities and long cycle lives, my work here opens up new paths to meet the growing demands for high-performance batteries.

Chapter 7: Conclusion

The focus of this research has been to explore opportunities for alternative Na batteries. The great natural abundance of Na and its similarities to Li make it a promising battery chemistry to investigate. However, Na-ion batteries in a form analogous to commercial Li-ion batteries appear unlikely to be able to compete with their Li counterparts in terms of performance (i.e. specific energy or specific power) or cost (in dollars per kWh). For these reasons, my research has been aimed at developing and characterizing alternative options for Na-based batteries that can potentially offer an advantage over Li-ion batteries. In Chapter 2, I examined a cointercalation reaction capable of exceptionally fast charging times and long lifespans, and in Chapters 3-6, I developed an anode-free Na metal battery aimed at competing with Li-ion batteries in terms of specific energy and cost. In this final chapter, I will briefly summarize the findings of this thesis and offer my perspective on the future.

7.1 Summary and outlook

In Chapter 2, I examined the cointercalation of Na ions and diglyme solvent into graphitic carbon. The remarkable rate (achieving up to 12 second charging times) and extended lifespan (96% capacity retention after 8,000 cycles) of this reaction motivated me to system seek a better understanding of the underlying mechanism. By conducting a series of in-situ Raman experiments, I was able to resolve the staging behavior and correlate the stage number with the electrochemical data. I found that unlike the naked intercalation of Li ions or K ions into graphite, the cointercalation of Na ions and solvent did not initially create a dilute stage 1 compound. In addition, I was able to highlight that after reaching a stage 1 compound, there appeared to be further packing of the ion galleries, resulting in supercapacitor-like storage. Furthermore, I was able to apply the findings of Chen et al. (published in

Nature) to a staging reaction in-situ for the first time, and identify the Fermi level of the stage 1 and stage 2 intercalation compounds.

While I did not develop full cells utilizing solvated Na-ion cointercalation, there have been numerous reports by others, including the pairing of a carbon-coated $Na_3V_2(PO_4)_3$ cathode (similar to the material synthesized in Chapter 5) and the pairing of a high surface area carbon electrode, to demonstrate high-rate performance.[110, 111] In addition, there have been a number of interesting follow-up studies further characterizing the solvated Na ion cointercalation process utilizing atomic force microscopy[112] and electrochemical dilatometry[113] as well explorations of different ethers.[114, 115]

Beyond energy storage, the fast reaction kinetics, the large volume change, and the high reversibility of the cointercalation process are attractive for mechanical actuation and sensing. In 2006, Yet-Ming Chiang's group at MIT reported an assessment of different intercalation-driven actuators.[22] While actuators relying on the intercalation of Li ions into graphite result in slow actuation (>100 seconds) and ~10% volume change, the solvated Na-ion cointercaltion into graphite offers significantly faster actuation (<15 seconds) and a far greater volume change (~260%). To take advantage of these properties, I have assisted Nitin Muralidharan (at Vanderbilt) in his recent work evaluating cointercalation for a symmetric energy harvesting device (manuscript in preparation). I have also collaborated with Zack Coppens and Chibuzor Fabian Ugwu in Jason Valentine's group with the aim of developing an electrochemically actuated dynamic metamaterial to function as a low-power display. In this design, the distance between an array of metal resonators and a reflective backplane is tuned by the intertercalation/deintercalation of solvated Na ions into a few-layer graphene spacer layer. In our initial testing, we have measured fast switching times (~200 mS), and we expect faster switching may achievable by shortening the diffusion length. More information on this device design can be found in the dissertation of Zack Coppens.[116]

In Chapters 3-6, I developed an anode-free Na metal battery. In Chapter 3, I found that a nucleation layer improved the plating and stripping of Na metal on an Al current collector, as it appeared to improve the connection between the current collector and the Na metal film and promote more uniform plating. Building on these findings, I went on to demonstrate the first anode-free Na metal battery by using a presodiated pyrite cathode. The exceptional specific energy of the full cell together with the promising cycling performance observed in the half cell testing encouraged me to continue to explore this anode-free approach. In Chapter 4, I investigated a range of different materials as nucleation layers. I compared the Na-ion storage properties of these materials, the Na metal nucleation energetics of Na plating on these materials, and their performance as nucleation layers. I found that carbon black was the best material for minimizing irreversible charge loss, and attributed the improved performance to the expected lower surface area of the nucleated Na metal on this nucleation layer. In Chapter 5, I selected and synthesized the cathode material $Na_3V_2(PO_4)_3$ to pair with the carbon black nucleation layer to demonstrate an anode-free cell to that can be assembled using air-stable electrodes. In comparison to a Na-ion cell with this cathode, I showed the anode-free cell to have a 40% greater specific energy. In addition, I showed higher energy efficiencies (98%) and flatter discharges (remaining constant at 3.35 V) with this approach than can otherwise be achieved. Cycling tests, however, revealed that these cells were limited to ~100 cycles. Finally, in Chapter 6, I presented a new strategy to increase the cycle life of these cell by including an excess Na in the cathode. The introduction of a Na surplus provided the opportunity to experiment with the initial plating current for depositing the initial Na metal. Here, I found initial evidence that a lower current improved the later Coulombic efficiency. As in Chapter 4, I attributed the improved performance to the expected lower surface area of the nucleated Na metal when using lower currents. Finally, I demonstrated that the incorporation of a Na reservoir could extend the cycle life from ~100 cycles to ~230 cycles.

Moving forward, the anode-free approach can be tailored to achieve a range of performance goals and satisfy different design constraints. With respect to specific energy, cathodes can be selected to provide up to 500 Wh/kg with options such as fluorophosphates with elevated operating voltages,[15] or nickel-containing O3-type layered oxides with higher capacities.[14, 45] Alternatively, transitioning from vanadium to more abundant and environmentally-benign transition metals (iron and/or manganese) may be of interest, potentially through the use of Prussian white[17] or iron sulfates[18]. Of these different cathode pairings, the rhombohedral Prussian white, $Na_2Fe[Fe(CN)_6]$, that was first reported by Goodenough's group[3] appears to be the ideal combination of high energy, abundant raw materials, and compatibility with glymes. While it is not included in this dissertation, I worked to synthesize a similar Prussian white material, but struggled to develop an anode-free cell capable of satisfactory cycling. While I attribute the poor reversibility of the cells I tested to the presence of trapped water and other contaminants in the Prussian white material, recent work from Rudola et al., showing that drying above 240 ^oC in an Ar environment can sufficiently dehydrate the material,[117] is very encouraging. Interestingly, this same group published a follow-up paper in 2018 using their Prussian white material to make an anode-free Na battery using a bare Cu current collector and an electrolyte of $NaBF_4$ in tetraglyme with a high specific energy of 336 Wh/kg and a moderate cycle lifespan (<100 cycles).[109] I think a incorporating a nucleation layer and switching to $NaPF_6$ salt could further advance this system.

In addition, I am excited about the use of high cathode areal loadings to boost the cycle life and the specific energy of these cells, as an increase in the plating capacity per unit area will reduce the first-cycle loss and improves the Coulombic efficiency of subsequent cycles. In regard to safety considerations, the stability of the Na metal in the diglyme electrolyte and the capability to discharge the cell to a Na metal-free state are an encouraging start. Future progress in this direction may include the

development of non-flammable polymer electrolytes, advanced separators, and diagnostic tools adapted to this battery type.

References

1. M. S. Whittingham, *Science*, 1976, **192**, 1126-1127.
2. J. M. Tarascon and M. Armand, *Nature*, 2001, **414**, 359.
3. J. B. Goodenough and K.-S. Park, *J. Am. Chem. Soc.*, 2013, **135**, 1167-1176.
4. M. Winter, J. O. Besenhard, M. E. Spahr and P. Novak, *Adv. Mater.*, 1998, **10**, 725-763.
5. M. Dresselhaus and G. Dresselhaus, *Adv. Phys.*, 1981, **30**, 139-326.
6. V. Etacheri, R. Marom, R. Elazari, G. Salitra and D. Aurbach, *Energy Environ. Sci.*, 2011, **4**, 3243-3262.
7. G. E. Blomgren, *J. Electrochem. Soc.*, 2017, **164**, A5019-A5025.
8. F. Schipper, E. M. Erickson, C. Erk, J.-Y. Shin, F. F. Chesneau and D. Aurbach, *J. Electrochem. Soc.*, 2017, **164**, A6220-A6228.
9. J. W. Choi and D. Aurbach, *Nat. Rev. Mater.*, 2016, **1**, 16013.
10. J.-Y. Hwang, S.-T. Myung and Y.-K. Sun, *Chem. Soc. Rev.*, 2017, **46**, 3529-3614.
11. C. Delmas, J.-J. Braconnier, C. Fouassier and P. Hagenmuller, *Solid State Ionics*, 1981, **3**, 165-169.
12. P. K. Nayak, L. Yang, W. Brehm and P. Adelhelm, *Angew. Chem. Int. Ed.*, 2017.
13. N. Yabuuchi, M. Kajiyama, J. Iwatate, H. Nishikawa, S. Hitomi, R. Okuyama, R. Usui, Y. Yamada and S. Komaba, *Nat. Mater.*, 2012, **11**, 512-517.
14. M. H. Han, E. Gonzalo, G. Singh and T. Rojo, *Energy Environ. Sci.*, 2015, **8**, 81-102.
15. Y.-U. Park, D.-H. Seo, H.-S. Kwon, B. Kim, J. Kim, H. Kim, I. Kim, H.-I. Yoo and K. Kang, *J. Am. Chem. Soc.*, 2013, **135**, 13870-13878.
16. B. Ellis, W. Makahnouk, Y. Makimura, K. Toghill and L. Nazar, *Nat. Mater.*, 2007, **6**, 749-753.
17. L. Wang, J. Song, R. Qiao, L. A. Wray, M. A. Hossain, Y.-D. Chuang, W. Yang, Y. Lu, D. Evans, J.-J. Lee, V. Sean, X. Zhao, M. Nishijima, S. Kakimoto and J. B. Goodenough, *J. Am. Chem. Soc.*, 2015, **137**, 2548-2554.
18. P. Barpanda, G. Oyama, S.-i. Nishimura, S.-C. Chung and A. Yamada, *Nat. Commun.*, 2014, **5**, 4358.
19. Z. Jian, L. Zhao, H. Pan, Y.-S. Hu, H. Li, W. Chen and L. Chen, *Electrochem. Commun.*, 2012, **14**, 86-89.
20. Y. Liu, B. V. Merinov and W. A. Goddard, *Natl. Acad. Sci. U.S.A.*, 2016, **113**, 3735-3739.
21. Y. Kim, K. H. Ha, S. M. Oh and K. T. Lee, *Chem. Eur. J.*, 2014, **20**, 11980-11992.
22. Z. Li, M. S. Pan, L. Su, P.-C. Tsai, A. F. Badel, J. M. Valle, S. L. Eiler, K. Xiang, F. R. Brushett and Y.-M. Chiang, *Joule*, 2017, **1**, 306-327.
23. P. Hartmann, C. L. Bender, M. Vračar, A. K. Dürr, A. Garsuch, J. Janek and P. Adelhelm, *Nat. Mater.*, 2013, **12**, 228-232.
24. B. Jache and P. Adelhelm, *Angew. Chem. Int. Ed.*, 2014, **53**, 10169-10173.
25. Z. Hu, Z. Q. Zhu, F. Y. Cheng, K. Zhang, J. B. Wang, C. C. Chen and J. Chen, *Energy Environ. Sci.*, 2015, **8**, 1309-1316.
26. B. Zhang, G. Rousse, D. Foix, R. Dugas, D. A. D. Corte and J. M. Tarascon, *Adv. Mater.*, 2016, **28**, 9824-9830.
27. X. Han, Y. Gong, K. K. Fu, X. He, G. T. Hitz, J. Dai, A. Pearse, B. Liu, H. Wang, G. Rubloff, Y. Mo, V. Thangadurai, E. Wachsman and L. Hu, *Nat. Mater.*, 2017, **16**, 572.

28. H. Kim, J. Hong, Y. U. Park, J. Kim, I. Hwang and K. Kang, *Adv. Funct. Mater.*, 2015, **25**, 534-541.
29. Z. Chen, W. Ren, L. Gao, B. Liu, S. Pei and H.-M. Cheng, *Nat. Mater.*, 2011, **10**, 424-428.
30. L. Malard, M. Pimenta, G. Dresselhaus and M. Dresselhaus, *Phys. Rep.*, 2009, **473**, 51-87.
31. A. C. Ferrari and D. M. Basko, *Nat. Nanotechnol.*, 2013, **8**, 235-246.
32. A. Reina, X. Jia, J. Ho, D. Nezich, H. Son, V. Bulovic, M. S. Dresselhaus and J. Kong, *Nano Lett.*, 2008, **9**, 30-35.
33. T. Maluangnont, G. T. Bui, B. A. Huntington and M. M. Lerner, *Chem. Mater.*, 2011, **23**, 1091-1095.
34. M.-C. Lin, M. Gong, B. Lu, Y. Wu, D.-Y. Wang, M. Guan, M. Angell, C. Chen, J. Yang and B.-J. Hwang, *Nature*, 2015.
35. T. Abe, H. Fukuda, Y. Iriyama and Z. Ogumi, *J. Electrochem. Soc.*, 2004, **151**, A1120-A1123.
36. D. Aurbach, B. Markovsky, I. Weissman, E. Levi and Y. Ein-Eli, *Electrochim. Acta*, 1999, **45**, 67-86.
37. L. Jaber-Ansari, K. P. Puntambekar, H. Tavassol, H. Yildirim, A. Kinaci, R. Kumar, S. J. Saldaña, A. A. Gewirth, J. P. Greeley and M. K. Chan, *ACS Appl. Mater. Interfaces*, 2014, **6**, 17626-17636.
38. A. P. Cohn, N. Muralidharan, R. Carter, K. Share, L. Oakes and C. L. Pint, *J. Mater. Chem. A*, 2016, **4**, 14954-14959.
39. A. M. Dimiev, G. Ceriotti, N. Behabtu, D. Zakhidov, M. Pasquali, R. Saito and J. M. Tour, *ACS nano*, 2013, **7**, 2773-2780.
40. A. P. Cohn, K. Share, R. Carter, L. Oakes and C. L. Pint, *Nano Lett.*, 2016, **16**, 543-548.
41. S. Pisana, M. Lazzeri, C. Casiraghi, K. S. Novoselov, A. K. Geim, A. C. Ferrari and F. Mauri, *Nat. Mater.*, 2007, **6**, 198-201.
42. A. Das, S. Pisana, B. Chakraborty, S. Piscanec, S. Saha, U. Waghmare, K. Novoselov, H. Krishnamurthy, A. Geim and A. Ferrari, *Nat. Nanotechnol.*, 2008, **3**, 210-215.
43. C.-F. Chen, C.-H. Park, B. W. Boudouris, J. Horng, B. Geng, C. Girit, A. Zettl, M. F. Crommie, R. A. Segalman and S. G. Louie, *Nature*, 2011, **471**, 617-620.
44. W. Bao, J. Wan, X. Han, X. Cai, H. Zhu, D. Kim, D. Ma, Y. Xu, J. N. Munday and H. D. Drew, *Nat. Commun.*, 2014, **5**.
45. J.-Y. Hwang, S.-M. Oh, S.-T. Myung, K. Y. Chung, I. Belharouak and Y.-K. Sun, *Nat. Commun.*, 2015, **6**, 6865.
46. W. Zhao, P. H. Tan, J. Liu and A. C. Ferrari, *J. Am. Chem. Soc.*, 2011, **133**, 5941-5946.
47. J. C. Chacon-Torres, L. Wirtz and T. Pichler, *ACS nano*, 2013, **7**, 9249-9259.
48. M. Inaba, H. Yoshida, Z. Ogumi, T. Abe, Y. Mizutani and M. Asano, *J. Electrochem. Soc.*, 1995, **142**, 20-26.
49. N. A. W. Holzwarth, S. G. Louie and S. Rabii, *Phys. Rev. B*, 1983, **28**, 1013.
50. A. M. Dimiev, S. M. Bachilo, R. Saito and J. M. Tour, *ACS nano*, 2012, **6**, 7842-7849.
51. E. Pollak, B. Geng, K.-J. Jeon, I. T. Lucas, T. J. Richardson, F. Wang and R. Kostecki, *Nano Lett.*, 2010, **10**, 3386-3388.
52. F. Wang, Y. Zhang, C. Tian, C. Girit, A. Zettl, M. Crommie and Y. R. Shen, *Science*, 2008, **320**, 206-209.
53. J. Chacon-Torres, A. Ganin, M. Rosseinsky and T. Pichler, *Phys. Rev. B*, 2012, **86**, 075406.
54. M. D. Slater, D. Kim, E. Lee and C. S. Johnson, *Adv. Funct. Mater.*, 2013, **23**, 947-958.
55. H. Li, L. Peng, Y. Zhu, D. Chen, X. Zhang and G. Yu, *Energy Environ. Sci.*, 2016, **9**, 3399-3405.

56. J. Ding, H. Zhou, H. Zhang, T. J. Stephenson, Z. Li, D. Karpuzov and D. Mitlin, *Energy Environ. Sci.*, 2017, **10**, 153-165.
57. D. A. Stevens and J. R. Dahn, *J. Electrochem. Soc.*, 2000, **147**, 1271-1273.
58. E. M. Lotfabad, J. Ding, K. Cui, A. Kohandehghan, W. P. Kalisvaart, M. Hazelton and D. Mitlin, *ACS nano*, 2014, **8**, 7115-7129.
59. F. Shen, W. Luo, J. Q. Dai, Y. G. Yao, M. W. Zhu, E. Hitz, Y. F. Tang, Y. F. Chen, V. L. Sprenkle, X. L. Li and L. B. Hu, *Adv. Energy Mater.*, 2016, **6**, 1600377.
60. C. Bommier, T. W. Surta, M. Dolgos and X. L. Ji, *Nano Lett.*, 2015, **15**, 5888-5892.
61. J. Ding, H. Zhou, H. Zhang, T. Stephenson, Z. Li, D. Karpuzov and D. Mitlin, *Energy Environ. Sci.*, 2017, **10**, 153-165.
62. H. L. Zhu, Z. Jia, Y. C. Chen, N. Weadock, J. Y. Wan, O. Vaaland, X. G. Han, T. Li and L. B. Hu, *Nano Lett.*, 2013, **13**, 3093-3100.
63. J. Qian, B. D. Adams, J. Zheng, W. Xu, W. A. Henderson, J. Wang, M. E. Bowden, S. Xu, J. Hu and J. G. Zhang, *Adv. Funct. Mater.*, 2016, **26**, 7094-7102.
64. D. I. Iermakova, R. Dugas, M. R. Palacin and A. Ponrouch, *J. Electrochem. Soc.*, 2015, **162**, A7060-A7066.
65. Z. W. Seh, J. Sun, Y. Sun and Y. Cui, *ACS Cent. Sci.*, 2015, **1**, 449-455.
66. R. Cao, K. Mishra, X. Li, J. Qian, M. H. Engelhard, M. E. Bowden, K. S. Han, K. T. Mueller, W. A. Henderson and J.-G. Zhang, *Nano Energy*, 2016, **30**, 825–830.
67. W. Luo, C.-F. Lin, O. Zhao, M. Noked, Y. Zhang, G. W. Rubloff and L. Hu, *Adv. Energy Mater.*, 2016, 1601526.
68. G. Y. Zheng, S. W. Lee, Z. Liang, H. W. Lee, K. Yan, H. B. Yao, H. T. Wang, W. Y. Li, S. Chu and Y. Cui, *Nat. Nanotechnol.*, 2014, **9**, 618-623.
69. P. Bai, J. Li, F. R. Brushett and M. Z. Bazant, *Energy Environ. Sci.*, 2016, **9**, 3221-3229.
70. E. Kazyak, K. N. Wood and N. P. Dasgupta, *Chem. Mater.*, 2015, **27**, 6457-6462.
71. C. P. Yang, Y. X. Yin, S. F. Zhang, N. W. Li and Y. G. Guo, *Nat. Commun.*, 2015, **6**, 8058.
72. R. Zhang, X. B. Cheng, C. Z. Zhao, H. J. Peng, J. L. Shi, J. Q. Huang, J. F. Wang, F. Wei and Q. Zhang, *Adv. Mater.*, 2016, **28**, 2155-2162.
73. Q. B. Yun, Y. B. He, W. Lv, Y. Zhao, B. H. Li, F. Y. Kang and Q. H. Yang, *Adv. Mater.*, 2016, **28**, 6932.
74. Z. Liang, G. Y. Zheng, C. Liu, N. Liu, W. Y. Li, K. Yan, H. B. Yao, P. C. Hsu, S. Chu and Y. Cui, *Nano Lett.*, 2015, **15**, 2910-2916.
75. K. Yan, Z. Lu, H.-W. Lee, F. Xiong, P.-C. Hsu, Y. Li, J. Zhao, S. Chu and Y. Cui, *Nat. Energy*, 2016, **1**, 16010.
76. D. Lin, Y. Liu, Z. Liang, H.-W. Lee, J. Sun, H. Wang, K. Yan, J. Xie and Y. Cui, *Nat. Nanotechnol.*, 2016, **11**, 626–632.
77. W. Xu, J. Wang, F. Ding, X. Chen, E. Nasybulin, Y. Zhang and J.-G. Zhang, *Energy Environ. Sci.*, 2014, **7**, 513-537.
78. K. N. Wood, E. Kazyak, A. F. Chadwick, K.-H. Chen, J.-G. Zhang, K. Thornton and N. P. Dasgupta, *ACS Cent. Sci.*, 2016, **2**, 790–801.
79. B. Neudecker, N. Dudney and J. Bates, *J. Electrochem. Soc.*, 2000, **147**, 517-523.
80. D. L. Wood, J. L. Li and C. Daniel, *J. Power Sources*, 2015, **275**, 234-242.
81. R. M. Gaume and L.-M. Joubert, *Rev. Sci. Instrum.*, 2011, **82**, 123705.
82. L. L. Lu, J. Ge, J. N. Yang, S. M. Chen, H. B. Yao, F. Zhou and S. H. Yu, *Nano Lett.*, 2016, **16**, 4431-4437.

83. C. J. Bae, C. K. Erdonmez, J. W. Halloran and Y. M. Chiang, *Adv. Mater.*, 2013, **25**, 1254-1258.
84. A. Pei, G. Zheng, F. Shi, Y. Li and Y. Cui, *Nano Lett.*, 2017, **17**, 1132-1139.
85. N. A. Liu, L. B. Hu, M. T. McDowell, A. Jackson and Y. Cui, *ACS nano*, 2011, **5**, 6487-6493.
86. D. Stevens and J. Dahn, *J. Electrochem. Soc.*, 2000, **147**, 1271-1273.
87. C. Bommier, T. W. Surta, M. Dolgos and X. Ji, *Nano Lett.*, 2015, **15**, 5888-5892.
88. T. Ohzuku, Y. Iwakoshi and K. Sawai, *J. Electrochem. Soc.*, 1993, **140**, 2490-2498.
89. N. N. Sinha, A. Smith, J. C. Burns, G. Jain, K. Eberman, E. Scott, J. Gardner and J. Dahn, *J. Electrochem. Soc.*, 2011, **158**, A1194-A1201.
90. A. P. Cohn, N. Muralidharan, R. Carter, K. Share and C. L. Pint, *Nano Lett.*, 2017, **17**, 1296-1301.
91. R. Zhang, X. R. Chen, X. Chen, X. B. Cheng, X. Q. Zhang, C. Yan and Q. Zhang, *Angew. Chem. Int. Ed.*, 2017, **56**, 7764.
92. C. Yang, Y. Yao, S. He, H. Xie, E. Hitz and L. Hu, *Adv. Mater.*, 2017, **29**, 1702714.
93. L. Medenbach, C. L. Bender, R. Haas, B. Mogwitz, C. Pompe, P. Adelhelm, D. Schröder and J. Janek, *Energy Technol.*, 2017, **5**, 2265.
94. V. Aravindan, Y. S. Lee and S. Madhavi, *Adv. Energy Mater.*, 2017, **7**, 1602607.
95. B. Zhang, R. Dugas, G. Rousse, P. Rozier, A. M. Abakumov and J.-M. Tarascon, *Nat. Commun.*, 2016, **7**, 10308.
96. E. Irisarri, A. Ponrouch and M. Palacin, *J. Electrochem. Soc.*, 2015, **162**, A2476-A2482.
97. R. Klee, M. J. Aragón, R. Alcántara, J. L. Tirado and P. Lavela, *Eur. J. Inorg. Chem.*, 2016, **2016**, 3212-3218.
98. Z. Du, K. Rollag, J. Li, S. An, M. Wood, Y. Sheng, P. Mukherjee, C. Daniel and D. Wood, *J. Power Sources*, 2017, **354**, 200-206.
99. A. Smith, H. M. Dahn, J. Burns and J. Dahn, *J. Electrochem. Soc.*, 2012, **159**, A705-A710.
100. J. Cannarella and C. B. Arnold, *J. Power Sources*, 2014, **245**, 745-751.
101. P. Meister, H. Jia, J. Li, R. Kloepsch, M. Winter and T. Placke, *Chem. Mater.*, 2016, **28**, 7203-7217.
102. D. Shanmukaraj, S. Grugeon, S. Laruelle, G. Douglade, J.-M. Tarascon and M. Armand, *Electrochem. Commun.*, 2010, **12**, 1344-1347.
103. Y. Sun, H. W. Lee, Z. W. Seh, G. Zheng, J. Sun, Y. Li and Y. Cui, *Adv. Energy Mater.*, 2016, **6**.
104. J. Zhao, J. Sun, A. Pei, G. Zhou, K. Yan, Y. Liu, D. Lin and Y. Cui, *Energy Storage Mater.*, 2018, **10**, 275-281.
105. M. Sathiya, J. Thomas, D. Batuk, V. Pimenta, R. Gopalan and J.-M. Tarascon, *Chem. Mater.*, 2017, **29**, 5948-5956.
106. J. M. De Ilarduya, L. Otaegui, J. M. L. del Amo, M. Armand and G. Singh, *J. Power Sources*, 2017, **337**, 197-203.
107. R. Dugas, B. Zhang, P. Rozier and J. Tarascon, *J. Electrochem. Soc.*, 2016, **163**, A867-A874.
108. X. Yao, Z. Zhu, Q. Li, X. Wang, X. Xu, J. Meng, W. Ren, X. Zhang, Y. Huang and L. Mai, *ACS Appl. Mater. Interfaces* 2018, **10**, 10022-10028.
109. A. Rudola, S. R. Gajjela and P. Balaya, *Electrochem. Commun.*, 2018, **86**, 157-160.
110. Z. Zhu, F. Cheng, Z. Hu, Z. Niu and J. Chen, *J. Power Sources*, 2015, **293**, 626-634.
111. P. Han, X. Han, J. Yao, L. Zhang, X. Cao, C. Huang and G. Cui, *J. Power Sources*, 2015, **297**, 457-463.
112. L. Seidl, N. Bucher, E. Chu, S. Hartung, S. Martens, O. Schneider and U. Stimming, *Energy Environ. Sci.*, 2017, **10**, 1631-1642.

113. M. Goktas, C. Bolli, E. J. Berg, P. Novák, K. Pollok, F. Langenhorst, M. v. Roeder, O. Lenchuk, D. Mollenhauer and P. Adelhelm, *Adv. Energy Mater.*, 2018, 1702724.
114. B. Jache, J. O. Binder, T. Abe and P. Adelhelm, *PCCP*, 2016, **18**, 14299-14316.
115. G. Yoon, H. Kim, I. Park and K. Kang, *Adv. Energy Mater.*, 2017, **7**, 1601519.
116. Z. J. Coppens, 2017.
117. A. Rudola, K. Du and P. Balaya, *J. Electrochem. Soc.*, 2017, **164**, A1098-A1109.